ROMA TRE
UNIVERSITÀ DEGLI STUDI

Scuola Dottorale di Ingegneria
Sezione di Ingegneria dell'Elettronica Biomedica,
dell'Elettromagnetismo e delle Telecomunicazioni

XXV CICLO DEL CORSO DI DOTTORATO

EXPERIMENTAL MICROWAVE PROPERTIES OF INNOVATIVE SUPERCONDUCTORS

Dottorando:
Kostiantyn Torokhtii

_____
(firma)

Docente Guida:
Prof. Enrico Silva

_____
(firma)

Coordinatore:
Prof. Lucio Vegni

_____
(firma)

Contents

List of Figures

List of Tables

Introduction

The investigation of the microwave characteristics of superconductors and superconducting structures are important for both applications (for the high field superconducting magnets, microwave filters, generators, transmission lines etc.) and the study of its fundamental properties. Microwave properties are an important source of information, especially when a magnetic field is applied to drive the material into the mixed state.

In the microwave frequency range, the relevant experimental quantity is the effective surface impedance $Z_s = R_s + iX_s$, where R_s and X_s are the surface resistance and reactance. At zero external magnetic field, R_s represents the losses of the microwave power, and is due to the presence of quasi-particles ("nonsuperconducting charge carriers"). X_s represents screening effects, and it can be used for the determination of the London penetration depth, related to the superconducting order parameter. In presence of a static magnetic field, type II superconductors are driven in the mixed state, where the magnetic field partially penetrates in the superconductor volume in shape of fluxons (vortices). In this case, R_s is mainly determined by the so-called flux flow resistivity, related to the quasi-particles excitations in the vortex cores, whereas X_s is related to the effect of the vortex pinning, which is important for the reduction of the vortex-motion-induced dissipation.

This thesis summarizes a three-year experimental study. The work is focused on the investigation of the high frequency electrical transport properties of complex superconducting systems.

The first part of my work consisted in the study of two classes of complex superconducting structures: ferromagnetic/superconductor/ferromagnetic trilayers and $YBa_2Cu_3O_{7-x}$ samples with nanosize $BaZrO_3$ columnar pinning centers. At the present time the study of the ferromagnetic/superconductor structures is an active field. The behaviour of ferromagnetic/superconducting multilayers is strongly affected by the magnetism of the ferromagnetic material. It induces Cooper pair breaking, and can favour the nucleation of fluxons, critical temperature oscillation versus ferromagnetic layer thickness, spontaneous persistent currents in rings interrupted by an superconductor/ ferromagnetic/

superconductor junction, superconducting order parameter oscillation in the ferromagnetic metal as opposed to the decay in normal metals. Here the effect of ferromagnetism on the superconductivity was studied by microwave characterization of $Nb/Pd_{0.81}Ni_{0.19}/Nb$ trilayers at zero field and in the mixed state.

High T_c superconductors (HTC) with artificially enhanced pinning centers were studied. In these materials the reduction of vortex motion, which is the main cause of power dissipation, is obtained by introducing artificial pinning centers. The anisotropy and pinning effects of $BaZrO_3$ inclusions on $YBa_2Cu_3O_{7-x}$ samples grown by pulsed laser deposition and chemical solution decomposition techniques were investigated.

There are various methods for the measurement of Z_s at microwave frequencies. The available methods include both resonant techniques (like cavity, dielectric loaded or microstrip line resonators) and non resonant methods (which are based on the transmission technique like the so-called Corbino disc).

In this work two methods were used, exploiting their complementary strengths: the dielectric resonator (DR) method, which works at a single frequency was chosen due to its high sensitivity and its small size (which is useful for the study of small samples) and the Corbino disk, which has a lower sensitivity, but it is capable to operate over a wide range of frequencies.

Another part of this work is devoted to the upgrade and development of measurement techniques. First, a 8.2-GHz dielectric resonator was designed, realized and put into operation. Second, a pre-existing 48-GHz dielectric resonator system was upgraded to the change the resonator operation from reflection to transmission. Third, a rectangular DR (for anisotropy study) was developed.

The outline of this thesis is is the following: in Chapter I a synopsis of the main theories of the superconducting state in magnetic field and vortex dynamics is presented; in Chapter II I describe the measuring technique and the measurement systems developed or upgraded during this thesis; in Chapter III the experimental results of the microwave response on the S/F/S trilayers at zero magnetic field and in the mixed state is discussed; in Chapter IV I discuss the experimental results on the HTS with columnar-like pinning centers in tilted magnetic field.

Chapter 1

Superconductivity

The phenomenon of the superconductivity was discovered by H. Kamerlingh Onnes in 1911 [1]. He observed the disappearance of the electrical resistivity of mercury by cooling down it below the so-called critical temperature T_c. Another fundamental phenomenon of superconductors is their ideal diamagnetism, which was first observed by W. Meissner and R. Ochsenfeld in 1933 [2]. The discover of superconductivity and the progress in the cooling technique gave a strong stimulus to the study of new superconducting materials. In the subsequent years many new superconducting materials were discovered, with growing critical temperatures. In 1971 Nb_3Ge with T_c=23 K had the highest critical temperature until the high temperature superconductivity was discovered in 1986. To describe the observed effects in new superconducting materials the theoretical description was needed. First phenomenological theory was created by brothers H. and F. London in 1935; later, V. L. Ginzburg and L. D. Landau proposed the theoretical description in 1950, and in 1957 Bardeen, Cooper and Schrieffer developed their microscopic theory of superconductivity. Notably, at present there is no universally accepted theory for superconductors.

The Meissner effect consists in the expulsion of the externally applied magnetic field by means of supercurrent (current flowing without dissipation) circulating in the surface layer. This effect indicates, that the transition from the normal to superconducting state is a thermodynamic phase transition. Below T_c the superconducting state is reached since its free energy is lower than the energy in the normal state. The difference between these energies is known as condensation energy. An applied magnetic field H increases the overall energy of the superconductor. At a specific value of H, the material dependent critical field H_c, the magnetic energy becomes larger than the condensation energy and the material finds its energy minimum by reverting to the normal state. The critical field above which the superconducting state disappears is
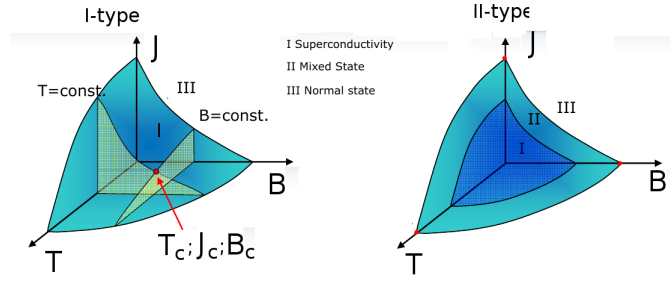
Figure 1.1: Phase diagrams of two types of superconductors

dependent from the temperature: at zero temperature its maximum reaches zero at T_c in conventional superconductors: $H_c(T) = H_c(0)(1 - (T/T_c)^2)$. In addition to T_c and H_c a third important parameter is the critical value of the current flowing through the superconductor J_c, above which the kinetic energy is higher than the condensation energy. This phenomenology characterizes the so-called I-type superconductors. The schematic phase diagram is shown in Fig. 1.1.

Another class is the type-II superconductivity, in which additional phenomena are observed. It is characterized by two states of superconducting phase (See Fig. 1.1). Correspondingly two critical fields are present. In magnetic field lower than H_{c1} the Meissner state is present. Increase of the field leads to the the transition in the so-called mixed state. In this case the external magnetic field partially penetrates in the volume of superconductor as "fluxons". The region of the H-T diagram between $H_{c1}(T)$ and $H_{c2}(T)$ is known as "vortex state" (see sec. 1.2). Above the upper critical field H_{c2} the superconductor reverts to the normal state.

In the following sections the main theories of the superconductivity at zero magnetic field and in the vortex state are briefly described.

1.1 Theoretical background

1.1.1 London theory

The phenomenological theory created by brothers H. and F. London describes the Meissner effect. This theory determines the dependence between electromagnetic field and current and takes into account only the superconducting current, which flows without resistance. It supposes, that electric and magnetic fields do not disturb the superconducting state. Based on the Drude law the current density of superconducting electrons is represented as $j_s = e n_s v_s$, where

n_s is the superconducting electrons density and v_s is the velocity of its motion. Combining this relation with the second Newton's law ($n_s m \frac{dv_s}{dt} = e n_s E$) one can obtain the first London equation:

$$\frac{dj_s}{dt} = \frac{n_s e^2}{m} E = \frac{1}{\Lambda} E \qquad (1.1.1)$$

where $\Lambda = m_s / e^2 n_s$ is the London parameter.

The second London's equation shows the relation between the magnetic field and superconducting current. It determines how the magnetic field penetrates in the superconductor in the Meissner state from the point of view of the free energy of the superconductor. Taking into account the value of the free energy of the superconductor at zero magnetic field (F_{s0}) and the relation for the current density: $curlH = j_s$ one can obtain the kinetic energy density of the supercurrent:

$$E_{kin} = \frac{n_s m v_s^2}{2} = \frac{m j_s^2}{2 n_s e^2} = \lambda_L (curlH)^2 \qquad (1.1.2)$$

There the magnetic field energy density is defined as $E_{mag} = \mu_0 H^2$.

Here the important quantity - the characteristic length on which the magnetic field penetrates in superconductor - is introduced as:
$\lambda_L = \sqrt{\Lambda / \mu_0} = (m/(\mu_0 n_s e^2))^{0.5}$.

The Gibbs free energy in the whole superconductor can be determined by the volume integral over the entire volume of the superconductor:

$$F_s = F_{s0} + \int (H^2 + \lambda^2 (curlH)^2) dV \qquad (1.1.3)$$

We can assume that superconductor electrons fit their motion to minimize electric and magnetic energies. Minimization of the free energy leads to the second London's equation:

$$H + \lambda_L^2 curl curl H = 0 \qquad (1.1.4)$$

This law describes the Meissner effect - in stationary case there is no magnetic field inside the superconductor.

Now it is possible to determine how the magnetic field H_0 penetrates in the volume of the superconductor. Let's suppose the superconductor/vacuum boundary positioned at x=0 with superconductive sample semispace $x > 0$. The magnetic field is applied parallel to the surface of superconductor. The solution of eq. 1.1.4 with boundary condition for the Meissner state (H(0)=H_0 and H(∞)=0) give the exponential law of the magnetic field decay: $H = H_0 \exp(-x/\lambda_L)$ for $x > 0$.

This means that screening supercurrent falls off over the length λ_L and can be rewritten as:

$$j_s = -\frac{H_0}{\mu_0 \lambda_L} e^{x/\lambda_L} \qquad (1.1.5)$$

There are few limitations of the London theory: it is valid only in the local limit; there is no normal component considered. Local limit takes into account that a vector potential (defined as $\overrightarrow{H}=\mathrm{curl}\overrightarrow{A}$) changes with distance slower than size of superconducting carriers. It is not able to describe the whole range of the experimentally observed effects.

The modified London's theory for non-local case was proposed by Pippard [3], introducing the coherent length term ξ_0 - phase coherent length of the superconducting carriers: $\xi_0 = a\frac{hv_F}{kT_c}$ where $a \sim l$

Pippard has seen the similarity of the London equation and the Ohm law which, in non-local representation, is:

$$\overrightarrow{j}_s = -\frac{1}{\lambda_P^2}\overrightarrow{A} \qquad (1.1.6)$$

Here $\lambda_P \approx (\lambda_L^2 \xi_0)^{1/3}$ is the so-called Pippard penetration depth. It shows that, in case $\lambda_L \ll \xi_0$, $\lambda_P \gg \lambda_L$, i.e. nonlocal electrodynamics predicts deeper penetration of the magnetic field with respect to local limit.

The analysis of high frequency experimental data shows that ξ is decreased with the impurities concentration. Introduction of the impurity decreases the free length distance of the electron interaction and ξ decreases too. Pippard proposed an empirical relation for the coherent length: $1/\xi = 1/\xi_0 + 1/\alpha l$, where $\alpha \approx l$ [3].

With introduced coherence length term the classification of the superconductor materials can be made:pure superconductors are characterized by the mean free path $l \gg \xi_0$ and can be described by the non-local theory; metals with large number of impurities and alloys have $l \ll \xi_0$

1.1.2 Two-fluid model

Gorter and Kazimir in their theory take that the superconductor material are containing two kinds of the charge [4]: superconductive and normal component. The total charge density is $n = n_s + n_n$ where n_n and n_s are the normal and superconductive charge densities, respectively.

The total current in the superconductor can be represented as $j = j_s + j_n = (\sigma_1 - i\sigma_2)E$, where superconducting and normal components of the current density are described as $j_{s,n} = n_{s,n}ev_{s,n}$. Here the complex conductivity term

$\sigma_{eff} = (\sigma_1 - i\sigma_2)$ is introduced [4, 5] and was assumed that the normal skin effect approximation is valid so that the mean free path of the electrons is much lower than the penetration depth and the frequency of the electromagnetic field is so small that it can not destroy the superconducting state. One can describe the electrodynamic of the superconductors based on the London's equations and Drude law within the two-fluid model:

$$m\frac{dv_s}{dt} = -eE \qquad m\frac{dv_n}{dt} + m\frac{v_n}{\tau} = -eE \qquad (1.1.7)$$

where v_n and v_s are the velocities of the normal and superconducting components; τ is the relaxation time of the normal component.

In case of harmonic wave the electric field and current density are proportional to $e^{i\omega t}$. In this case one can extract the current densities of the superconducting and normal fluids:

$$j_s = -i\frac{1}{\Lambda\omega}E \qquad j_n = -\frac{n_n}{n_s}\frac{\tau}{\Lambda}\frac{1 - i\omega\tau}{1 + (\omega\tau)^2}E \qquad (1.1.8)$$

The corresponding complex conductivity is represented as:

$$\sigma_1 = \frac{n_n e^2 \tau}{m(1 + \omega^2\tau^2)} \qquad \sigma_2 = \frac{n_s e^2}{m\omega} + \frac{n_n e^2 \omega^2 \tau^2}{m\omega(1 + \omega^2\tau^2)} \qquad (1.1.9)$$

In the microwave frequency range (up to 100 GHz) for the case T<T$_c$ and $\omega\tau \ll 1$ the complex conductivity can be represented as $\sigma_{eff} = \sigma_n n_n/n + i(1/\omega\mu_0\lambda_L^2)$ [6]. In this case the imaginary part of the σ_{eff} is directly connected to the penetration depth and superconducting electrons density. At high frequencies $\omega\tau \gg 1$, the superconductor conductivity becomes completely inductive.

Within the two-fluid model a temperature dependence of the penetration depth can be obtained. Within this model the empirical temperature dependence for the density of the electrons ($n_s/n = 1 - (T/T_c)^4$) is obtained. Using the London penetration depth definition, its temperature dependence can be obtained:

$$\lambda_L/\lambda_L(0) = (1 - (T/T_c)^4)^{-0.5} \qquad (1.1.10)$$

1.1.3 BCS theory

A microscopic theory of superconducting state was proposed by Bardeen Cooper and Schrieffer (BCS) [7]. It explains well the experimentally observed phenomenons in traditional superconductors and can be applied to some kinds of high temperature superconductors. The basic concept of BCS theory is that

electrons are bounded in so-called Cooper pairs [8] and the energy gap (Δ) appeared in the energy spectrum of the superconductor. In traditional superconductors attractive interaction was found within electron - phonon coupling through the local polarization of the crystal lattice in vicinity of electron. This induces the local positive charge capable to attract the second electron.

Cooper problem [8] sets the pairing energy as 2Δ where Δ is the lowest single-particle excitation energy. BCS states the size of the pair as $\xi \sim \hbar v_F/\Delta$ (or coherent length). At T=0 K in this case all electrons in the superconductor are coupled in pairs and energy 2Δ is needed to destroy a Cooper pair. At temperature different from zero the thermal depairing occurs and the quasiparticles state occupation is described by the Fermi function $f(E_k) = (\exp(E_k/k_BT)+1)^{-1}$, where $E_k = \sqrt{\epsilon_k^2 + \Delta^2}$ is the energy of the excited level; ϵ_k^2 is kinetic energy of the electron with wave vector k.

In BCS theory the coherent effects in superconductor are connected to the density of the states (DOS) of quasiparticles in superconductor. The density of states in quasiparticles $N(E)$ is represented as:

$$N(E) = N_F \left\{ \begin{array}{ll} \frac{E}{\sqrt{E^2-\Delta^2}} & for E > \Delta \\ 0 & for E > \Delta \end{array} \right. \tag{1.1.11}$$

where N_F is the density of states near the Fermi level in normal conductor.

In BCS theory the temperature dependence of the energy gap can be determined based on the gap relation for Δ_k:

$$\Delta_k = -1/2 \sum_{k'} V_{kk'} \frac{\tanh\left(E_{k'}/2k_BT\right)}{E_{k'}} \Delta_{k'} \tag{1.1.12}$$

where $V_{kk'}$ is the matrix element of the interaction potential of the Cooper pairs with potentials $\hbar k$ and $\hbar k'$, which is considered as isotropic and constant near the Fermi surface and absent outside it.

For isotropic case of s-wave superconductor the temperature dependence of the energy gap can be obtained in implicit form as:

$$\frac{1}{N(0)V} = \int_0^{\hbar\omega_c} \frac{\tanh\left(\sqrt{\epsilon_k^2 + \Delta^2}/2k_BT\right)}{\sqrt{\epsilon_k^2 + \Delta^2}} d\epsilon \tag{1.1.13}$$

where V is the interaction potential, which is considered as isotropic and constant near the Fermi surface and absent outside it.

This relation determines the energy gap at zero temperature as $\Delta(0) = 2\hbar\omega_D \exp(-1/N(0)V)$ and the well known universal relation $\Delta(0) \approx 1.764 k_B T_c$. The temperature dependence of the energy gap can be determined from eq. 1.1.13.

As an example, in the temperature interval $T < 0.4T_c$ the exponential law of the temperature dependence of the gap can be demonstrated [9]:

$$\Delta(T) \approx \Delta(0) - \sqrt{2\pi\Delta(0)k_B T}\exp(-\Delta(0)/k_B T) \qquad (1.1.14)$$

To describe the term of the conductivity within BCS model one can use the two-fluid model representation and take into account both normal σ_n and superfluid σ_s components. For clean local limit ($\xi \ll l \ll \lambda_L$) at low frequencies ($\omega\tau \ll 1$) one can obtain the relation for the superfluid component of the conductivity:

$$\sigma_s = \frac{ne^2}{m}\frac{1}{i\omega}\left[1 - \int_{-\infty}^{\infty}-\frac{\partial f(E)}{\partial E}dE\right] \qquad (1.1.15)$$

and for the normal component of the conductivity

$$\sigma_n = \frac{ne^2}{m}\int_{-\infty}^{\infty}-\frac{\partial f(E)}{\partial E}\frac{1}{1/\tau_s(E)+i\omega}dE \qquad (1.1.16)$$

where τ_s is the energy dependent quasiparticles relaxation time

These relations give the temperature dependence of the penetration depth and also the imaginary part of the conductivity. In the dirty London limit ($l \ll \xi_0$ and $\lambda \gg \xi$) one can calculate [10]:

$$\sigma_2(T)/\sigma_2(T_c) = \lambda_L^2(0)/\lambda_L^2(T) = \frac{\Delta(T)}{\Delta(0)}\tanh\left(\frac{\Delta(T)}{2k_B T}\right) \qquad (1.1.17)$$

For the real part of conductivity:

$$\sigma_1(T)/\sigma_1(T) = \Delta(T)/2k_B T\coth(\Delta(T)/2k_B T)\ln(\Delta(T)/\hbar\omega) \qquad (1.1.18)$$

In this limit the so-called coherence peak appears on the temperature dependence of the real conductivity, which is associated with logarithmic divergence. In the BCS theory, coherence effects arise whenever interference effects among quasiparticles excitations are relevant, thus preventing their modelling as uncorrelated charge carriers implicit in two-fluid model.

1.1.4 Ginzburg-Landau theory

The theory proposed by Ginzburg and Landau in 1950 is the extension of the London phenomenological theory for the case of spatially varying superfluid density. It is based on the Landau theory of the second order phase transition. Theory of Ginzburg-Landau (G-L) is based on the assumption that the thermodynamic characteristics of the superconductor are described by an

order parameter $\psi(r)$. The order parameter is nonzero at any temperature lower than the temperature of the phase transition and equal to zero above it, so it is associated to the electronic condensation of superconducting carriers. In this formulation $|\psi(r)|$ represents the local superconducting charge carriers density.

Within the G-L theory the volume density of Helmholtz free energy can be expanded in a series of powers of $|\psi(r)|^2$:

$$f(r) = f_n + \alpha|\psi(r)|^2 + \frac{\beta}{2}|\psi(r)|^4 + \frac{1}{2m}\left|\left(\frac{h}{i}\nabla - \frac{e}{c}A(r)\right)\psi(r)\right|^2 \quad (1.1.19)$$

where $\alpha = -\mu_0 H_c^2/|\psi|^2$ and $\beta = \mu_0 H_c^2/|\psi|^4$ are coefficients with a smooth and regular temperature dependence; f_n is the free energy of the normal state.

To obtain more general equations, including the interaction with vector potential, the volume density of Gibbs energy can be used: $g = f - b(r)H$. Here $b(r)$ is the local value of the magnetic flux density; small case letters describe local values of the parameters. G-L equation in the view of the Gibbs energy contains two unknown quantities: $\psi(r)$ and vector potential $\overrightarrow{A}$

Minimization of the volume density of Gibbs energy with respect to these parameters leads to the differential G-L equation, which in equilibrium state, connects supercurrent and vector potential [11]:

$$\hat{J}_s = \nabla^2 A/\mu_0 = (\mathrm{i}eh/2m)(\psi^*\nabla\psi - \psi\nabla\psi^*) + (4e^2/m)|\psi|^2\hat{A} \quad (1.1.20)$$

This relation for a bulk superconductor, in low field case and for small variation of the order parameter, reduces to the London relation $\hat{J}_s = -n_s e^2/m\hat{A}$ with constant order parameter $|\psi_\infty|^2 = -\alpha/\beta$. This shows, that $|\psi|^2$ corresponds to the superconducting pair density n_s^*.

Minimization of eq. 1.1.20 with respect to ψ leads to the second G-L differential equation:

$$\alpha\psi(r) + \beta|\psi(r)|^2\psi(r) + \frac{1}{2m}\left(h\mathrm{i}\nabla - 2eA(r)\right)^2\psi(r) = 0 \quad (1.1.21)$$

One can write the equation for the G-L penetration depth in analogy to the London one:

$$\lambda_{GL} = \sqrt{\frac{m}{\mu_0 e^2 |\psi_\infty|^2}} \quad (1.1.22)$$

Another quantity can be introduced in G-L theory. The so-called Ginzburg-Landau coherence length is:

$$\xi_{GL} = \sqrt{\frac{h^2}{2m|\alpha|}} \qquad (1.1.23)$$

ξ_{GL} denotes the length, over which the order parameter can vary significantly. It is related to the low-temperature BCS value ξ_0. The ratio of two characteristic lengths is called G-L parameter: $\kappa = \lambda_{GL}/\xi_{GL}$, which is independent from temperature.

According to the value of the G-L parameter the superconductors are divided in two classes: type I with $\kappa < 1/\sqrt{2}$ (in which the superconductor is characterized only by the Meissner state) and type II with $\kappa > 1/\sqrt{2}$ (where the mixed state appears).

To evaluate the dynamic features introduced in G-L theory, the time dependent G-L theory can be used to include relaxation processes for nonequilibrium superconductivity. According to this the G-L equation can be rewritten as:

$$\frac{2|\alpha|}{\hbar}\tau_{rel}\left(\hbar\frac{\partial}{\partial t} - 2ie\Phi_{e1}\right) = -\frac{1}{2m}(-i\hbar\nabla - 2eA)\psi - \alpha\psi - \beta|\psi|^2\psi \qquad (1.1.24)$$

where Φ_{e1} is the electrostatic potential; $\psi = \psi(r,t)$. The component, which takes into account the relaxation process is $\tau_{rel} = h/(32k_B(T_c-T))$, it describes the exponential decay of ψ and deviation from the equilibrium value $\sqrt{|\alpha|/\beta}$.

1.2 Vortex state of superconductors

The type-II superconductors are characterized by the mixed state, which appears when the external magnetic field $H_{c1} < H < H_{c2}$ is applied. In this case the magnetic field penetrates in the superconductor volume as fluxons. The fluxon can be represented as a tube, which has the normal phase in the center and is surrounded by closed superconducting currents. First theoretical description of this effect was given by Abrikosov [9].

Within the G-L framework the vortex lattice geometry can be determined for type II superconductors. The order parameter phase turns by 2π around the vortex and drives the rotating current. Near the center of the vortex the order parameter is suppressed, $\psi(0) = 0$ along the axis of the vortex. Rotating screening currents generate a magnetic field and bind a flux to the vortex extending a distance λ away from the vortex axis.

It is shown that each fluxon carries only one flux quantum $\Phi_0 = h/2e$ and that the system of the fluxons allows to reduce the free energy with respect to

the fully diamagnetic Meissner state. Spatial distribution of the magnetic field follows from the London equation $[1 - \lambda^2 \bigtriangledown^2]B = 0$ completed with the G-L theory by the source term $\Phi_0 \hat{z} \delta^2(r)$. Integration of the second G-L differential equation the magnetic field profile can be obtained for r> ξ [12]

$$B(r) = \frac{\Phi_0 \hat{z}}{2\pi\lambda^2} K_0(r/\lambda) \tag{1.2.1}$$

where $K_0(r/\lambda \ll 1) \sim \ln \rho$ and $K_0(r/\lambda \ll 1) \sim e^{-r/\lambda}/\sqrt{r/\lambda}$ are the MacDonald functions.

The energy of a vortex can be determined considering the kinetic contribution of the screening currents, the field energy and the condensation energy of the normal core. The numerical solution of the G-L equation with $\kappa \gg 1$ provides the vortex energy in the form [10]

$$\epsilon_l = \varepsilon_0 \left[\ln(\lambda/\xi) + C_c\right] \tag{1.2.2}$$

where $\varepsilon_0 = \left(\frac{\Phi_0}{4\pi\lambda}\right)^2$ is the basic energy scale; C_c, includes the contribution from the normal core ($\ll \ln(\kappa)$) and magnetic energy. Different values, presented in literature [10, 13], show that $C_c \sim 0.1 - 0.5$. In HTS, the current and magnetic field can induce additional components, but their impact in the vortex energy is small.

For anisotropic superconductors, such as HTS, the free energy per unit length (ϵ_l) of a vortex depends on the angle ϑ between the vortex axis and crystal ab-plane of the material [14] (see Fig. 1.2). Here the ab-plane corresponds to the plane surface (boundary between vacuum and superconductor) and c-axis is perpendicular to it.

$$\epsilon_l = \varepsilon_0 \varepsilon_\vartheta \ln(\lambda/(\xi\varepsilon_\vartheta)) \tag{1.2.3}$$

where $\varepsilon_\vartheta^2 = \varepsilon^2 \cos^2 \vartheta + \sin^2 \vartheta$ is the anisotropy parameter; $\varepsilon^2 = m/M$ is the mass anisotropy parameter with $m = m_{ab}$ and $M = m_c$.

The vortex energy allows to determine the lower critical field. For isotropic superconductors H_{c1} is determined by the energy gain ($[H_{c1}\Phi_0]/[4\pi]$) when the single vortex enters in superconductor driving it in the mixed state as follows [13]:

$$H_{c1} = \frac{4\pi\epsilon_l}{\Phi_0} = \frac{\Phi_0}{4\pi\lambda^2} \left[\ln(\lambda/\xi) + C_c\right] \tag{1.2.4}$$

In large fields $H \rightarrow H_{c2}$ the overlap of the vortices drives the whole superconductor in the normal state, where its surface can be represented as covered
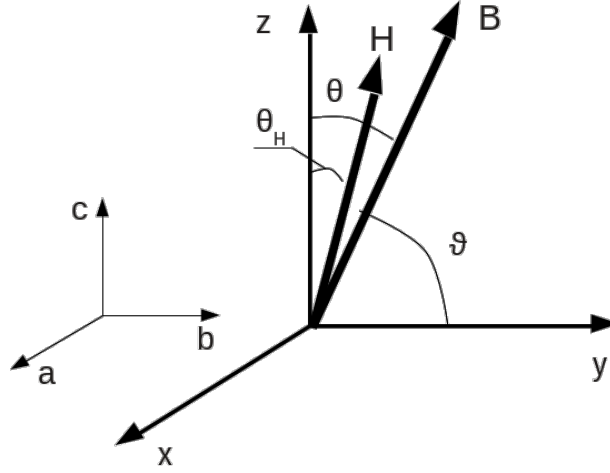
Figure 1.2: Reference coordinate system used in the description of the parameters in anisotropic superconductors. The crystal axis of the superconductor (a,b and c) are aligned along with the x, y and z axis correspondingly

by the normal cores. The upper critical field is [15]:

$$H_{c2} = \frac{\Phi_0}{2\pi\xi^2} \tag{1.2.5}$$

For the anisotropic superconductors more complex estimations are needed. Critical fields are calculated by minimization of Gibbs energy. In [14] they are determined as:

$$H_{c1}(\theta_H) = \frac{\Phi_0}{4\pi\lambda^2} \frac{\varepsilon}{\varepsilon_{\theta_H}} \ln(\lambda/(\xi\varepsilon_\vartheta)) \tag{1.2.6}$$

and

$$H_{c2}(\theta_H) = \frac{\Phi_0}{2\pi\varepsilon_{\theta_H}\xi^2} \tag{1.2.7}$$

where θ_H is the angle between the magnetic field and axis of anisotropy c (see Fig. 1.2); $\varepsilon_{\theta_H} = \varepsilon^2(1 + \varepsilon^2\cot^2\theta_H)/(1 + \varepsilon^2\cot^2\theta_H)$; $\vartheta_H = \pi/2 - \theta_H$. In this case the anisotropic core has a dimension ξ and $\varepsilon_{\theta_H}\xi$ along the a and b directions correspondingly. For $H \gg \sqrt{\frac{\Phi_0}{2\pi\xi^2}}/\varepsilon_\theta$ vortices align to the magnetic field direction.

1.2.1   Vortex motion models

The applied current affects the vortices with the Lorentz force, which drives the vortex movement in direction perpendicular to the direction of applied

current [10]:

$$\overrightarrow{f}_L = \overrightarrow{J} \times \hat{n}\Phi_0 \qquad (1.2.8)$$

where Φ_0 is the flux quantum; $\hat{n}$ is the unit vector yielding the magnetic field direction.

The vortex movement with a velocity v_L generates the electric field $\overrightarrow{E} = \overrightarrow{v}_L \times \overrightarrow{B}$

In the case of the single vortex and where only free vortex flow is present, vortex (and magnetic) motion occurs in direction perpendicular to the direction of applied current with a velocity v_L. This movement, in turn, generates the electric field $\overrightarrow{E} = \overrightarrow{v}_L \times \overrightarrow{B}$. In the free fux-flow regime the Lorentz force is counteracted only by the friction force of the medium ($\overrightarrow{F} = -\eta\overrightarrow{v}_L$). Here the coefficient η is a viscous drag coefficient, related to the relaxation processes of the quasiparticles [14, 16].

In a real superconductor the defects of the crystal structure are always present. They represent the preferable sites for vortices (pinning centers), since they allow to minimize the total condensation energy cost. The presence of the pinning is the cause of the additional force (the pinning force $\overrightarrow{F}_p$) which reduces the mobility of the vortex. In presence of the d.c. current, a vortex starts to move only for $J > J_c$, where J_c is the current yielding $F_L > F_{p,max}$.

The balance of the fields acting on the vortex can be obtained in the following form:

$$\overrightarrow{F} + \overrightarrow{F}_H + \overrightarrow{F}_p = \overrightarrow{F}_L + \overrightarrow{F}_t \qquad (1.2.9)$$

where $\overrightarrow{F}_t$ represents the force of the thermally activated vortex movement; $\overrightarrow{F}_H = \alpha_H\hat{n} \times \overrightarrow{v}_L$ is the perpendicular force on a moving vortex (Hall force), which subtends the Hall angle $\Theta = \arctan(\alpha_H/\eta)$. Usually $\alpha_H \ll \eta$ and Hall angle is small and taking that, it can be neglected [14]. It becomes relevant only in the clean limit.

Now I shortly discuss the parameters in the force balance relation.

Pinning force.
The pinning force contribution is related to the spatial variation of the pinning potential as: $\overrightarrow{F}_p = -\bigtriangledown U$.

When a small displacement of the vortices occurs, the vortex does not interact with nearby ones (single vortex approximation). Considering the harmonic regime $J \propto e^{i\omega t}$ and sufficiently high angular frequency ω the vortex oscillates with small amplitude around the equilibrium position. In the limit of small displacement ($u = v_L/(i\omega)$) the pinning force is elastic and can be rewritten

as: $\overrightarrow{F}_p = -\triangledown U \simeq -k_p u$, where $k_p = \nabla^2 U$ is the pinning constant (also known as Labusch parameter, α_L)

Vortex viscosity.

Neglecting pinning effects, the Lorentz force is compensated only by drag force. Motion of the vortices generates the electric field, which can be divided by two components: longitudinal to the current, which produces the dissipation, and transversal, which determines the Hall effect. Two mechanisms of the dissipation due to vortex motion are considered. The first is related to the condensation energy during movement: the Cooper pairs on the vortex front side are transformed to quasi-particles with loss of the energy, the inverse transformation occurs on the rear side, but only part of the energy is recovered due to the finite relaxation time [9].

In the free flux-flow regime, the flux-flow resistivity can be rewritten in the form, given by Bardeen and Stephen [17]:

$$\rho_{ff} = \frac{\mu_0 H_{c2} \Phi_0}{\eta} \tag{1.2.10}$$

The second mechanism is due to the Joule dissipation by the normal currents moving through the vortex core [18]. The power dissipated per unit length is related to η through $W = Fv_L = \eta v_L^2$. In [14, 19] the vortex viscosity is determined in the general case:

$$\eta = \pi h n \frac{\omega_0 \tau}{1 + (\omega_0 \tau)^2} \tag{1.2.11}$$

where $\omega_0 = e\mu_0 H_{c2}/m$ is the cyclotron frequency given by the level separation of the quasi-particle states within the vortex core [20].

Two regimes can be identified: superclean $\omega_0 \gg \tau$ and moderately clean $\omega_0 \ll \tau$. In the moderately clean limit in absence of the Hall effect the Bardeen and Stephen (BS) relation [18] can be obtained as:

$$\eta = \pi h n \omega_c \tau = \frac{\mu_0 H_{c2} \Phi_0}{\rho_n} \tag{1.2.12}$$

where $\rho_n = m^*/ne\tau$ is the normal state conductivity.

At $\omega_0 \gg \tau$ the Hall contribution dominates and viscosity can be determined as: $\eta \approx \pi h n / \omega_c \tau$ [19].

Thermally activated depinning.

Various types of the defects in the superconductors like defects, impurities, stresses etc. pin the vortices. Pinning in the superconductor can be represented as non-periodic pinning potential. For the vortices it is energetically effective
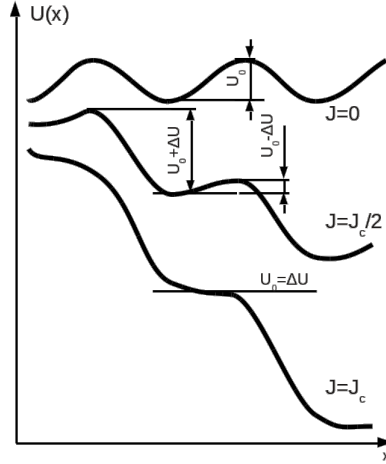
Figure 1.3: The representation of the pinning potential well along the coordinate of the Lorentz force

to be in the bottom of the pinning well. Overcoming the energy well leads to the flux motion. The energy barrier can be written as $U_0 = 0.5\mu_0 H_c^2 l^3$, where H_c is the thermodynamic critical field and l is the linear dimension of the point-like defects.

With increasing magnetic field the potential well height decreases. In this case the possibility of the thermally activated vortex motion increases.

The rate of the vortex jump is determined as $\varpi = \omega_t e^{-U_0/k_B T}$ [21], where ω_t is the characteristic frequency in the range $10^5 - 10^{11}$ sec^{-1}.

A d.c. external current produces the tilt of the pinning potential as shown in Fig. 1.3. Along the Lorentz force direction the energy well height is lowered by Lorentz force energy with respect to the unperturbed pinning potential and equal to $U_0 - \Delta U$. Here the shift of the barrier height is equal to the work done by the driving force and is determined as $\Delta U \propto J$. The resulting net jump rate in the current direction is [21, 10]

$$\varpi = \omega_t e^{-U_0/k_B T} = \omega_t e^{-U_0/k_B T} \left(\omega_t e^{\Delta U/k_B T} - \omega_t e^{-\Delta U/k_B T} \right) \qquad (1.2.13)$$

Here, the barrier energy is $U_0 = 0.5\mu_0 H_c^2 l^3$. The pinning is more effective when the correlation length $l \simeq \xi$ (strong pinning). In this case the pinning force can be determined as $F_p \sim \mu_0 H_c^2 \xi$. The condition $l < \xi$ gives lower pinning force due to smaller energy gain of smaller defect, at $l > \xi$ gives the residual movement freedom to the fluxon and $F_p \sim 1/l$.

Currents near J_c (depinning current density) lead to the pinning potential $U_L \to 0$ and to the flux-flow regime.

Now I introduce the models of the ac vortex motion. Basically they take into account the relation 1.2.9.

Gittleman and Rosemblum (GR) model.

As an example, I show the deduction of the simple model relation. This model is valid for the superconductor at the temperatures $T \ll T_c$ where the effect of the thermally activated movement is negligible [22]. Neglecting the Hall and thermal forces leads to the relation:

$$\eta \overrightarrow{v}_L + \frac{k_p \overrightarrow{v}_L}{\mathrm{i}\omega} = \overrightarrow{J} \times \hat{n} \Phi_0 \qquad (1.2.14)$$

For current $\overrightarrow{J} \perp \overrightarrow{B}$ in the scalar form one obtains:

$$\left[\eta + \frac{k_p}{\mathrm{i}\omega} \right] v_L = JB\Phi_0 \qquad (1.2.15)$$

from this, using the relations $\overrightarrow{E} = \rho_{vm} \overrightarrow{J}$ and $\overrightarrow{E} = \overrightarrow{B} \times \overrightarrow{v}_L$, the vortex motion resistivity can be obtained as:

$$\rho_{vm} = \frac{B\Phi_0}{\eta} \frac{1}{1 - \mathrm{i}\frac{k_p}{\eta\omega}} \qquad (1.2.16)$$

Two important parameters are included in ρ_{vm}: the flux-flow resistivity $\rho_{ff} = \frac{B\Phi_0}{\eta}$ and the so-called depinning angular frequency $\omega_p = \frac{k_p}{\eta}$, which marks the crossover between elastic and dissipative motion. At lower frequencies ($\omega \ll \omega_p$) ρ_{ff} is imaginary. At high frequencies it is fully ($\omega \gg \omega_p$) dissipative end equal to the flux-flow resistivity $\rho_{vm} = \rho_{ff} = \frac{B\Phi_0}{\eta}$, where movement of the vortices is not affected by pinning. In this regime it is possible to determine directly the the flux-flow resistivity without application of large current densities.

Coffey-Clem (CC) model

Thermal force is considered in the Coffey and Clem model. Here the pinning potential has a sinusoidal form [23, 24], so that the pinning potential is uniform and periodic with the potential well height U_0. Under these conditions the vortex motion resistivity is:

$$\rho_{vm} = \frac{B\Phi_0}{\eta} \frac{\epsilon + \mathrm{i}\frac{\omega_p}{\omega_0}}{1 + \mathrm{i}\frac{\omega_p}{\omega_0}} \qquad (1.2.17)$$

where $\epsilon = (I_0(u/2))^{-2}$ is a creep factor and $\omega_0 = \omega_p \frac{1}{1-\epsilon} \frac{I_1(u/2)}{I_0(u/2)}$. Here I_1 and I_0 are the modified first and zero order Bessel functions; $u = \frac{U_0(T,B)}{K_B T}$ is the

normalized energy barrier height (K_B is the Boltzmann constant).

The creep factor is a parameter which varies between 0 and 1. In absence of the creep ($\epsilon \to 0$) equation 1.2.17 reverts to the more simple GR model (eq. 1.2.16). Thermal effects are not negligible for the temperature near T_c: in this case the creep factor $\epsilon \to 1$, the pinning well height is small and the pinning effect disappears completely. Vortex motion becomes a fully dissipative flux-flow regime, independently from the frequency.

Brandt (B) model.

The model of the vortex motion, proposed by H. Brandt, considers that thermal depinning leads to the relaxation of the pinning constant: $k_p(t) = k_p e^{-t/\tau_r}$, where $\tau_r = \tau_p e^{U_0/K_B T}$ is the relaxation time [25, 26]. The corresponding vortex resistivity is:

$$\rho_{vm} = \frac{\Phi_0 B}{\eta} \frac{\epsilon' + i\omega\bar{\tau}}{1 + i\omega\bar{\tau}} \tag{1.2.18}$$

where $\epsilon' = \frac{\tau_p}{\tau_p + \tau_r}$ takes the role of a creep parameter, $\bar{\tau} = \frac{\tau_p \tau_r}{\tau_p + \tau_r}$ is the characteristic time for thermal activated depinning, where $\tau_p = 1/\omega_p$ is the inverse of the depinning angular frequency and U_0 is the pinning potential barrier height [27]. The creep parameter can be written as $\epsilon' = \frac{1}{1 + e^{U_0/K_B T}}$.

This model introduces the parameter $\bar{\tau}$ which is the equivalent of ω_0 in CC model, so that $\omega_0 = 1/\bar{\tau} = \tau_p^{-1} + \tau_r^{-1}$. It is worth noting that, within this model a tighter algebraical condition $0 \le \epsilon' \le 1/2$ holds, therefore this states the conditions of the model applicability and has to be taken into account in the experimental data elaboration process. This model does not require any specific assumption about the pinning potential landscape, thus allowing in principle to include also other mechanisms like quantum flux creep [25, 26]. Application of this model is bounded by the creep rate $\epsilon' \to 0.5$ at $\omega \gg \tau_p^{-1}$, where purely flux-flow regime can not be reached for any finite or zero frequency. At $U_0 \to \infty$ creep is negligible and this model gives the GR relation.

Universal expression.

The previously discussed models can be turned into the following universal expression [27]:

$$\rho_{vm} = \frac{\Phi_0 B}{\eta_{eff}} \frac{\epsilon_{eff} + i\omega\tau_{eff}}{1 + i\omega\tau_{eff}} \tag{1.2.19}$$

where τ_{eff} is the main time constant governing the vortex oscillations (usually linked to the pinning characteristic frequency), and the dimensionless parameter ϵ_{eff} is a measure of the weight of creep phenomena. It is bound to the

interval $0 < \epsilon_{eff} < 1$ in order to recover the correct zero frequency limit, which must be $0 \le \rho_{vm} \le \rho_{ff}$. It can be noted that, according to eq. (1.2.19), $\rho_{vm,2} \ge 0$ always.

1.2.2 Determination of vortex parameters

The described models of the vortex motion allow to determine the main vortex parameters like η, k_p, ρ_{ff} starting from the measured complex resistivity $\rho_{vm} = \rho_{vm,1} + \mathrm{i}\rho_{vm,2}$. One way is the fit of the frequency dependence of the ρ_{vm}. This method is reliable only for wideband measurements.

In this section I describe the procedure of the parameter determination from a single frequency measurements (as those obtains using resonant techniques). They can be interpreted based on the experimental parameter $r = \frac{\rho_{vm,2}}{\rho_{vm,1}}$. This is a dimensionless parameter, which gives a measure of the relative weight of the reactive to resistive response [28, 29], given essentially by the elastic and dissipative response of the vortex. At $r \ll 1$ flux low regime dominates in vortex dynamics, at $r \gg 1$ the pinning dominates. The fact that parameter r is model independent and unaffected by the systematic errors in the experiment makes it a good instrument in the interpretation of the experimental data and its comparison with theory (see section 1.2.1).

Within the GR model, where creep is negligible this parameter is:

$$r = \frac{\omega_p}{\omega} = \frac{\rho_{ff}}{\rho_C} \tag{1.2.20}$$

where $\rho_C = \frac{\Phi_0 B}{k_p \omega}$ is the Campbell resistivity [30].

Based on the r parameter the flux flow resistivity and pinning coefficient can be written as:

$$\rho_{ff} = \rho_{vm,1} \left[1 + r^2 \right] \tag{1.2.21}$$

$$k_p = r\omega B \Phi_0 / \rho_{ff} = \omega B \Phi_0 \frac{\rho_{vm,2}}{\rho_{vm,1}^2 + \rho_{vm,2}^2} \tag{1.2.22}$$

Calculation of this parameters in general case is a more complex procedure. The detailed procedure, which is based on the universal expression is described in [27]. The universal expression allows to separate the parameters in a independent way. In terms of the universal expression for the ρ_{vm}, the parameter r is:

$$r = \frac{\rho_{vm,2}}{\rho_{vm,1}} = \varpi \frac{1 - \epsilon_{eff}}{1 + \varpi^2 \epsilon_{eff}} \tag{1.2.23}$$

where $\varpi = 1/(\omega\tau_{eff}) \ge 0$. The ratio r belongs to the interval $[0, \infty]$.

Creep factor.

From the relation above the maximum possible creep factor can be obtained [27]:

$$\epsilon_{eff} \leq \epsilon_{eff,max}(r) = 1 + 2r^2 - 2r\sqrt{1+r^2} \tag{1.2.24}$$

This relation gives the upper bound for the creep factor. Creep factor ϵ can't be obtained directly from the single frequency experimental data: only its maximum value can be obtained. The function $\epsilon_{eff,max}(r)$ decreases monotonously from 1 to 0 when r spans the interval $[0, \infty]$.

The two parameters: ϵ_{eff} and r allow to calculate the other. As an example, parameter ϖ:

$$\varpi = \frac{1 - \epsilon_{eff} - \sqrt{A}}{2r\epsilon_{eff}} \tag{1.2.25}$$

where $A = (1 - \epsilon_{eff})^2 - 4r^2\epsilon_{eff}$

Viscous drag coefficient.

The vortex viscosity can be derived as:

$$\eta = \frac{\Phi_0 B}{\rho_{vm,1}} \frac{2\epsilon_{eff}}{1 + \epsilon_{eff} - \sqrt{A}} \tag{1.2.26}$$

This relation is model independent within the universal expression. Dependence from ϵ_{eff} means that only boundary value can be determined. η always falls in the range:

$$\eta_{GR} \frac{1 + \epsilon_{eff,max}}{2} < \eta < \eta_{GR} \tag{1.2.27}$$

where η_{GR} is obtained using the GR model, that is without taking into account the creep.

Both η_{GR} and $\epsilon_{eff,max}$ are directly calculated from experimental data. They limit the value of η and determine the error in its determination. Based on eq. 1.2.27 one can deduce that the application of the GR model to low temperature data with high r, where creep is thought to be small or negligible, yields more uncertain estimates of η. In this case it is true that $\epsilon_{eff,max}$ is small (and that the real ϵ_{eff} can be even smaller), but neglecting it altogether brings an error up to a factor of 2 on η.

Thus, estimates for η can be accompanied by significant error bars. Errors can be reduced by noting that the uncertainty on the creep factor, $0 < \epsilon_{eff} < \epsilon_{eff,max}$, does not uniformly reflect on η. Even in the worst case $\langle \eta \rangle \pm 20\%$

represents a 90% confidence interval, where $\langle \eta \rangle$ is the expected value of η.

Pinning constant.

The pinning constant is calculated by simple relation $k_p = \omega_p/\eta$, where the depinning frequency is determined by the model dependent relation [27]:

$$\frac{\omega_p}{\omega} = \frac{(1 - \epsilon_{eff} - \sqrt{A})(1 - \epsilon_{eff})}{2r\epsilon_{eff}} \begin{cases} \frac{I_0(u/2)}{I_1(u/2)}, & \text{CC} \\ 1, & \text{B} \end{cases} \qquad (1.2.28)$$

The value of k_p, determined by GR model, represents the lower limit, $k_{p,max}$ is model dependent, determined by eq. 1.2.28.

Within the Brandt model for $r \gtrsim 1$ the uncertainty on k_p is vanishingly small and $k_{p,max}/k_{p,GR} \simeq 1$. But in the Brandt model the creep factor is limited ($\epsilon \leq 0.5$), so that large creep regime can not be described. The CC model is able to capture both the low- and the high-creep regimes. However, an interpretation of the data within the CC model yields a larger uncertainty with respect to the Brandt model. The determination of the parameters (mainly k_p determination) and interpretation of the experimental data are dependent from the choice of the model.

Chapter 2

Measurement technique

In this chapter I illustrate the various measurements methods and describe the procedure of the data extraction from the measured quantity. In this work two methods were used, exploiting their complementary strengths: the dielectric resonator method, which works at a single frequency was chosen due to its high sensitivity and small size (which is useful for the small samples) and the Corbino disk, which is characterized by a lower sensitivity, but its capability of operating over a wide range of frequencies is especially useful.

Three systems for the measurement of the surface impedance were realized and used. First, a new measuring cell based on the dielectric resonator (DR) of the Hakki Coleman type operating at a single frequency 8 GHz was designed and setup. Second, DR of the same type, operating at 48 GHz [31] was upgraded to work in transmission. Third, the wideband measurements were taken with the Corbino disk. Finally, for future work a rectangular DR (RDR) was realized and tested to study the in-plane anisotropy of conducting samples. All these configurations and corresponding cryogenic systems are described in the next sections. Preliminarily, I describe the main principles and techniques for the surface impedance (Z_S) measurements measurements.

2.1   Surface impedance

The properties of the conductor in the electromagnetic system can be described by Maxwell equations. Consider an electromagnetic wave incident normally to a flat boundary vacuum/(super)conductor. The surface impedance of the medium is defined as:

$$Z = \frac{E_\parallel}{H_\parallel} \tag{2.1.1}$$

where the electric and magnetic field components are orthogonal to each other and parallel to the boundary.

This is a complex quantity which can be determined experimentally by performing high frequency measurements. In the linear regime the surface impedance is independent from the amplitude of the electromagnetic field and includes only the contributions from the sample properties.

The electromagnetic wave in a normal conductor decays exponentially on the characteristic penetration depth $\delta = \sqrt{2/(\omega\mu_0\sigma_n)}$, where σ_n is the conductivity of the normal metal.

For a normal conductor one can neglect the imaginary part of the complex conductivity. In that case the conductivity becomes real and equal to the d.c. conductivity $\sigma_{d.c.}$. Z_S can be rewritten as

$$Z_S = \sqrt{\frac{\omega\mu_0}{2\sigma_{d.c.}}}(1+i) \tag{2.1.2}$$

This relation is valid for the normal skin effect in conductors, where the penetration length is larger than the normal carriers mean free path and where the sample thickness t_s is much greater that the penetration depth of the impinging electromagnetic (em) field. It also states, that the real and imaginary parts of the surface impedance are equal for the normal conductor.

In a superconductor, general case Z_S can be rewritten as dependence from the complex conductivity [11]:

$$Z_S = R_S + iX_S = \sqrt{\frac{i\omega\mu_0}{\sigma}} \tag{2.1.3}$$

where R_S is the real part, named surface resistance and X_S is the imaginary part, named surface reactance.

Often, film samples are used for the study of Z_s of materials. They can be represented as layered structure as depicted in Fig. 2.1. They can also include very thin buffer layer(s) between the film and the substrate which will be neglected in the next description.

When $t_s \leq \min(\lambda, \delta)$ the relation for Z_s becomes more complex. This is due to the penetration of the electromagnetic field through the film sample and interaction with the substrate and any supporting layers.

For the general case of multilayer structure depicted in Fig. 2.1 the surface impedance is given by the effective quantity $Z_{s,eff}$ based on impedance transformation [32, 33]

$$Z_{s,eff} = Z_s^w \frac{Z_{d,eff} + iZ_s^w \tan(k_s^w t_s)}{Z_s^w + iZ_{d,eff} \tan(k_s^w t_s)} \tag{2.1.4}$$
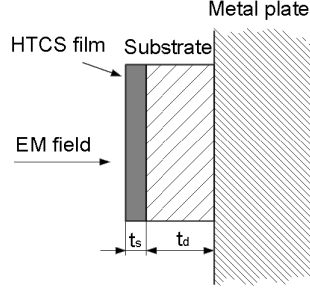
Figure 2.1: Layered structure resulting in a typical microwave measurement on thin films.

where $Z_{d,eff}$ is the effective surface impedance of the substrate, Z_s^w and k_s^w are the wave impedance and the wave propagation constant in the superconducting film. The latter two quantities exactly coincide with the plane wave Z_s and $k_s = \mu_0 \omega / Z_s$ for Transverse Electromagnetic (TEM) wave propagation, while for guided propagation (including the case of Transverse Electric (TE) operated resonators) in general they are given by the corresponding modal quantities. Let $\mathbf{k} = (k_\parallel, k_\parallel, k_\perp)$. The TEM approximation is justified when $k_\parallel \ll k_\perp$ [32]. This is often satisfied (including the case of TE operated resonators) and only in very particular arrangements the modal quantities differ significantly from TEM. From now on this approximation will be assumed and the "w" superscript will be dropped.

The effective surface impedance of substrate in general form can be represented similar to the film case taking into account the bulk impedance of the underlying metallic plate (Z_m) [34]:

$$Z_{d,eff} = Z_d \frac{Z_m + iZ_d \tan(k_d t_d)}{Z_d + iZ_m \tan(k_d t_d)} \qquad (2.1.5)$$

where Z_d is the characteristic impedance of substrate, which is material-dependent parameter; k_d and t_d are respectively the propagation constant and the thickness of the substrate.

In case $|Z_{d,eff}| \gg |Z_s|$ the substrate contribution can be neglected and equation (2.1.4) reduces to the intrinsic surface impedance of the film:

$$Z_{s,eff} \simeq Z_s^{(i)} = -iZ_s \cot(k_s t_s) \qquad (2.1.6)$$

which, if $t_s \ll min(\lambda, \delta)$, gives the so-called thin-film approximation:

$$Z_{s,eff} \simeq Z_f = R_f + iX_f = \frac{1}{\tilde{\sigma}_s t_s} \qquad (2.1.7)$$

There are various methods for the measurement of Z_S at microwave frequencies. The available methods include both resonant techniques (like cavity resonator, dielectric resonator (DR), microstrip line resonators etc.) and non resonant methods (like the so-called Corbino disk). Samples in the form of epitaxial films are better suited for microwave studies of intrinsic properties. In order to focus on intrinsic properties, techniques requiring sample patterning (for example coplanar line) were avoided.

2.2 Surface impedance measurement

Here I briefly review the main principles of the surface impedance measurements at the microwave frequencies. I describe with details the methods that were used in this work.

2.2.1 Resonant methods

Cavity resonator

Traditionally, cavity resonators are used for the Z_s measurements. The simplest structure of a cavity resonator is section of waveguide shortcircuited from both ends by flat conductors. Many cavity configurations are used; rectangular [35, 36], cylindrical, elliptical [37], conical [38]. They operate at single frequency in the range 1 GHz up to 120 GHz [39, 40, 41, 42, 43].

There are two methods of the surface impedance measurements using cavity resonators. One of them is surface perturbation technique, which is used for the study of the flat samples. Here, the sample replaces one of the cavity bases. Base replacement method allows to perform precise measurements only with sufficiently large samples to increase its impact in the response of the resonator. Small sized samples in form of the plate or single crystals can be studied by volume perturbation technique. This class included so-called hot-finger method [44, 45]. Here the sample is placed inside the cavity on a sapphire rod (see Fig. 2.2a). Sapphire rod is used to cool the sample separately from the cavity. Microwave currents are generated on both sides of the bulk sample. This technique allows to measure not only in-plane impedance but also axial impedance [44].

Cavity resonators are usually excited on the lowest order transverse electric TE or magnetic TM modes. In the rectangular and cylindrical cavities, which are widely used, correspondingly unidirectional and circular currents are induced on the flat surfaces. Electromagnetic fields in the cavity resonators due to the simplicity of geometry are well described in the literature, which simplifies its design process and operation.
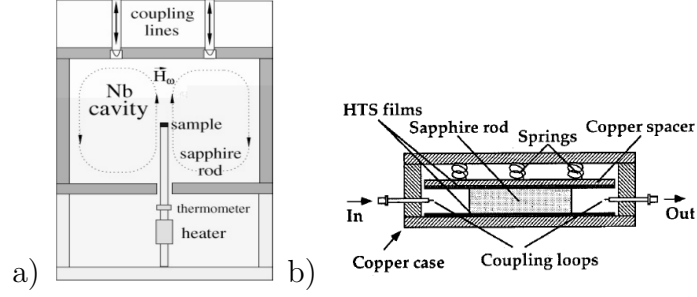
Figure 2.2: Schematic of two resonance measurement cells: the "hot-finger" microwave cavity (a) and shielded Hakki-Coleman resonator (b).

The main characteristics of each resonant system are the quality factor Q-factor, which is represented as relation between energy stored in the resonator to the losses, and resonant frequency. The losses in the cavity resonator come from the losses in the conducting walls and, depending from the cavity configuration from the radiated energy. The resonant frequencies of the cavity resonator depends on the relation between its dimensions and properties of the material, from which they are realized.

Resonators made from good conductors (copper, gold) have Q-factor of the order of 10^2-10^4. To improve the performance of a cavity resonator the superconductor can be deposited on the walls of the cavity (usually Nb). Use of low temperature superconducting material for the resonator walls the resonator application is limited in the temperature interval of the superconducting state, but increases Q up to 10^5.

The losses in the resonator are a sum of the losses in the conducting wall and superconducting sample. Losses in the conducting parts are proportional to the surface resistance. Experimentally the resistance of the sample can be extracted on the base of two measurements: with sample as one base and conducting base with known resistance [46].

Cavity resonators have a few advantages: relatively simple in design and realization; large Q-factor at low temperatures; possibility of the resonant mode tuning by holes or screws. To the disadvantages we could subsume sensitivity to the quality of the surfaces and cavity made by good conductor is needed (as example, oxygen-free copper).

Dielectric resonator

A main disadvantage of the cavity resonators is difficulty to measure samples with sizes compatible with the resonator size or small samples.

However, cavities made with a normal conductors are characterized by low

Q-factor and analysis of the experimental data becomes difficult. This can be avoided in the dielectric loaded resonators. This type of the resonator is made from dielectric and has a smaller dimensions, so the possibility of the smaller samples measurements is occurs, because electromagnetic fields are confined in the dielectric with the dielectric constant much higher than the dielectric constant of the medium in which it is enclosed. There are few commercially available dielectrics with high permittivity (ε_r) and low loss: sapphire $\varepsilon_r = 9.8$, rutile $\varepsilon_r = 100$, lantanium alluminate with $\varepsilon_r = 25$ and various types of ceramics. Here only real part of the permittivity is considered. Sapphire is widely used not only because it is characterized by high ε_r, but also due to its extremely low dielectric losses at microwaves.

Resonant frequency strongly depends on ε and the Q-factor is dielectric losses dependent. So during the dielectric resonator design, the choise of the proper material is needed and its parameter temperature dependencies have to be taken into account [47].

A typical configuration of dielectric resonator was proposed by Hakki-Coleman (H-C) [48] (Fig. 2.2b). It is used for the surface impedance and for the characterization of the dielectrics as a standard method [49, 50, 51, 52]. There are, also, configurations adapted for specific problems [53, 54, 55].

In H-C dielectric resonator the dielectric rod is clamped between two conducting bases or placed in the center of the cylindrical cavity. Typically the base replacement technique, where one or both bases are replaced by the sample, is used for Z_s measurements. H-C resonator is characterized by Q-factor of the order 10^6 at low temperature, and main losses are dielectric losses and losses in the sample. This type of resonator is usually excited on the fundamental TE or TM modes. Determination of the electromagnetic field distribution are more complicated with respect to the cavity resonator and sometimes numerical methods are needed.

The main part of electric and magnetic energies of the DR with the high ε dielectric are stored in the dielectric cylinder. Outside the dielectric an almost exponential decay of the electromagnetic field takes place. So effect of the base edges or the outer wall on the resulted Q-factor is minimal. To remove the radiation contribution completely outer walls can be used. It can be shown that the effect of the wall is negligible for high ε dielectric [56].

Planar resonator

Resonators based on the planar transmission line technique are interesting mainly from the applicative point of view. These resonators can be easily integrated with standard electronic devices in the printed circuits integrated in the microwave circuits. Superconducting planar resonators such as microstrip

[57] and coplanar [58, 59, 60, 61] are widely used for the superconductor surface impedance measurements in presence of magnetic field and for the study of nonlinear effects due to the self induced magnetic field in the sample. They can be made by deposition of the superconductor on the dielectric substrate surface. The resonator shape is created by lithography.

Planar resonators have a quite large Q-factor of the order 10^4 which allows to perform accurate measurements. This method has a big disadvantage, it is destructive. Each sample must be patterned in form of the resonator, preventing from the use for different measurements.

Microwave current in the planar resonators is concentrated in the region of the central conductor in the zone of patterned sample, so that the effect of the sample boundaries play a role. Constant sample thickness is also needed. Therefore precise preparation of the samples is needed to avoid additional contributions in the experimental data.

2.2.2   Nonresonant methods

Nonresonant methods of the surface impedance measurements are based on the measurements of the reflected or transmitted power through the superconducting sample or reflected from its surface.

Transmission type measurements are based on the detection of the power, transmitted through the sample. This method is not widely used due to the low sensitivity and need the complicated analytical modelling. In [62] and [63] this method is realized in the infra-red range. But at microwave frequencies some assumption of the infra-red analysis are not fulfilled. Measuring cell contains rectangular waveguide with propagated TE_{01} mode. The superconducting film sample on the dielectric substrate is placed perpendicular to the wavegude axis. To extract complex conductivity reflection from the boundaries of the sample has to take into account.

It was proposed a simplification of the power transition model stated in [63] for the case of the lossless dielectric substrate [64]:

$$T \approx \frac{2n}{Z_g d\sigma(ncos\beta l + jsin\beta l)} \qquad (2.2.1)$$

where $Z_g = n_0/\sqrt{1 - (1/2a\sqrt{\varepsilon_0\mu_0}f)^2}$ is the wave impedance of the air-filled waveguide; $\gamma \simeq j\sqrt{k^2 - (\pi/a)^2}$ and l are propagation constant and the substrate thickness; n is the refractive index.

Measurements of the reflected power are based on the setup where the superconducting sample short circuits the waveguide or coaxial cable. The reflected power gives the surface resistance of the sample.

The sample can be placed perpendicular to the metallic waveguide axis (E-plane structure). In this case the incident power is fully reflected and sensitivity of the method to the sample conductivity is minimal. It, also, can be placed at the grazing angle with respect to the sample surface. This improve the method sensitivity by 10 [65, 66].

Waveguide reflection method need the calibration to separate reflected signal from the sample and waveguide. Reflected power is expressed as:

$$R_m = E_D + \frac{R_a E_R}{1 - R_a E_S} \qquad (2.2.2)$$

where E_D, E_R, E_S - calibration coefficients, which are field and temperature dependent and $R = |\Gamma|^2$ is the parameter connected to the reflection coefficient.

The constants are determined by solving the system of the linear equations on the basis of three calibrating measurements with different conducting samples. This method is very sensitive to the waveguide surface quality and edges of the waveguide-sample contact, since they produce unrecognisable leakages and disturbing of the field. So only flat samples can be measured. Additional inconvenience is the necessity of the calibration measurements. However, this method allows to carry out broadband measurements in the range limited by frequency range of the waveguide operation.

Another type of the transmission line method was proposed by Corbino [67]. Corbino disk technique allows more flexible wideband measurements with respect to the waveguide one. Due to the low diameter of the coaxial cable, the measurements of small sample is possible. The coaxial cable range of operation is from the few MHz up to ten's of GHz. Here the coaxial cable is short circuited by the sample [68]. The sample is placed perpendicularly to the central conductor. TEM wave in the coaxial cable induces in-plane radial currents on the sample surface (see Fig. 2.3). As in the case of the waveguide termination, power leakages has to be avoided. A metallic plate is placed and pressed by spring in the backside of the sample.

The surface impedance is connected to the reflected signal by the well-known equation [69]:

$$Z_s = Z_0 \frac{1 + \Gamma_0}{1 - \Gamma_0} \qquad (2.2.3)$$

This method also needs for the calibration which can be performed by a second measurement with the normal conductor as a sample.
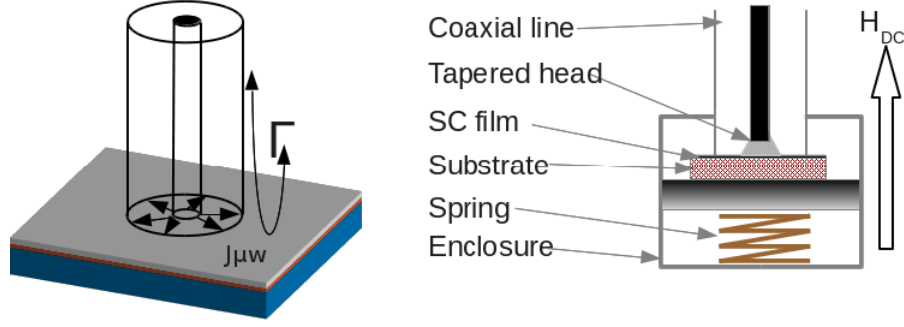
Figure 2.3: Scheme of the Corbino disk measuring cell

2.3 Principle of the DR measurements

Resonant systems are characterized by two parameters: the resonant frequency at which the stable electromagnetic field configuration exists and quality factor. Mode configuration is determined by solutions of the Helmholz equation with the boundary conditions which corresponds to the resonant structure [70].

The Q-factor takes into account the losses in the resonant system with respect to the stored energy. Larger Q-factor means that less power is dissipated in the elements of the resonator like dielectrics and conductors. Every resonant system can be characterized by the unloaded quality factor, which takes into account only the losses in the resonator. It can be represented as the relation between the power dissipated in the resonators elements, at the one period of the oscillation, and total stored energy:

$$Q_u = \frac{\omega_0 W}{P_r} \tag{2.3.1}$$

where $\omega_0 = 2\pi f_0$ is the angular resonant frequency; W is the energy stored in the resonator; $P_r = P_\Omega + P_D$ is the power, dissipated in the conducting parts (P_Ω) and dielectric elements (P_D).

The resonance system has also elements which are used for the coupling to the external circuits. Thus, the measured loaded Q-factor takes into account the losses in the elements of the transmission line and coupling elements. The loaded Q-factor can be written as:

$$Q_l = \frac{\omega_0 W}{P_r + P_{out}} \tag{2.3.2}$$

where P_{out} represent the power losses in the external line for one period of the oscillations.

The external Q-factor can be written as $Q_{out} = \frac{\omega_0 W}{P_{out}}$ and it represents the losses in the line. The relation for the losses is written as:

$$\frac{1}{Q_l} = \frac{1}{Q_u} + \frac{1}{Q_{out}} = \frac{1}{Q_u}(1 + \beta) \tag{2.3.3}$$

where β is the coupling coefficient.

If in the resonant system more than one coupling elements were used: $\beta = \sum \beta_i = \sum Q_{u,i}/Q_{out,i}$. Thus, the measured parameter of the resonator, coupled with the external circuit is the loaded Q-factor $Q_l = Q_u(1 + \sum \beta_i)$, where β_i is the coefficient which characterizes coupling of the resonator to the i-th external circuit. The coupling coefficient can assume the values: $\beta = 1$ which corresponds to the critical coupling, $\beta > 1$ is over-coupling and $\beta < 1$ is low coupling regime. Determination of the coupling coefficient is a complex procedure and additional elaboration of the experimental data are needed [71, 72, 73].

The error in the unloaded Q-factor is estimated by relation, determined by measured β and loaded Q-factor. For single coupling this relation can be rewritten as:

$$\frac{dQ_u}{Q_u} = \frac{dQ_l}{Q_l} + \frac{d\beta}{1 + \beta} \tag{2.3.4}$$

At low coupling ($\beta \ll 1$) the loaded and unloaded Q-factors are essentially equal. It is desirable to use low coupling to directly measure the unloaded Q-factor and error is determined only by the loaded Q-factor error. Therefore, in practice the coupling coefficient $\beta \to 0$ is preferable.

Another source of the losses in the resonator is the radiation of the electromagnetic energy in the open space, which has to be taken into account in the open resonance systems. The estimate of radiation Q-factor(Q_{rad}) in the practice needs additional measurements with different samples, which is difficult when a low-temperature measurements is performed. In closed resonator the radiation losses can be ignored ($Q_{rad} \to \infty$). In this work the closed resonators are used, so that, there is no need to take into account thee radiated energy.

As short summary, the following factors affect the unloaded Q-factor of the DR: dielectric losses due to the dielectric material polarization, which is defined by the loss tangent of the dielectric (P_d), the finite conductivity of the metal parts of the resonator (conducting losses (P_Ω)), the losses due to the power radiation (P_{rad})

The time average of the energy stored in the resonator is the sum of the electric (W_e) and magnetic (W_m) stored energies.

$$W = W_m + W_e = \frac{1}{4}\int_{V\,diel} \varepsilon_r' \varepsilon_0 |E|^2 dV + \frac{1}{4}\int_{V\,vacuum} \varepsilon_0 |E|^2 dV + \frac{1}{4}\int_{V\,diel + V\,vacuum} \mu_0 |H|^2 dV \tag{2.3.5}$$

where $\varepsilon_r = \varepsilon_r' + j\varepsilon_r''$ is the complex permittivity of the dielectric which fills the volume V_{diel}. At the resonant frequency $W_m = W_e$. Power losses are determined by perturbation technique. In this case ohmic losses are determined by the induced surface current (J_{sur}) which can be determined from tangential component of the magnetic field:

$$P_\Omega = \frac{1}{2}R_s \int_S |J_{sur}|^2 dS = \frac{1}{2}R_s \int_S |H_\tau|^2 dS \qquad (2.3.6)$$

where integration is performed on the conductor surface. Ohmic losses are proportional to the surface resistance, so in the ideal conductor $R_s = 0$ and losses are absent. Dielectric power losses are given by: $P_d = \frac{1}{2}\omega_0 \int_{Vdiel} \varepsilon_r'' \varepsilon_0 |E|^2 dV$

The inverse Q-factor value is determined by the losses. For conductive and dielectric losses one can obtain:

$$\frac{1}{Q_\Omega} = R_s \frac{\omega_0 W}{\frac{1}{2}\int_S |H_\tau|^2 dS} \qquad (2.3.7)$$

and

$$\frac{1}{Q_d} = \frac{\frac{1}{2}\omega_0 \int_{Vdiel} \varepsilon_r'' \varepsilon_0 |E|^2 dV}{\frac{1}{4}\int_{Vdiel} \varepsilon_r' \varepsilon_0 |E|^2 dV + \frac{1}{4}\int_{Vvacuum} \varepsilon_0 |E|^2 dV} \simeq k\tan\delta \qquad (2.3.8)$$

where $k \sim 1$ is the dielectric filling factor.

As noted before, the unloaded inverse Q-factor is represented as sum of the losses in the resonator's components:

$$\frac{1}{Q_u} = \frac{\sum P_{\Omega,i} + P_d + P_{rad}}{\omega W} = \sum \frac{1}{Q_{\Omega,i}} + \frac{1}{Q_d} + \frac{1}{Q_{rad}} \qquad (2.3.9)$$

Therefore the resulting equation for the resonator losses gives the possibility to measure the surface resistance using the resonator technique:

$$\frac{1}{Q_u} = \sum \frac{R_{s,i}}{G_i} + \tan\delta \qquad (2.3.10)$$

where i is the indication of i-th resonator's conducting element, G_i and $R_{s,i}$ are geometrical factor and resistivity of the i-th element correspondingly.

The resonant frequency strongly depends on geometry of the resonator and on the material properties and it can be determined only in form of the variation with respect to fixed parameter. The variation of the parameters is made with respect to the base value (value at fixed temperature, field etc.). There are few contributions which affect the resonant frequency shift. In the case of the real conductor, the resonant frequency is shifted due to the imaginary part

of the impedance of the conducting parts. Additional frequency shift component is due to the temperature variation of the permittivity of the dielectric component [56] or due to the thermal expansion. The change of the geometric parameters with temperature due to he thermal expansion is small with respect to other contributions and it is possible to neglect them. The resonant frequency shift can be written as:

$$\frac{\Delta f_0}{f_0} = -\sum \frac{\Delta X_{S,i}}{2G_i} - \frac{k}{2}\frac{\Delta\varepsilon_r}{\varepsilon_r} \tag{2.3.11}$$

2.4 Measurement technique

As it was discussed above, with the DR one can measure the absolute value of the surface resistance and only variations of the surface reactance. We consider the resonator of the Hakki-Coleman type. The dielectric rod is clamped between two bases and sample was placed between one base and the rod. In this structure the losses in DR can be represented as:

$$\frac{1}{Q_u} = \frac{R_{s,s}}{G_s} + \frac{R_{s,l}}{G_l} + \frac{R_{s,b1}}{G_{b1}} + \frac{R_{s,b2}}{G_{b2}} + \frac{1}{Q_d} \tag{2.4.1}$$

where $R_{s,s}, R_{s,l}, R_{s,b1}, R_{s,b2}$ are the surface resistances of the conductors and G_s, G_l, G_{b1}, G_{b2} are the geometrical factors of the sample, lateral wall and bases. $\frac{1}{Q_d} = tan\delta$ is the dielectric losses

The designed DR was made from the nonmagnetic material (copper for the 8.3 GHz and brass for the 48 GHz DRs). Therefore, their surface resistances are independent on the magnetic field. But, the temperature dependence of the resistivity has to be taken into account. Loss tangents of the dielectrics used are also constant in the field. In the DRs for the Z_s measurements dielectrics with loss tangent as small as possible are used.

To remove background contribution the study of the "homogeneous" resonator is needed. The difference between the unloaded Q-factors of the DR with superconducting sample and of the DR with sample as a normal conductor is:

$$\frac{1}{Q_{u,SC}} - \frac{1}{Q_{u,M}} = \frac{R_{s,SC} - R_{s,M}}{G_s} \tag{2.4.2}$$

or

$$R_{s,SC}(T,H) = R_{s,M}(T) + G_s \left[\frac{1}{Q_{u,SC}(T,H)} - \frac{1}{Q_{u,M}(T)} \right] \tag{2.4.3}$$

Since the surface resistance of the material from which the DR cavity is made, an additional uncertainties can arise.

Neglecting the dielectric losses simplifies the loss relation for the homogeneous resonator: $R_{s,M}(T) = (G_{sum})/Q_{u,M}(T)$, where $G_{sum} = G_s + G_l + G_{b1} + G_{b2}$

In applied magnetic field it is easier to measure variation of the surface impedance. For the variation of the surface resistance we can disregard the effect of the normal conductor:

$$\Delta R_s(T, H) = R_s(T, H) - R_s(T, \mathring{H}) = G_s \left[\frac{1}{Q_{u,SC}(T, H)} - \frac{1}{Q_{u,SC}(T, \mathring{H})} \right]$$
(2.4.4)

Resonant frequency shift is affected by the changes of the surface reactance and dielectric properties of the rod. We can write this frequency shift as sum of the contributions: $\Delta f_{0,m/d} = \sum \Delta f_{0,m} + \Delta f_{0,d}$, where $\Delta f_{0,m} = -f_0 \Delta X_{s,m}/2G_m$ are the conductive contribution and $\Delta f_{0,d}$ is the dielectric contribution.

Two measurements have to be performed to remove the wall, bases and dielectric contributions. One of them made with the superconducting sample, another - with the normal conductor as sample. Normal conductor sample must have the same dimensions as superconducting to leave electromagnetic field structure unchanged.

Measured resonant frequency shift in the resonator with superconducting sample is represented as sum of the contributions due to the finite inductance of the materials from which DR is made:

$$\frac{\Delta f_{0,s/m/d}(T, H)}{f_0} = -\frac{\Delta X_{s,s}(T, H)}{2G_s} - \frac{\Delta X_{s,m}(T)}{2G_l} - \frac{\Delta X_{s,m}(T)}{2G_{b1}} - \frac{\Delta X_{s,m}(T)}{2G_{b2}} - \frac{\Delta f_{0,d}(T)}{f_0}$$
(2.4.5)

For the resonator with normal conducting sample:

$$\frac{\Delta f_{0,m/d}(T, H)}{f_0} = -\frac{\Delta X_{s,m}(T)}{2G_s} - \frac{\Delta X_{s,m}(T)}{2G_l} - \frac{\Delta X_{s,m}(T)}{2G_{b1}} - \frac{\Delta X_{s,m}(T)}{2G_{b2}} - \frac{\Delta f_{0,d}(T)}{f_0}$$
(2.4.6)

Subtracting of this equations:

$$\Delta X_{s,s}(T, H) - \Delta X_{s,m}(T) = -2G_s \frac{\Delta f_{0,s/m/d}(T, H) - \Delta f_{0,m/d}(T, H)}{f_0}$$
(2.4.7)

This relation gives an opportunity to determine the surface reactance shift, but it still includes the contribution of the normal conductor.

We already discussed how to extract the surface resistance from the data. For the normal conductors real and imaginary pars of the Z_s are equal. Based on this statement it is possible to determine the reactance contribution in the Δf_0. Based on this we can determine that:

$$\frac{\Delta X_{s,m}(T)}{G_s} = \frac{\Delta R_{s,m}(T)}{G_s} \tag{2.4.8}$$

DR technique allows to determine the absolute value of R_s but only the shift in the reactive part. The absolute value of X_s can be determined by assuming, that in the normal state the sample is a normal metal, which has equal real and imaginary parts of Z_s.

2.5   Measurement systems

Measurements of the superconducting properties need the good thermal stabilization and possibility of the temperature controlling in wide intervals (from the temperatures given by the method of the cooling, up to the room temperature). In this work the cryogenic systems make use of cryoliquids (namely liquid Helium and Nitrogen). The regulation of the temperature is realized by controlling the current in suitable heaters.

The inner part of the cryostats has to be well isolated to avoid the heat exchange between the cryoliquids and external medium at room temperature. Usually this thermal isolation is realized based on the classical Dewar structure.

For the measurements in presence of the magnetic field the cryostats were realized using nonmagnetic materials mainly stainless steel adapted for cryogenic temperatures.

2.5.1   Liquid Helium Cryosystem

One part of the results in this thesis was obtained using a He-flow cryomagnetic system, which consists also the cooling system for a Nb_3Sn superconducting magnet.

In Fig. 2.4 the scheme and photo of the cryostat are shown.

In the the liquid helium cryostat the temperature variation between the helium bath and room temperature air is about 296 K. To reduce the heat flow through the vacuum isolation additional "layer" filled by liquid nitrogen is used.

The sample chamber is also separated from the liquid helium by vacuum isolation. This is needed to heat the measuring cell above the T=4.5 K and perform the measurements at varied temperature.
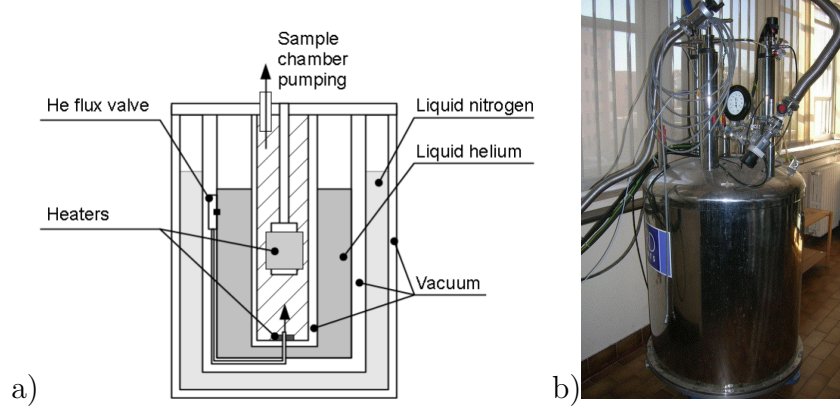
Figure 2.4: Scheme (a) and photo (b) of the liquid He cryostat with superconducting magnet

In the He-flow cryostat cooling is realized by the controlled flow of the cold helium gas from the chamber with liquid helium. For this purpose the pressure in the sample chamber has to be kept constant (P=500 mbar). This is realized by the gas pumping through the special valve.

Temperature of the measuring cell is controlled by simultaneous use of two heaters: two placed on the cell (for the heating of the resonator), another near the the helium flow valve (to control the temperature of the helium gas, which enters in the sample chamber). This allows precise variation the temperature of the sample from 4 K up to the room temperature without producing thermal gradients along the sample chamber.

Superconducting Nb_3Sn magnet is able to produce the magnetic field up to the B_{max}=12 T in the zone of the sample chamber. This magnet is integrated in the cryostat to be kept in the He bath. It is powered by the current generator Oxford PS120 with maximum produced current I_{max}=150 A with automatic control system to prevent the quenching effect (transition of the Nb_3Sn in the normal state). Value of the current sets the magnetic field based on the calibration curve, which depends on the cryostat construction. Placing of the sample inside the magnet bore allows to obtain the homogeneous magnetic field along the cryostat axis.

2.5.2 Liquid Nitrogen system

This DR based system operates at a frequency of 48 GHz and was designed to perform surface impedance measurements at temperatures of liquid nitrogen. In Fig. 2.5 the liquid nitrogen bath cryostat for the 48 GHz DR is shown. In the outermost chamber a $5 \cdot 10^{-6}$ mbar vacuum provides thermal insulation. The
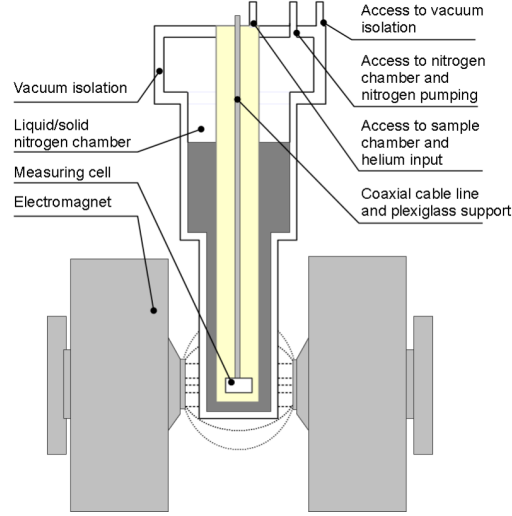
Figure 2.5: Cryostat for 48 GHz DR setup

intermediate chamber is filled by liquid nitrogen. Construction of this cryostat allows to reach the temperatures around 55 K by pumping the liquid nitrogen evaporation with rotary pump. The inner (or sample) chamber contains the cryogenic insert, which includes the resonator and the microwave line. Before the cooling down the air from the sample chamber has to be removed to avoid the effect of the ice on the measured data and remove the risk of microwave line destruction. After filling of the cryostat, inside the sample chamber a low pressure helium atmosphere is created (around 0.2 mbar) to make thermal exchange with the nitrogen bath.

The cryostat is inserted inside the air gap ($\sim$ 80 mm) of a conventional electromagnet (Bruker BE25V). This electromagnet allows to generate static magnetic field up to $\mu_0 H_{max}$=7000 G. It is powered by the stabilizated current source Bruker BSMPS-BIP1 with I_{max}=17 A. Besides two main magnet coils there are additional compensated ones to reduce the residual magnetic field, which appears during the magnetic field variation. The intensity of the magnetic field is detected by a sensor based on the Hall effect (placed in the middle between the magnet coils on the level of the sample) and measured by a gaussmeter Walker MG-3D. The magnet is installed on the rotatable base, which allows to vary the orientation of the magnetic field up to 360°.

2.6   8-GHz dielectric resonator measuring cell

This section presents the designed measuring cell of 8 GHz dielectric resonator.

This resonator was designed for the study of relatively small size super-conducting samples in presence of the extremal magnetic field. The DR was realized with special care to measurements of ΔZ_S (surface impedance variation).

The following requirements were taken into account during the design process:

- Samples under study have a form of squares with dimensions 5×5mm, with thickness 0.5 mm.

- Dimensions of the available cryostat bore: 50 mm in diameter and 1 m in the depth.

- Possibility of the measurements in the external magnetic field, which is axial to the resonator axis.

- High sensitivity of the DR and its structure as simple as possible.

Here the shielded Hakki-Coleman configuration of the resonator was chosen due to its high sensitivity and because its model is well described in the literature [70, 47].

The designed resonator is a cylindrical metallic enclosure containing a coaxially placed cylindrical dielectric rod of radius R_{diel} and height h_{diel}. The sample is placed between the dielectric cylinder and bottom conducting base. Top base is in contact with the dielectric rod. In this configuration the samples with different sizes (from the area covered by the dielectric cylinder up to the whole area inside the metallic enclosure, which is end-wall replacement technique) can be measured. This type of the resonator is excited on the fundamental modes. The TE_{011} resonant mode is selected because it is usually well separated from the spurious modes and due to the well known advantages of TE_{0np} modes like a high unloaded Q-factor and circular currents on the bases with no electric field component normal to the base there is no need for electric contact between bases and lateral wall, which is critical for the cavity type resonators.

In order to operate with small samples, the probing area has to be as small as possible. From other point of view, for the complex structure, the whole sample has to be probed and excluding of the boundary effects is needed. This means that the electromagnetic fields must be strongly confined into correspondingly small radial region in order to minimize the contribution not originating from the sample material itself and to reduce the effect of the sample boundaries. this can be done by choosing a dielectric material with high dielectric permittivity for the cylinder. For the resonator applications the material with low loss tangent is needed to decrease its effect on the loses in the

DR. The rutile (TiO$_2$), a high permittivity and low loss material (loss tangent tanδ=10^{-6} at liquid helium temperature), was chosen as dielectric. Being uniaxially anisotropic, rutile is characterized by different dielectric constants $\varepsilon_\perp$ and $\varepsilon_\parallel$ perpendicular and parallel to the anisotropy axis respectively ($\varepsilon_\perp$ =100, $\varepsilon_\parallel$=265 at liquid helium temperature) [75]. Its anisotropy has been taken into account both in design process and in the control of second order effects.

2.6.1   Geometry design

Design of the DR was performed using the model, basis of which are reported in [47, 76]. During the design process the balance between the needed geometry and performance of the resonator was carefully taken into account. The geometry of the resonator, namely height and radius of the dielectric cylinder, determines the resonant frequency and losses. The design of the geometry of the resonator was based on the following requirements:

- Resonant frequency is around 8.5 GHz at temperature 4.5 K, which is higher than the characteristic frequency of the flux motion in Nb (See experimental part).

- Reducing of the losses in the lateral wall of the resonator.

- Probing area high enough to probe the whole sample.

Due to the axial position of the measuring cell the maximum radial space can be used by the resonator. To reduce the effect of the lateral wall I choose the maximum possible radius of the cylindrical cavity. Taking into account the need of the heaters and spacers between the bore wall and the measuring cell, the outer wall diameter equal to 24 mm was chosen.

Operating with the small sized samples the peak of the TE$_{011}$ mode has to be inside the needed probing area. Under this conditions the effect of the boundaries can be neglected.

Starting from the simplest configuration of the DR where the sample thickness can be neglected. I choose and separate the area on the bottom base to simulate the sample contribution. This circular area has a radius 2.5 mm. Inside it I also mark out the area with diameter 2 mm as minimum needed area.

The TE$_{011}$ mode is the lowest mode excited in the DR and usually well separated from the spurious modes. In the homogeneous configuration the calculated resonant frequencies of the HEM and TM modes has to be far

away, thus there is no effect on the determination of the Q-factor of the TE mode.

The resonant frequency is determined by the dimensions of the dielectric cylinder and is not affected by the outer wall radius, much higher than the radius of the probed area. To keep the needed value of the resonant frequency the height and radius of the dielectric cylinder was optimized. By the simulation one can show that with increasing of the dielectric cylinder radius the resonant frequency decreases and the Q-factor of the resonator decreases. This reduction in the Q-factor is compensated by a higher cylinder. In the Fig. 2.6a the dimensions of the dielectric rod which correspond to the f_{res}=8.2 GHz are shown. Fixed radius (R_{diel}) gives the certain height (H), so, the parameter R_{diel}/H can be taken as independent.

Fig. 2.6b shows the variations of the losses in the DR at f_{res}. It can be shown that main part of the losses (around 50%) is in the upper base. Another half of the whole losses correspond to the area of the sample. And only 0.1% of the power is lost in the remaining part of the bottom conducting base. This calculation was performed using the homogeneous configuration of the DR, where copper was taken for all conductive materials. Copper was chosen because it is nonmagnetic, with low resistivity (R_S=0.16 Ω at 8.2 GHz). Low resistivity of the copper allows to increase the Q-factor by decreasing the losses in the upper base.

It was shown that due to the large radius of the outer wall its effect is negligible. Concentration of the induced current inside the probed area with radius 2.5 mm minimizes the effect of the bottom base. Low losses in the bottom base means lower disturbance of the electromagnetic field by the boundaries of the presupposed sample.

The central part was fixed in diameter of 2 mm to show the effect of the mask which can be applied to improve the general Q-factor of the resonator by increasing of the geometrical factor of the probed sample surface. To avoid the effect of the mask the maximum of the surface current has to be chosen between the circular area uncovered by the mask and maximum needed sensed sample surface (which is in form of the circle with diameter 5 mm).

Thus the main part of the losses has to be in the zone on the sample surface between the two circles of diameter 2 mm and 5 mm. A large radius of the dielectric can be an advantage from the point of view of the mechanical stability of the resonator due to the high diameter of the outer wall.

In the Fig. 2.7 the current density on the sample surface along the coordinate axis is shown. It can be seen that maximum of the current density is always inside the area covered with the dielectric rod. This is due to good confinement of the electromagnetic field caused by the high dielectric permit-
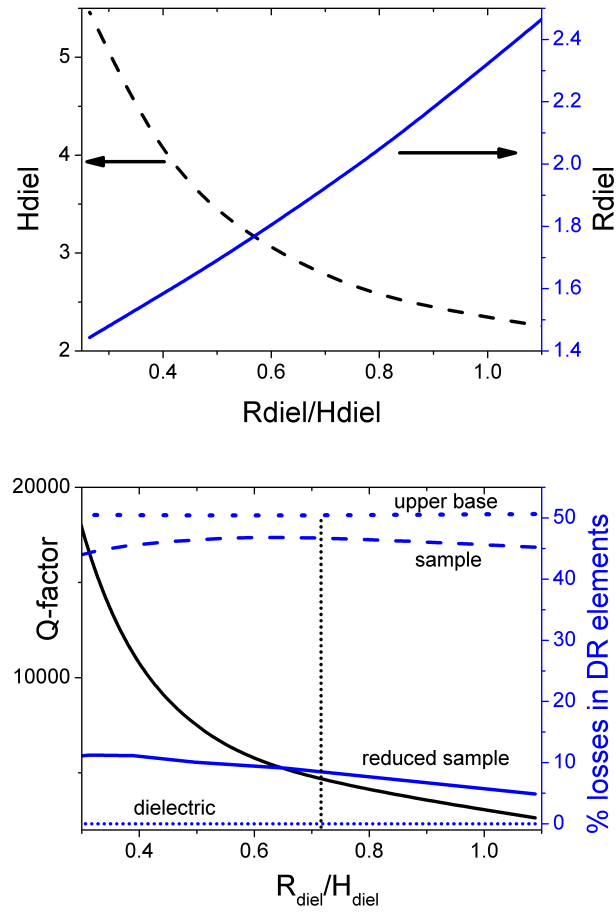
Figure 2.6: (a) R_{diel} and H depending from the aspect ratio R_{diel}/H which corresponds to the f_{res}=8.2 GHz; (b) Losses in the various parts of the DR as dependence from the aspect ratio R_{diel}/H
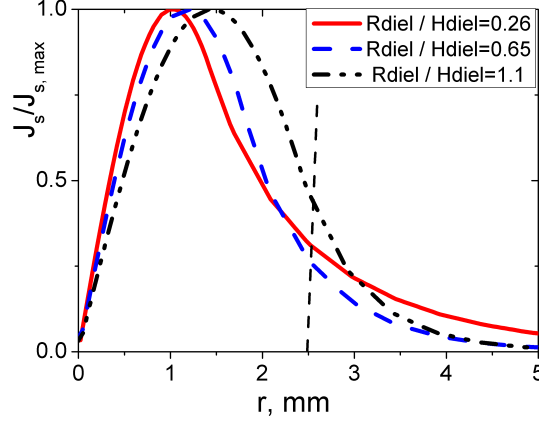
Figure 2.7: Induced current density vs. R_{diel}

tivity of rutile. Outside of the dielectric rod the induced current density decays nearly exponentially.

A dielectric rod with height 2.77 mm and diameter 3.88 mm was chosen as a result of design goals taking into account the dimensions of the sample and of the available cryostat. Resonant frequency, which corresponds to this dimensions is 8.4 GHz at temperature 4 K. Spurious modes are in the distance around 300 MHz, which allows to obtain good shape of the curve for the resonator Q-factors starting from 200. The corresponding geometrical factors of the sample and upper base are G_s=6500 and G_{b2}=265.

2.6.2 Measuring cell design

In this section I show the main components of the measuring cell. In Fig. 2.8 the draft of the DR-based cell is shown. The dielectric rutile rod is placed axially in the center of the outer wall. The upper base is fixed by screws to the outer wall. The bottom base was realized in form of a spring-loaded piston. The sample under study is placed on the bottom base surface. The dielectric rod is placed on the sample surface. Attention has to be given to the centering of the sample and dielectric rod. The decentering leads to non reproducible results and problems with the optimization of the coupling. In this case the resonant curve is not a Lorentz one and determination of the parameters of the resonator becomes difficult. Using specially developed centring tools the position of the dielectric rod can be tuned.

All metallic parts of the cell were worked out in copper. The internal surfaces of the DR were polished to avoid the effect of the scratches and oxi-
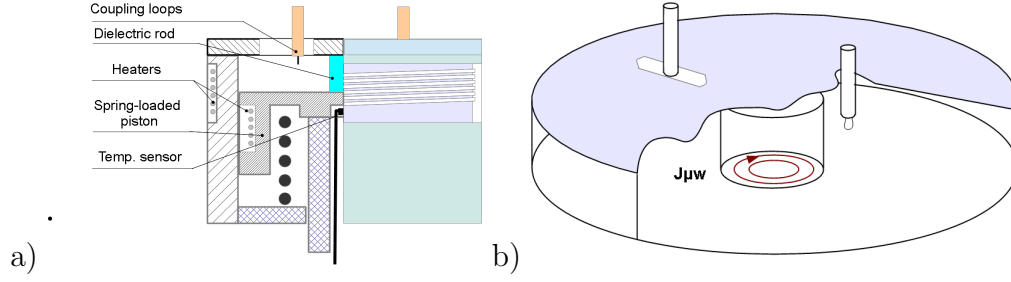
Figure 2.8: (a) Draft of the front view of the measuring cell; (b) 3D view of the DR without outer jacket

dizing on the metal surface. This increases the Q-factor of the DR. Dielectric rod was also bought with optically polished surfaces to avoid the additional disturbances of the electromagnetic field.

Heaters, used for the thermal stabilization, were realized by the noninductive resistive windings. One heater coil was placed in the piston. The rutile is a bad thermal conductor, so that thermal coupling between two bases is low. To reduce the possible temperature gradient between the bases, the second heater was placed around the outer wall near the upper base. The heaters were connected in parallel, which allows the simultaneous heating of both bases.

This resonator was realized to work in transmission. Thus, two ports are needed for the coupling. Coupling between the resonator and the external microwave line was realized through loops made with a central part of the coaxial cable short circuited on the outer conductor. This type allows to couple with the magnetic field line of the TE_{011}. It was found that optimal coupling was realized with the coaxial cable loops placed near the upper base, where the magnetic field of the TE_{011} mode has only radial component. To minimize the effect of the coaxial cables on the characteristics of the DR, coaxial cables with 0.8 mm diameter were used. Appropriate loop diameter was determined experimentally and was equal 1.5 mm. Coaxial cables were inserted through holes in the upper base of the shielding cavity. This insertion allows to use maximum space of the cryostat bore for the resonator.

For the resonator working in transmission the minimization of the coupling coefficients is needed to perform measurements of the unloaded Q-factor without additional calibration procedure. The resonant curve shape is, also, sensitive to the difference between the coupling coefficients β_1 and β_2. In this measuring cell a mechanism for the tuning of the coupling was developed. This mechanical system allows to adjust and control the axial and radial position of couplers. In this way, coupling coefficients β_1 and β_2 can be tuned to do the
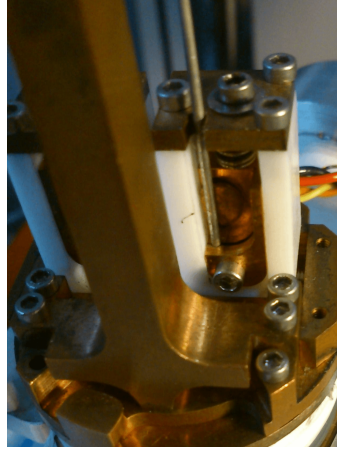
Figure 2.9: Photo of the mechanical tool for the coupling adjustment

resonance curves as symmetrical as possible. In Fig. 2.9 the photo of the tool for the tuning of the coupling is shown.

The coaxial cable inserted in the tuning mechanism is fixed in the clamping tool. This clamping tool can be realized using teflon or copper. It was shown in practice that the teflon clamping tool fixes well the axial position of the coaxial cable, but rotation of this cable is unavoidable. The copper clamping tool can fix this problem, but it can lead to the coaxial cable damaging when large clamping force is applied. Experimental study of the reflected signal of the coaxial cables inserted into the clamping tool shows that there are no inhomogeneities produced due to the overpressed cables, which were used in the measurements.

Cryogenic measurements give the risk to damage the metallic parts due to the difference in the thermal expansion coefficients of the materials. Part of the coaxial cables outside the measuring cell were shaped in form of the spring to compensate for the mechanical stresses due to the temperature gradient between the measuring cell and transmission line of the cryogenic insert.

A Cernox temperature sensor for controlling of the sample temperature is used during the thermalization process. The sensor is placed inside the piston in the bottom of the sample and separated from it by the 1.5 mm copper wall. Copper is a good thermal conductor, this leads to a negligible difference of the temperatures between the sample and sensor. The temperature sensor was also isolated from the outer space by a teflon covering. This allows to avoid the additional cooling of the sensor by the liquid He evaporations.

The 8.3-GHz DR was specifically designed for the cryostat with magnet, which generates the field perpendicular to the sample surface. The temperature of the coaxial cables was controlled by an additional temperature sensor

placed in contact to the surface of one coaxial cable (Fig. 2.10). A vector network analyser (VNA) is connected to the resonator by means of coaxial cables (single mode operation up to 40 GHz). The VNA, temperature sensors, heaters, magnet power supply and cryogenic liquids levels were PC-controlled by Labview programs via a GPIB (IEEE-488) bus.

2.6.3 Calibration

During the measurements, the main calibration issue is related to the density of calibration points, which needs to be sufficiently high to ensure an accurate determination of the resonators Q-factor and of the resonant frequency. Since the dielectric resonator operating frequency changes with the temperature, this implies the availability of a sufficient number of calibration points in wide frequency range.

The measuring of the Q-factor is performed based on the determination of the width of the resonant curve:

$$Q_l = f_{res}/\Delta f \qquad (2.6.1)$$

where Δf is the bandwidth of the resonant system which is measured on the levels 0.5 for the measured curve in power, 0.707 - for the voltage and 3 dB if the resonant curve is measured in dB.

The resonant frequency can be determined precisely by the maximum of the resonant curve. But error of the Q-factor determination directly depends from the resonant bandwidth error. Bigger Q-factor corresponds to the low bandwidth. This needs more precise determination of the bandwidth.

The transmission line has two parts, the low temperature part inside the cryostat and the room temperature part (Fig. 2.10). Calibration of the transmission line was performed by separate calibrations.

The microwave line up to cryostat was calibrated at room temperature using standards (Open, Short and Load) on the basis of full 12-term transmission line calibration [77]. Before low temperature measurements 12 error coefficients were determined from 4 measurements with Open, Short, Load and Thru standards (Anritsu or HP) with known line characteristic. The procedure of the determination of the error coefficients is described in Appendix A. During the measurements, using the previously determined error coefficients an offline calibration was performed. Low temperature measurements were performed without applying calibration on the VNA. All calculations concerning calibration are carried out using LabView acquisition programs explicitly developed.
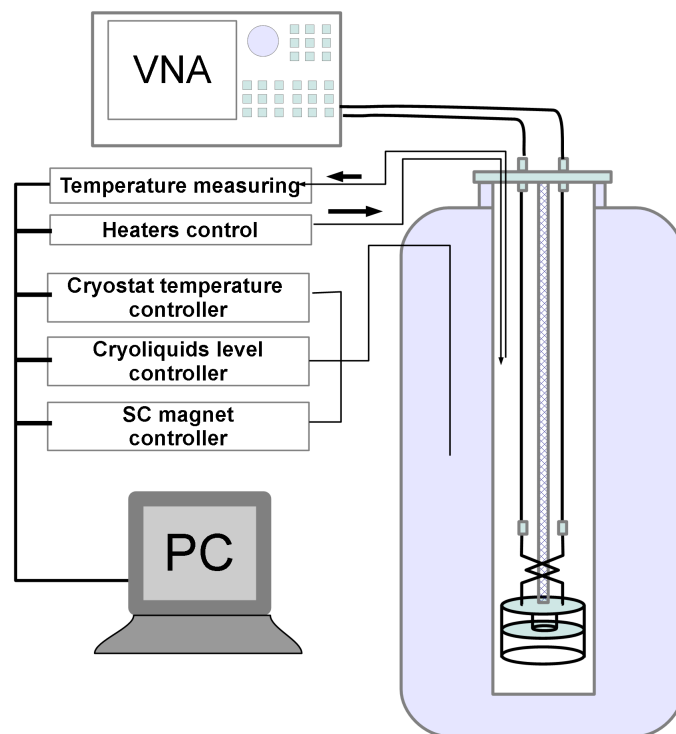
Figure 2.10: Scheme of the measurement system

Measured resonance curve points are affected by error coefficients which are frequency dependent. The accuracy of calculations is determined by the number of experimental points around the resonance. However, using calibration process on the VNA we can use only 1600 calibrated points. Using LabView calibration module we can reduce resolution of the calibration by collection of the calibration data and by applying interpolated error coefficients frequency dependence. The offline calibration is limited only by the VNA frequency range and by the time needed for calibration. It is impossible to fully calibrate the transmission line at liquid helium temperature and we take into account only loss level in the low temperature part. We show that the calibration affects the resonant curve through the S_{11} and S_{22} backgrounds. In the transmission mode, due to much better signal-noise of S_{21} as compared with S_{11}, the resonance is not much affected by the calibration. S_{21} error can be easily decreased by calibration, non zero constant background level does not strongly affect on the Q_l determination and easily can be taken into account in process of the fitting by Lorentz curve.

2.6.4 Improving of the operation at room temperature

The dielectric resonator measuring cell was designed based on the assumption that the sample is a good conductor (namely copper). As it was shown before, the geometrical factor of the sample is G_s=270 and equal to the geometrical factor of the upper base. The superconductor in the normal state is a bad conductor. It lowers the general Q-factor of the resonator and makes difficult the tuning of the resonator. To improve the response of the measuring cell with installed superconducting sample in the normal state, the geometrical factor of the superconducting sample has to be increased. This can be done by applying the masks or patterning of the sample surface. Thus part of the surface is covered by the conductor, another part remains the superconducting. In order to keep DR method non-destructive the patterning can not be used. Thus for masking, a thin metallic mask with circular hole was proposed. The mask was made from the thin aluminium foil with thickness 0.02 mm. Aluminium was chosen as nonmagnetic material with quite high conductivity.

Circular currents induced by TE_{011} mode has no radial component. Therefore the circular shape of the hole and small thickness of the mask were chosen to not disturb the induced currents. The circular hole diameter was determined experimentally to keep the balance between the increased geometrical factor of the sample and possibility of its realization in practice.

To increase more the effectiveness of the DR a spacer between the sample and the rutile cylinder was applied. Application of the spacer allows to increase the Q-factor and geometrical factor of the sample [78, 56]. Teflon (ε=2.4)
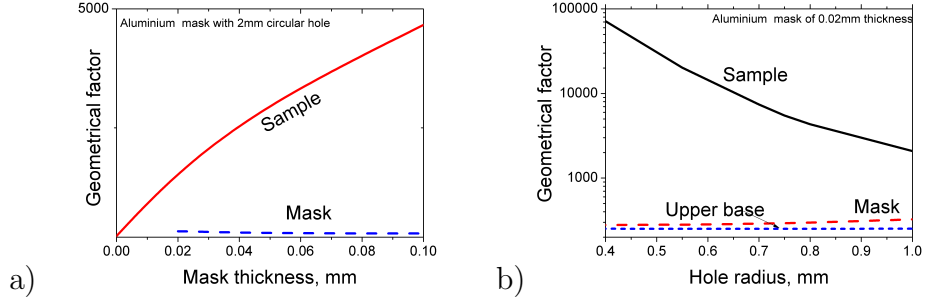
Figure 2.11: Effect of the mask thickness (for the mask with 2-mm hole) (a) and central circular hole (for the mask of 0.02mm thickness) (b) on the geometrical factors of the DR parts; b)

spacer with thickness 0.2 mm was used for this purpose. The spacer fully covers the surface of the mask. This allows to keep the mask flat due to the rigidity of the used Teflon. Here the sample, placed on the bottom base, is covered by the mask with circular hole. Teflon spacer, which is placed on the mask, keeps this mask flat and creates the gap. In Fig. 2.11 the effects of the mask thickness and circular hole (in the center of the mask) diameter on the geometrical factors of the DR elements are presented.

2.6.5 Low temperature test

The designed DR was tested at low temperature. This section represents the results of this test and defines more exactly the measurements procedure. As it was noted before, the configuration where the sample is masked and teflon spacer is added, is more suitable for the measurements of the superconducting samples. First I consider the configuration where the sample under study is the normal conductor (homogeneous configuration). In Fig. 2.12a the frequency sweep measured at room temperature is shown. A comparison of the measured data and calculated ones shows good agreement concerning TE_{011} mode (around 1%). TE_{011}, on which the resonator operates, is characterized by the unloaded Q-factor around 2000 and resonant frequency f_0=9.425 GHz with respect to the calculated Q_u=3500 and f_0=9.43 GHz. Nearest modes are the modes of the HE type with dominated electric field line component perpendicular to the bases. The spurious modes are excited due to the coupling of the elongated part of the coaxial cable loops with its electric field lines. The difference between the spurious modes and TE_{011} is around 90 MHz which is acceptable for the mode with Q-factor higher than 2000. Comparison in Fig. 2.12a shows that group of the simulated spurious modes is shifted with
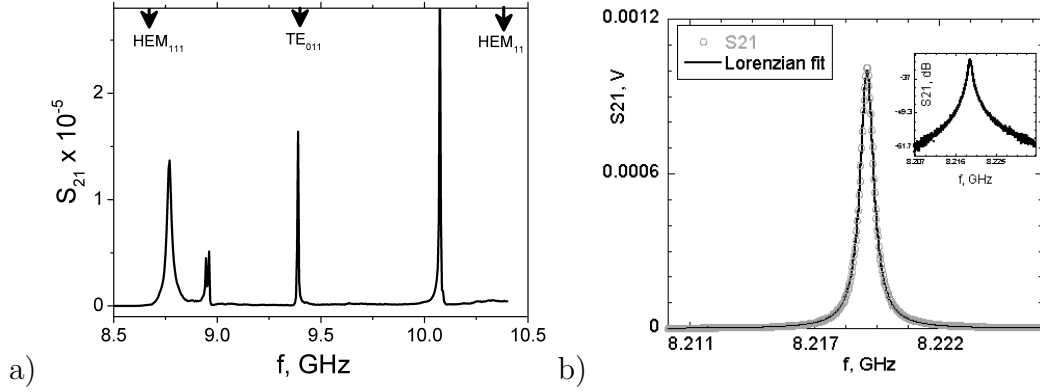
Figure 2.12: a) Comparison of the simulated spectrum and measured at room temperature one of the homogeneous DR. b) Resonant curve of the homogeneous DR: measured at temperature 3 K and its lorentzian fit, in the inset - measured resonance curve in dB

respect of the measured one by $\sim$300 MHz. This is due to the more simple resonator structure which was used in the simulation: holes, scratches and effect of the couplers were not taken into account. Full wave simulation of the small size elements strongly depends from the used grid, therefore increasing of the mesh nodes leads to the increasing of the calculation time.

Parameters of the DR were calculated taking into account the dielectric constant and loss tangent temperature dependencies for rutile from [75].

Two DR were tested at low temperatures: homogeneous configuration and simplest Hakki-Coleman type. In Fig. 2.13 the temperature dependencies of the resonant frequency and quality factor are shown. It is clear that increasing of the height of the cylindrical DR leads to the decreasing of the resonant frequency. Additional spacer does not affect the TE_{011} mode configuration and slightly deforms the field distribution of the spurious modes. To completely remove the spurious HE modes, thicker spacer is needed, but thick spacer from only one side of the dielectric cylinder transforms TE_{011} into the quasi-TE mode, where induced current has a normal to the sample surface component.

With decreasing of the temperature, the Q-factor increases from 2000 up to 11000. This dependence is due to the decrease of the metallic parts conductivities and loss tangent with temperature. The decrease of the resonant frequency is due to the increase of the dielectric permittivity of the rutile cylinder (both $\varepsilon_\perp$ and $\varepsilon_\parallel$) and by the change of the conductive parts reactance.

Let us consider the method of the determination of the surface impedance of the superconducting sample based on the measured Q-factors and resonant frequencies. First I take the relation for the losses in the resonant system (see eq. 2.4.1). For the DR with mask, spacer and superconducting sample
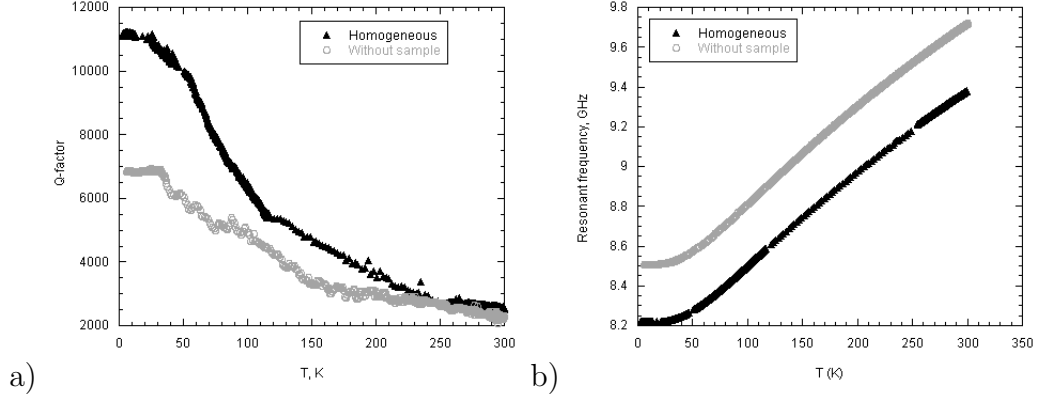
Figure 2.13: Temperature dependencies of the parameters of the DR in homogeneous configuration compared with the Hakki-Coleman configuration: a) Quality factor; b) resonant frequency.

(operating configuration), the losses can be divided in two parts: connected to the sample losses and background contribution. The latter contribution includes the losses in the normal metal lateral wall, bases, mask and losses in dielectric elements. As it was shown before, losses in the lateral wall are less than 0.5% of the whole losses in the resonator ($G_l=1.2 \cdot 10^{10}$) and we can neglect them. It is possible to neglect the effect of the bottom base with $G_{b1}=4 \cdot 10^4$, since this is one order higher than the superconducting sample geometrical factor.

The resulting relation can be rewritten as:

$$\frac{1}{Q_u} = \frac{R_{s,s}}{G_s} + background \qquad (2.6.2)$$

where $background = \frac{R_{s,mask}}{G_m} + \frac{R_{s,base}}{G_{b2}} + ktg\delta_{rutile}$ $R_{s,mask} = R_{s,Al}$ and $R_{s,base} = R_{s,Cu}$ are the surface resistances of the aluminium mask and copper upper base; G_s and G_{b2} are their geometrical factors. The coefficient $k \sim 1$ is the rutile dielectric cylinder filling factor.

Here I neglect the effect of the dielectric losses in the teflon spacer because of its much smaller reflection coefficient with respect to rutile, and because of its small filling factor.

The background contribution is temperature dependent, but independent from the magnetic field. It can be determined from the measurements with homogeneous DR.

Thus, to obtain the absolute value of the surface resistance two additional temperature measurements are needed. One of them with DR without sample to determine $R_{s,Cu}$, another - with homogeneous configuration of the DR to

take into account surface resistance of the mask $R_{s,Al}$.

$$\frac{1}{Q_u} - \frac{1}{Q_{u,hom}} = \frac{R_{s,s}}{G_s} - \frac{R_{s,Cu}}{G_s} \qquad (2.6.3)$$

$R_{s,Cu}$ can be determined by the the measurements without sample within the approximation used before and taking into account that the geometrical factor of bases approximately equals the one for the upper base (in case of the configuration without sample). From these measurements the copper surface impedance can be defined as:

$$R_{s,Cu} = \frac{G_{b2}}{2Q_{u,H-C}} \qquad (2.6.4)$$

The resulting surface resistance of the superconducting sample becomes:

$$R_{s,s} = G_s \left[\frac{1}{Q_u} - \frac{1}{Q_{u,hom}} + \frac{G_{b2}}{2Q_{u,H-C}G_s} \right] \qquad (2.6.5)$$

In the variation of the imaginary part of the surface impedance it is possible to neglect the contribution from the lateral wall. The resonant frequency shift, originating from the variation of the dielectric cylinder dimensions with temperature, can be easily neglected for rutile, with thermal expansion coefficients $\alpha_\perp = 7.14 \cdot 10^{-6} K^{-1}$ and $\alpha_\parallel = 9.19 \cdot 10^{-6} K^{-1}$, due to its smallness with respect to the another contributions ($\propto 1$ Hz/K) [79].

For the resonator with normal conducting sample:

$$\frac{\Delta f_0}{f_0} = -\frac{\Delta X_{s,s}}{G_s} - background \qquad (2.6.6)$$

where $background = \frac{\Delta X_{s,mask}(T)}{G_m} - \frac{\Delta X_{s,base}(T)}{G_{b2}} - \frac{\Delta f_{0,d}}{f_0}$ and $X_{s,mask} = X_{s,Al}$ and $X_{s,base} = X_{s,Cu}$.

The main contribution in the background is due to the dielectric permittivity temperature variation. However, the contribution from the normal metal induced frequency shift cannot be neglected at low temperatures, where the dielectric constant of rutile is almost temperature independent. Fig. 2.14 reports the comparison of the resonator frequency shift with contribution from the conductive base (multiplied by 10). As we can see, metallic part contribution is 1000 times smaller of the whole frequency shift ($\frac{\Delta f_0}{f_0} \sim 10^{-4}$). But it still comparable to the measured X_s for the superconductor.

Therefore the background contribution can be taken into account using the measurements made with homogeneous DR configuration with the sample made with the same material as bases. Extraction of the measured $\frac{\Delta f_0}{f_0}$
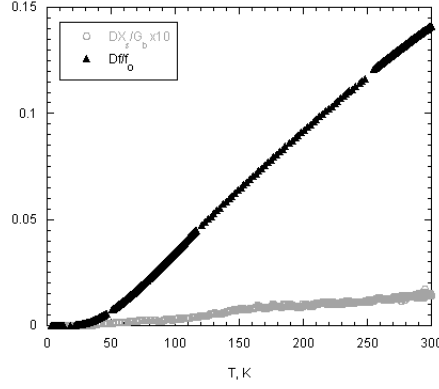
Figure 2.14: Measured in the homogeneous DR configuration resonant frequency shift compared with the contribution from the conductive base

with homogeneous configuration allows to extract the superconducting surface reactance shift.

For the resonator with normal conducting sample one obtains:

$$\Delta X_{s,s} = G_s \left[\frac{\Delta f_0}{f_0} - \frac{\Delta f_0}{f_{0,hom}} + \frac{\Delta X_{s,Cu}}{G_{b2}} \right] \qquad (2.6.7)$$

$\Delta X_{s,Cu}$ can be determined based on the measurements with DR without sample. Since, for the normal conductor $X_s = R_s$, using eq. 2.6.4 one can obtains:

$$\Delta X_{s,Cu} = R_{s,Cu} = \frac{G_{b2}}{2Q_{u,H-C}} \qquad (2.6.8)$$

As a result, based on the three measurements one can determine the absolute value of the surface resistance and the temperature variation of the surface reactance. With known conductivities of the DR parts this procedure can be shortened to one measurement with superconducting sample. An example of the measured surface impedance temperature dependence with the previously described DR is shown in Fig. 2.15.

2.7 Upgrade of 48-GHz dielectric resonator

Here I describe the upgrade of the previously existing 48 GHz measurement system, based on a nitrogen bath cryostat and rotating electromagnet. Surface impedance measurements were done by using a cylindrical dielectric loaded resonator, which worked in reflection before modifications and is excited on the TE_{011} mode at the resonant frequency of $\sim$48 GHz [31].
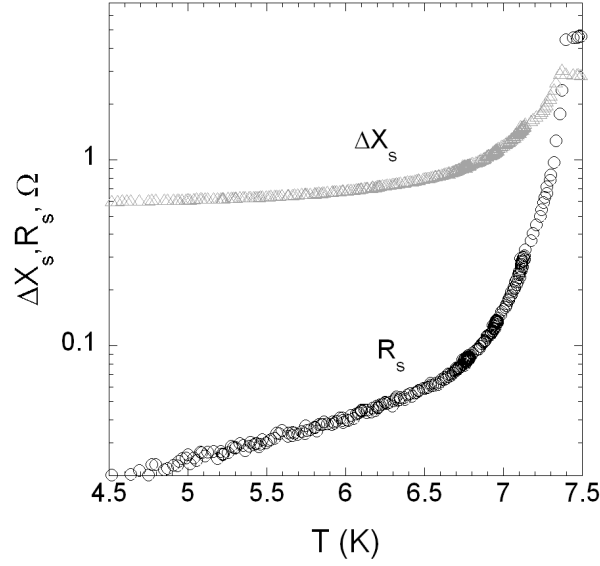
Figure 2.15: Real and imaginary parts of the surface impedance of the 20-nm Nb film measured by 8.2 GHz DR

2.7.1 Pre-existing configuration

Before describing the upgraded system I show the main elements of the pre-existing system. The higher operational frequency is outside the limit of VNA, thus the microwave circuits are different.

The microwave circuit is depicted in Fig. 2.16a. The microwave line is based on the synthesized HP-83751B source, equipped with a multiplying head 83556A. The power source operates in the frequency range 40-60 GHz with an output power up to 11 dBm and frequency stability $\propto$1 KHz. A U-band waveguide connects the power source, the power detecting crystal diode and, by means of a vacuum pass-through, the waveguide that is located inside the cryostat together with the cavity. To minimize the heat flow through the waveguide the section had a very thin metal walls reinforced by carbon fiber. The circulator directs the generated wave towards the resonator and deviates the wave reflected by the resonator towards the crystal detector. A ferrite isolator protects the power source from reflected waves.

The microwave power source is controlled by the NI-DAQ acquisition card and a IEEE 488 interface, controlled by Labview program. Each frequency sweep, set with a 0.1 s duration, is now initiated with a software primary trigger sent to the synthesized source. The source then generates the frequency sweep and simultaneously emits 1601 secondary triggers evenly spaced in frequency:

a)

b)
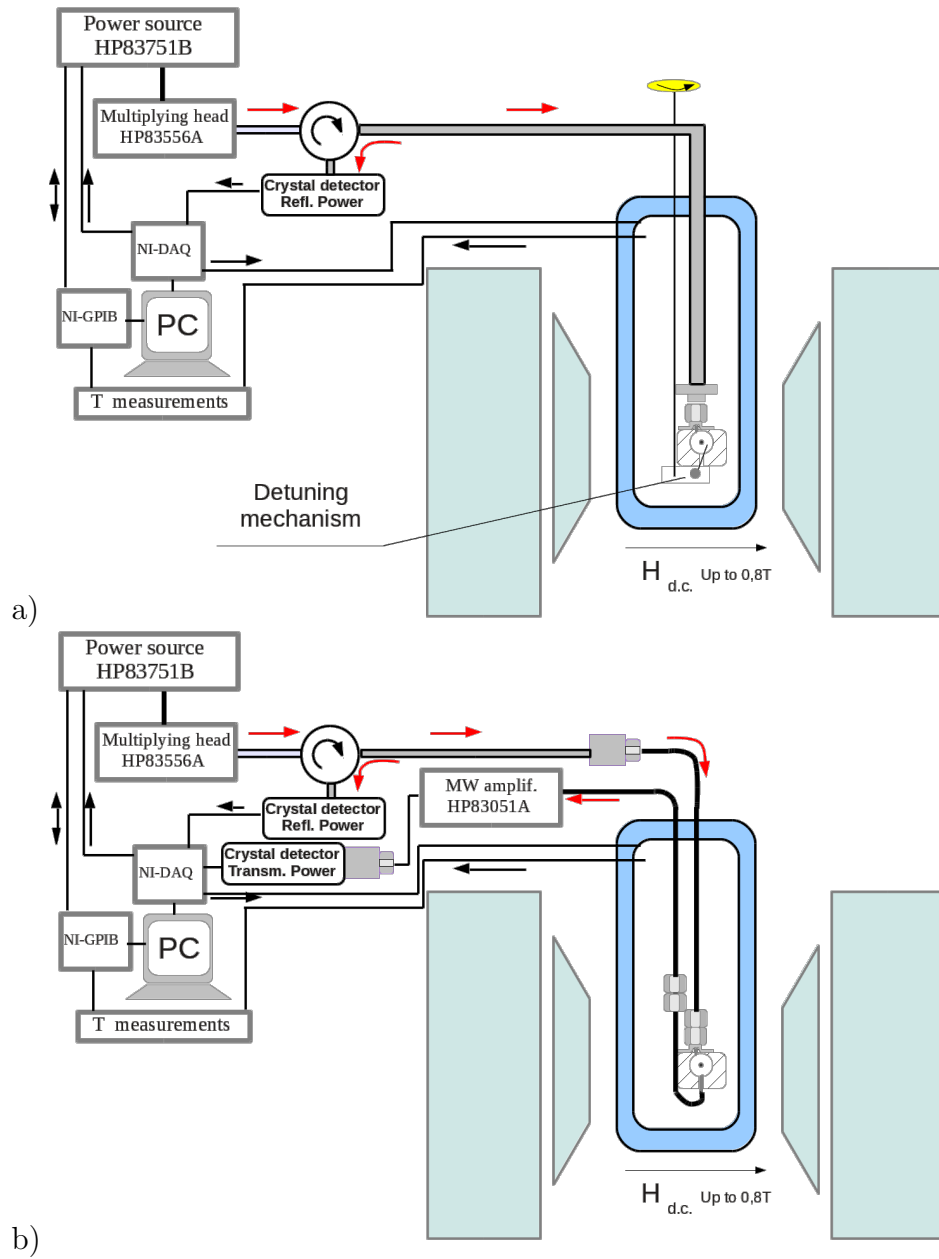
Figure 2.16: Diagram of the 48 GHz microwave circuit.

each one of them triggers the DAQ to take a reading of the power detected by the crystal diode. The corresponding frequency values are calculated by dividing the frequency interval by 1601. The latencies in the synchronization determine uncertainties on the frequency points less than 350 Hz, which can be safely neglected. Magnetic field intensity and temperature reading and controlling was realized through IEEE-488 interfaces. All measured data was elaborated by LabView software and recorded.

The measuring cell, based on the 48 GHz sapphire dielectric resonator, is shown in Fig. 2.17a. The sample replaces upper base and is pressed by thick brass disk with incorporated Cernox temperature sensor and spring through an outer pressing cage on the top of the metallic supporting case. Metallic parts of the DR were realized with monmagnetic material (brass). The metallic surfaces which forms the DR were, also, polished.

The sapphire rod is pressed against the sample by means of a spring loaded piston. Two heaters made with high resistive anti-inductive windings is located on the metal upper disk and on the piston. All the metallic parts were worked out in non-magnetic brass.

The resonator was excited in the TE_{011} mode to induce circular currents on the sample surface. Coupling with electrical field lines was used and realized by a tiny antenna.

For the line calibration a special detuning mechanism has been developed. A detuning mechanism consists a 0.5-mm diameter metallic post, which can be inserted and retracted through a small hole in the lateral wall (Fig. 2.17a). The insertion and extraction are operated from outside the cryostat. Fully inserted post couples and totally suppress the resonating mode. In this case the background can be measured and recorded. The resonator operates in the normal (resonant) regime only with extracted post. The resulting Lorentz curve is obtained by subtracting the background from the measurements performed in normal regime [31].

2.7.2 Upgraded measuring cell

The main goal of this upgrade is the improvement of the measurement process. A disadvantage of the previously described reflection type measurements is connected to the need of difficult calibration process and periodic tuning of the DR from outside the cryostat.

The measurement in reflection requires a detuning during the measurement process to remove the large temperature-dependent background and to obtain the resonant Lorentz curve (Fig. 2.18a). This requires the measurement of two curves for each data point at given temperature, so that the thermal stability becomes critical for the calibration accuracy. The system was modified to
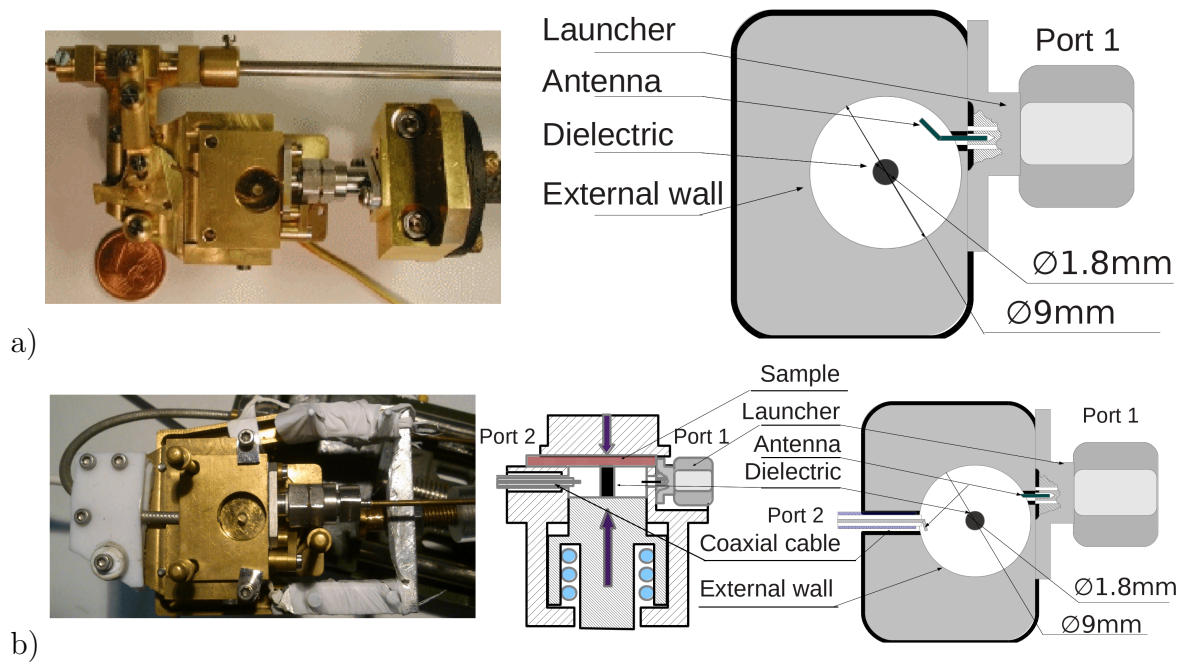
Figure 2.17: Scheme of the 48 GHz measuring cells operate in reflection (a) and in transmission (b).
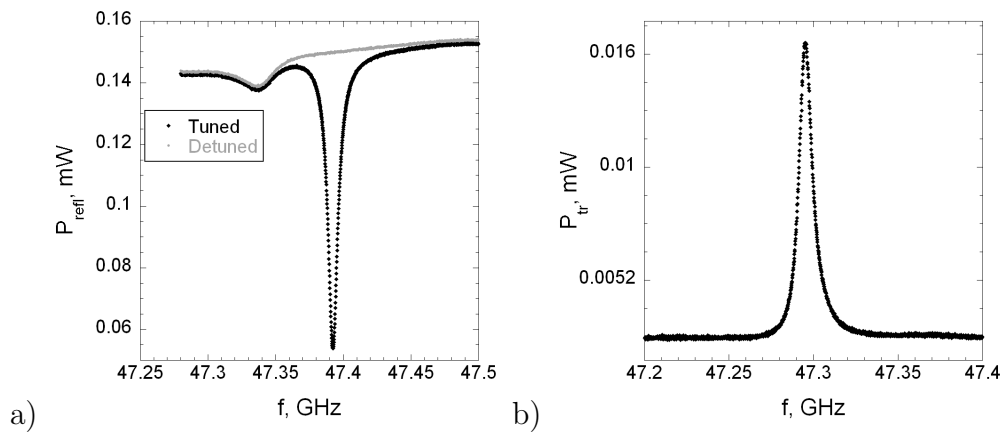
Figure 2.18: The response of 48-GHz DR measuring cells operate in reflection (a) and in transmission (b).

work in transmission in order to reduce the issues related to the calibration of the microwave line at cryogenic temperatures. Indeed, in transmission type measurements only one sweep is required which directly yields the resonant curve (Fig. 2.18b). The background of the transmitted signal is small and constant, originated by non-idealities of the components of the transmission line and by cross coupling between the resonator ports. Hence, the system was modified by adding a second coupler to the DR and by duplicating the whole microwave line, which connects the DR to the external excitation and measurement system.

Fig. 2.17b shows a schematic drawing of the dielectric resonator. The dielectric resonator is based on a sapphire rod placed in the centre of the cylindrical nonmagnetic conductive enclosure and bounded between two conductor bases. The sample to be measured is placed between one of the bases and the dielectric cylinder. The design of the DR allows to concentrate circular currents in the centre of the sample and to exclude the effect of the boundaries and gaps between upper base and resonators outer wall [80].

In the reflection type measurements, single port coupling was realized using a probe, which was inserted in the central conductor of a coaxial V launcher (Wiltron V103F), shown on the Fig 2.17a [80]. The microwave field of the probe is coupled with azimuthal electric field lines. The coupling were a trade-off between the need of reducing external losses and of high enough SNR. Pre-existing resonator coupling was tuned in order to have a coupling coefficient $\beta_1 = 0.1$, using an antenna shaped tangentially. The unloaded Q-factor is determined from the measured loaded Q-factor (Q_l) as $Q_l = Q_u(1 - \beta_1)$. Thus, also the temperature dependence of the coupling coefficient β_1 is required.

Measurements in transmission require two couplers (ports). In addition, to perform precise measurements coupling as small as possible is needed to avoid crosscoupling. Low coupling coefficients $\beta_{1,2}$ allows to obtain the unloaded Q_u directly from the measured Q_l ($Q_l = Q_u$ if β_1, $\beta_2 \ll 1$). Also the balance between coupling and amplitude of the signal is essential. In order to obtain smaller coupling coefficients, the coupling type was optimized. The existing coupling was reduced down by using a shortened straight antenna. The modified antenna enters in the metallic enclosure for a length of 0.3 mm (with respect to the 1.5mm in previous setup) and yields a coupling coefficient $\beta_1 = 0.06$.

In the upgraded configuration the detuning mechanism is not needed, and it was removed. It place was taken by by a custom-shaped coaxial cable, which operates up to 60 GHz. A special teflon fixing tool was, also, developed. The coaxial cable is located precisely in the middle plane of the DR to obtain better coupling with TE_{011} mode and it is electrically isolated from the body of the

resonator using teflon isolation. The second port is realized using the elongated central part of a coaxial cable working as an antenna coupled to the azimuthal electric field of the resonant mode (Fig. 2.17b). The coupling coefficient of the second port was tuned to be equal to β_1.

2.7.3 Cryogenic insert

The cryogenic setup is depicted in Fig.2.16b. A d.c. magnetic field can be applied with an angle with respect to the normal to the sample surface that can be varied by manually rotating the magnet. The measuring system required the addition of a second microwave line needed to connect the second coupler of the DR to the external system.

The pre-existing microwave line was based on a rectangular waveguide. The available cryostat allows to mount the cryogenic insert with maximum radial dimension 50 mm. Using two waveguides with U-band V-coaxial transitions leads to the increase of the cryoinsert diameter above the available space. V-type coaxial cables were used to reduce the transversal size of the line.

Since coaxial cables are characterized by a larger attenuation (with respect to the waveguide), an amplification of the transmitted signal becomes necessary. A microwave amplifier HP83051A working in the frequency range 45 MHz - 50 GHz was used. The amplified signal is then detected by a crystal detector, which gives the value of the power transmitted through the DR. A waveguide-coaxial transition couples the low temperature part of the line with the synthesized power source HP83751B equipped with a multiplying head HP83556A. A circulator directs the generated wave towards the resonator and deviates the wave reflected by the resonator towards a second crystal detector, which yields the power reflected by DR.

The acquisition process is controlled by Labview software. Typical frequency sweep time is 200 ms. The frequency sweep is initiated by the computer, which sends the primary trigger to the HP power source through a NI-DAQ card. The HP power source is programmed through GPIB connection. Voltage signals from the crystal detectors are collected using the NI-DAQ card, which also receives the frequency sweep signal from the power source. All calculations concerning calibration and Lorentz curve fitting are carried out using LabView acquisition program in real time.

The calibration of the transmission line was performed off-line using so-called Thru calibration technique. It is well suitable for the measurements of the absolute values of the transmitted power. Before the series of the measurements the calibration is performed with coaxial cables of the cryogenic insert line connected together with a section of zero-length coaxial line. High resolution measurements of the microwave power transmitted through the coaxial

line with variation of the temperature (from 60 K up to 300 K) were performed. By this way the temperature independent amplitude-frequency characteristic, which represents constant background due to the losses in transmission line, is obtained and calibration is performed.

2.8 Rectangular dielectric resonator

In this section I propose a method of the generation of the linear current on the surface of a superconducting sample using a dielectric resonator (DR) in form of a parallelepiped. While the technique of the rectangular dielectric resonator (RDR) is well known in the context of the antenna application due to big percent of the radiated power and magnetic dipole like radiation [81], in these cases only one side of the RDR is covered by the conductor, while the other sides are radiative (open ends). Partially metallic covered RDR is also widely used in filters [82]. I have apply to a relatively unexplored sphere of the complex resistivity measurements in presence of strong magnetic fields. In order to use RDR for the surface impedance measurements on superconducting systems, the main design requirements are the following: the DR has to operate at cryogenic temperatures in presence of magnetic fields; the resonant mode must be chosen to induce straight currents on the sample surface; Q-factor as large as possible are needed and the relevant mode has to be well separated in frequency from nearby modes.

2.8.1 Measuring cell

For the antenna application dielectrics with $\varepsilon \sim 10$ are used to increase the radiated power. As opposed to the antenna application of the rectangular DR (RDR), the dielectrics with high dielectric constant are needed in order to confine the electromagnetic field inside the resonator and to reduce the radiated power from the open ends of the dielectric. At a fixed frequency range, high ε implies small dimensions, which, in turn, make critical the design of the couplers (in terms of size, shape, positioning), their tuning and the sample mounting. Therefore the balance between the resonator dimensions, Q-factor and the frequency range have to be kept.

Two commercially available high ε dielectric materials were chosen: isotropic dielectric ($LaAl_2O_3$) with dielectric constant ε=24.5 and loss tangent tg$\delta = 6 \cdot 10^{-5}$ (at T=70K); anisotropic rutile (TiO_2) with dielectric constant along shorter side $\varepsilon_\perp$=170 and another side dielectric constants $\varepsilon_\parallel$=86.3 with tanδ=10^{-5} (at T=70K).

For the study of in-plane anisotropy, the straight microwave currents have

to dominate on the sample surface. It can be easily shown that the design of the RDR used for antenna application (with only one metal covered surface) is not suitable for the straight current generation, since it has a lowest mode TE_{111}, which can induce curved currents only.

A feasible design choice is to use a RDR in which 3 lateral sides are covered by conductors and one with the sample under study. The remaining two opposite open-end-faces (OEF) are used for the coupling (Fig. 2.19). This RDR structure is characterized by two fundamental modes: TE_{011} and TE_{101}, where two first indexes shows the electric field variations along the axis parallel to the OEF (x, z) and the third index shows the electric field variation along the direction between OEFs (y). In particular, TE_{011} gives the desired straight currents on the sample surface, while TE_{101} does not, but has to be checked in order to avoid interferences and superposition with TE_{011}.

Realization of the conductive covering can be done by sputtering of the metal on the dielectric surface to create the thick layer of the conductor with thickness higher then the length of the normal skin effect. This type of covering has a main disadvantage, which consists in the finite conductivity of the covering and impossibility to use the dielectric in another systems.

I propose to use a removable metallic covering, instead of sputtering of the metallic particles. This can be realized either or by conductive foil with a thin layer of glue or by clamping the thick metallic foil to the dielectric surface. It was shown that the glue particles on the surface only slightly decrease the resonator Q-factor. The glue also introduces the gap. The effect of the gaps between dielectric and covering is discussed in the following subsections.

The designed cell consists of the dielectric in form of the parallelepiped placed in the centre of a cylindrical copper cavity with radius much higher than the dimensions of the parallelepiped. The sample is placed between the lower base and dielectric. To cover 2 sides of the dielectric parallelepiped a special tool for the covering of the two opposite sides of the dielectric was developed and realized using nonmagnetic materials. It consists of flat teflon support of thickness 2 mm, in the lateral side of which two brass screws with diameter 1.2 mm are inserted. As a result one side of the dielectric is covered by the sample, the opposite side by the upper base of the cavity, the two sides which are perpendicular to the sample surface are covered by the micro-clamping tool with the copper foil. A photo of the DR used for the room temperature measurements is shown in Fig. 2.21a.

The selected TE_{011} mode would give ideally straight currents only for a waveguide DR, where dielectric is totally enclosed within infinite conductive surfaces. With two OEFs, the current lines develop a curved path mainly outside of the region of the sample covered by the dielectric. To separate
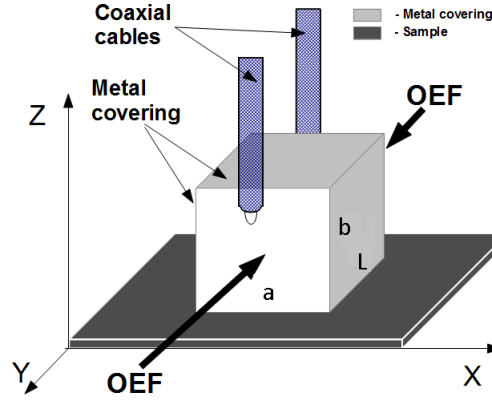
Figure 2.19: The rectangular metal covered DR configurations with two OEFs.

the "homogeneous" part of the currents and except the effect of the metallic covering edges we can use thin metallic masks on the sample surface with an aperture in the central part of the dielectric.

Given the typical sample sizes (from $5\times5\text{mm}^2$ to $10\times10\text{mm}^2$), additional design requirements are needed. I fix the minimal area of the straight current region, which should be $1.5\times1.5\text{mm}^2$. The straight currents region can be defined requiring a maximum tilting of the current from the desired direction equal to $J_{\mu w,\parallel}/J_{\mu w,\perp} = 3\%$, where $J_{\mu w,\parallel}$ and $J_{\mu w,\perp}$ are the current densities along the desired direction and perpendicular to it, respectively.

The coupling with open rectangular DR can be performed using coplanar waveguide or microstrip line [83], dielectric image waveguide [81], coaxial cable antenna with electrodes (sometimes deposited on the DR surface) [84]. I used coaxial cable loops, created from the central part of tiny coaxial cables, for the coupling with magnetic field-lines of TE_{011} mode in the covered RDR. Coaxial cables were put perpendicular to the sample surface within a circular enclosure with the diameter much bigger than the rectangular DR dimensions. Coupling with TE_{011} mode was performed with the loop surface placed parallel to the OEFs. The TE_{101} mode coupling can be realized by 90° rotation of the coaxial cable loops (Fig. 2.19). This configuration of the measuring cell is compatible to the measuring cell created for the 8.3GHz circular DR, which makes measurement process more flexible.

The RDR operating in transmission was made to improve quality of the measurements (Fig 2.19). Differently from the antenna application of the rectangular DR, where only one source of the microwave signal is needed, for the the transmission type measurements two couplers are needed. This demands two open end-faces (OEF) instead of single one.

Rutile is an anisotropic material. Its anisotropy was used to decrease the radiation of the electromagnetic field from the OEFs and reduce the current component perpendicular to the desired current direction. Since neither TE_{011} nor TE_{101} have component of the electric field lines normal to the OEF, there is no effect of the axial component of ε on the resonant frequency. In this case the models for the isotropic dielectrics can be used for the resonant frequency estimation. Electric and magnetic field lines of TE_{011} mode in the RDR are shown in Fig. 2.21b.

2.8.2 Geometry design

The metallic covering allows to describe this RDR as section of a dielectric-loaded waveguide. This type of resonators is widely used as a base for filters. In spite of the simple structure, the analysis of the resonant parameters is difficult and analytical relations adapted for the certain configuration are used. In the Appendix B I show the main relations which describe the electrodynamics of the waveguide DR. Here the simple structure, where the dielectric in form of the parallelepiped is put in the infinite (along the direction parallel to l) metallic waveguide, is used.

Estimate of the resonant frequency can be done by solving of the characteristic equation presented in Appendix B. As first approximation for this equation, a simple relation for the TE_{mnp} mode resonant frequencies (where OEFs are represented as a perfect magnetic wall) can be used [85]:

$$\omega_0 = \frac{1}{\sqrt{\mu\varepsilon}}\sqrt{(m\pi/a)^2 + (n\pi/b)^2 + (p\pi/l)^2} \qquad (2.8.1)$$

being a, b and l the sides of the parallelepiped, of the isotropic RDR.

Then using the characteristic equation shown in Appendix B, resonant frequencies of the TE and TM modes, which are mainly excited at lower frequencies, are calculated. As example for the TE_{011} mode the characteristic equation is as follows [86]:

$$\sqrt{\frac{\varepsilon_r - \frac{\lambda}{\lambda_{cr}(m,n)}}{1 - \frac{\lambda}{\lambda_{cr}(m,n)}}} \tan\left[\left(1 - \frac{\lambda}{\lambda_{cr}(m,n)}\right)L\right] = \begin{cases} \cot\left[\left(\varepsilon_r - \frac{\lambda}{\lambda_{cr}(m,n)}\right)l/2\right] \\ -\tan\left[\left(\varepsilon_r - \frac{\lambda}{\lambda_{cr}(m,n)}\right)l/2\right] \end{cases}$$
$$(2.8.2)$$

where a, b and $l \ll L$ are sides of the dielectric parallelepiped; $\lambda_{cr}(m,n)$ is the cutoff wavelength of the waveguide without dielectric. Upper and lower right-side relations in the brackets correspond to the non-even modes (p=2N+1, where N=0,1,2...) and even modes (p=2N, where N=0,1,2...).

In the RDR the waveguide sections approximation can be applied only for rough calculations. Overall, the effect of the boundaries of the metal covering and of the anisotropy of the dielectric has to be taken into account for the complete design of RDR. In this case the estimate of the parameters of the RDR (such as resonant frequency and Q-factor) can be performed by numerical methods since there is no general analytical equation available for the real geometry of the considered rectangular DR.

During the design process two requirements were considered:

- The TE_{011} mode has to be well separated from the TE_{101} mode and spurious modes;

- The TE_{011} mode has to be excited at a high resonant frequency (to have the possibility to perform the measurements above characteristic frequency of the superconductor in the vortex state).

To choose the dimensions of the dielectric, the simulation was performed numerically using the finite element method by commercially available packages. Based on performed simulations, the dimensions of the dielectric were chosen to have the TE_{011} mode (at the frequency near 7 GHz) well separated from TE_{101} and other spurious modes. In Fig. 2.20 the mode chart of the anisotropic, rutile-based RDR is shown. Variation of a affects the TE_{011} mode f_{res} and Q-factor but its effect on TE_{101} is negligible. Similarly the effect of the variation of b is much more visible on the TE_{101} mode. This fact validates that the wavegude approximation is applicable for RDR. Based on the calculations, the region, where the modes are well separated, was chosen. The Q-factor of the TE_{101} mode is independent from a and increases with increasing b from 1200 at 2 mm to 2200 at 5 mm.

The dimensions for the isotropic $LaAl_2O_3$ parallelepiped are $3.9 \times 3.5 \times 4.7$ mm, for anisotropic rutile $3.7 \times 3.1 \times 3.08$ mm, where first, second and third value are dimensions along x, z and y correspondent. In the following I focus the attention mainly on the rutile based RDR due to its applicative advantages. RDR with $LaAl_2O_3$ will be used to validate obtained results.

Table 2.1 shows the comparison of the resonant frequencies calculated with analytical models based on the dielectric loaded WG [87, 82] and determined using finite elements model. This comparison validates the resonant frequency obtained with finite elements simulations. It shows that the WG resonator approximation can be used for the mode resonant frequency identification in the RDR where the covered dielectric is clamped between two conductive bases, which is the model of the measuring cell under development (Fig. 2.21a), within 2.3% of error. Effect of the rutile anisotropy (where the anisotropy axis was
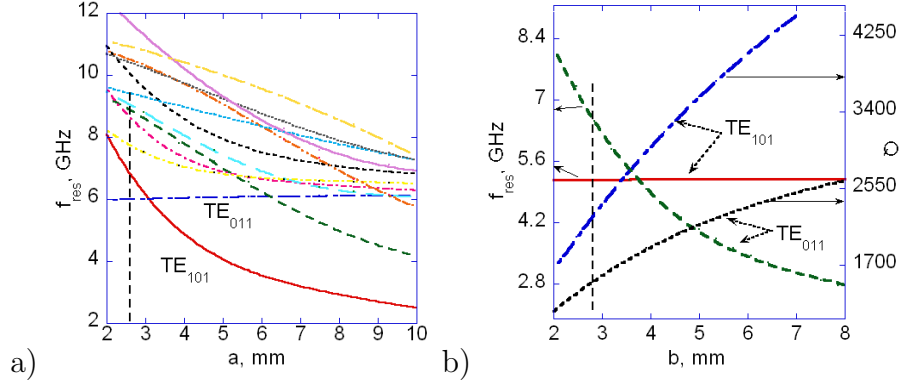
Figure 2.20: RDR mode chart at fixed b dimension (a). Resonant frequencies and Q-factor of the TE_{011} and TE_{101} modes (b).

positioned along the shorter side of the dielectric) is visible only for TM modes and can be neglected in f_{res} determination of TE modes.

Table 2.1: Comparison of the resonant frequencies determined by analytical (WG model) models and FEM simulation for covered rutile RDR with $\varepsilon_\perp = 86$ and dimensions 3,7×3,1×3.08 mm

Mode	Two OEF RDR WG model [87, 85] Res.Freq, GHz	Two OEF RDR (Simulation) Res.Freq, GHz	Two OEF RDR in cyl. cavity Res.Freq, GHz	Two OEF RDR in cyl. cavity with anisotropic rutile ($\varepsilon_\parallel = 170$) Res.Freq, GHz
TE_{101}	5.385	5.385	5.18	5.18
TE_{011}	6.19	6.19	6.05	6.048
TE_{111}	7.7	7.69	7.56	7.55
TE_{102}	8.31	8.306	7.96	7.942
TM_{111}	8.622	8.56	8.57	7.11
TE_{012}	8.97	8.97	8.72	8.7
TE_{112}	10.24	10.25	9.96	9.91

As a result, for RDR made from $(LaAl_2O_3)$, the calculated resonant frequencies of the TE_{101} and TE_{011} modes are 8.1 GHz and 8.9 GHz respectively. For the rutile-based DR the TE_{011} and TE_{101} frequencies are 6.05 GHz and 5.18 GHz, respectively.

For the correct identification of the experimentally observed modes, comparison of the experimental data and results of the modelling is needed.

The prototype was tested at room temperature. In Fig. 2.21d the experimental results at room temperature of the RDR prototype are shown and compared to the simulation results. The calculated Q-factor of the TE_{011} mode is 1600 and higher compared to the experimentally observed Q-factor, which is 300. But a good agreement (within 5%) between the computed and measured resonant frequencies can be observed.
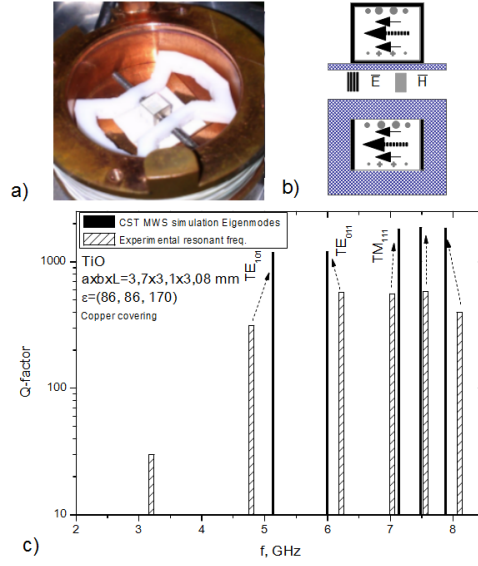
Figure 2.21: Photo of the experimental cell (a) and TE_{011} (b) modes of the "covered" rectangular DR with two OEF. (c) comparison of the calculated and experimental data (TE_{011} was excited in the RDR).

Calculation of the Q-factor of the resonator is more complicated since it depends on the geometry of the resonant system. Q-factor of the RDR in cylindrical cavity can be estimated by simulation. In this case WG approximation can be used for the determination of the geometrical factors of the metal parts which are directly cover the dielectric sides.

The unloaded Q-factor can be represented as: $1/Q_u = \sum R_s/G + 1/tan\delta$, where R_s and G are the surface resistance and the geometrical factor of the conducting resonator element. Losses in the dielectric are $Q_{diel} \sim 1.24 \cdot 10^4$ which is much higher then in the losses in the covering $Q_s \sim 1.3 \cdot 10^3$. The geometrical factor of the sample with dimensions 5×5mm is 78 Ω, the geometrical factors of the bases are $G_{b1} = 20 \cdot 10^3$ Ω, $G_{b2} = 85$ Ω. The measured low Q-factor is caused by the larger ohmic dissipation on the conductor surfaces of the RDR with respect to the calculated values.

To increase the Q-factor, air gaps, gaps between the dielectric and the metal covering can be introduced [53, 54]. A simulation study was performed using finite element method to determine the effect of the gaps on the resonator parameters.

2.8.3 Effect of the gaps

Air gaps or spacers in the DR structure give the way for the improvement of the device performance (separation of the resonant frequencies and slight increasing of the Q-factor) although they make the resonator parameters determination more difficult. Few DR models take into account the presence of the gaps [53, 54, 88, 89]. In the work of Y. Kobayashi [53, 54] it was shown that gaps in the cylindrical DR increase the resonator Q-factor and decrease the resonant frequency of the TE_{011} mode.

Study of the gap effect on the RDR parameters is a difficult problem due to the absence of theoretical estimates and analytical relations, so that the full electromagnetic analysis using the electromagnetic simulators had to be performed.

Two different types of gap are considered: type-A, in which the metal surfaces normal to the gap are continuous (Fig. 2.22a), and type-B, in which the metal surfaces are discontinuous (Fig. 2.22b). In Fig. 2.22c a sketch of the RDR with the general type gaps between dielectric and metal covering is shown. Gaps of type-B are more easily done in practice, since type-A requires a good ohmic contact of the whole conductor enclosure. Various combinations (Fig. 2.22a,b,c) have been studied: type-A and type-B, along X or Z directions, symmetrical or asymmetrical gaps. The type, size and orientation of the gaps have different impacts on the resonant modes Q-factors, resonant frequencies and straight current regions.

In particular, it can be seen that type-A along the z-direction allows to further separate resonant frequencies of the the fundamental modes. An air gap between dielectric and sample has a different effect on the resonant frequencies of the TE_{101} and TE_{011} mode as shown in Fig. 2.23. This feature is due to the difference between stored magnetic and electric energies on the side where the gap was introduced, and it can be described using perturbation technique.

In [90] estimates of the resonant frequency shift with changes in the volume of the resonator with electric boundaries is performed. It is shown that the resonant frequency shift depends on the ratio between stored electric and magnetic energies in the region which is changed by the gap. The resonant frequency shift can be defined by equation:

$$s - j\omega_0 = \frac{j\omega_0}{W_T} \int_{V_D} \left(\frac{1}{4}\mu_A |\overrightarrow{H_A}|^2 - \frac{1}{4}\varepsilon_A |\overrightarrow{E_A}|^2 \right) \tag{2.8.3}$$

or

$$\frac{\Delta\omega}{\omega_0} = \frac{W_M - W_E}{W_T} \text{ at } \Delta V_D \leq 0 \tag{2.8.4}$$

where V_D is the volume of the dielectric and W_T is the total stored energy;
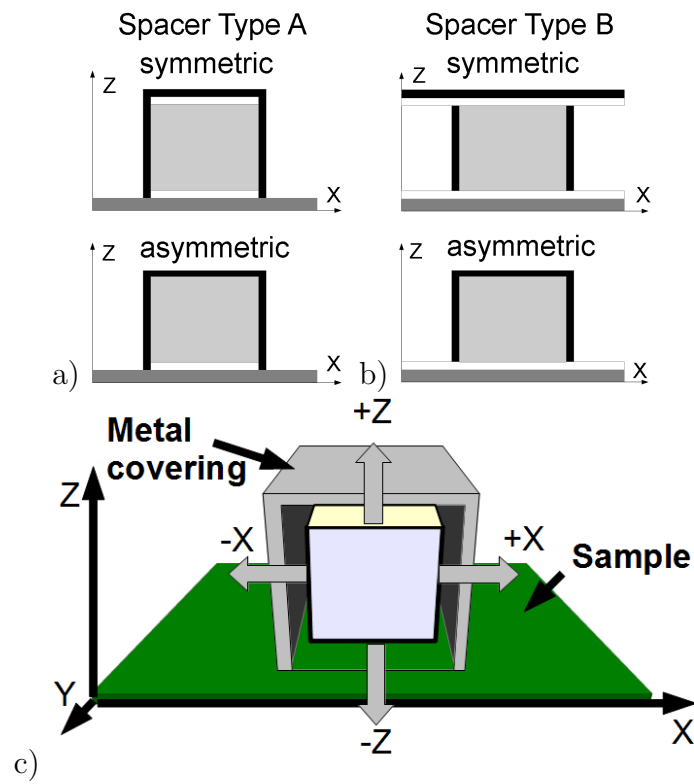
Figure 2.22: Draft of the rectangular DR gapped model used for the simulation: A-type gap (a), B-type gap (b) and general case (c).

So, if volume increasing occurs in a place where the stored unperturbed electric energy is higher than magnetic energy, the resonant frequency decreases and vice versa. This allows us to determine a behaviour of the resonant frequency in presence of the gaps in the resonator in a situation when metal covering is in electrical contact with the sample.

In RDR configuration where TE_{011} mode was excited, in the sample surface region, the stored electric energy is higher then magnetic energy. "Rotated" with respect to the TE_{011} mode by 90° ,TE_{101} mode has stored electric energy lower then stored magnetic energy in the surfaces of the metallic covering which are perpendicular to the sample surface $(y - z)$. Thereby by increasing the gap between the sample and dielectric the resonant frequency increases (Fig. 2.23a). Fig. 2.23a shows that a symmetric type-A gap along the x-direction, also, leads to the opposite behaviour of the fundamental modes with increasing of the gap thickness. It has to be noted that if the resonant frequency of RDR with type A gap decreases, it decreases linearly.

A different behaviour was also observed in the Q-factor of the low-order modes gap size dependencies. Fig. 2.23b shows that a decreased resonant frequency corresponds to a weak increase of the Q-factor of TE_{011} (from 1200 to 1280 for rutile RDR with gaps 0 mm and 0.4 mm).

Simultaneous increasing of the air gap in the directions of the crossection (-z, +z,-x, +x) brings to the nonlinear dependencies of the considered modes. Here the balance between dimensional effects and modes configuration plays a role.

In Fig. 2.24a, b the resonant frequencies and Q-factor of the TE_{011} mode are shown as a function of the air gap thickness. In this case the asymmetric type B gap was introduced using a teflon spacer between the sample and covered RDR. As far as Q-factor variation is concerned, type B gap is best suited, providing an increasing up to 50%. As an example, Q-factors of the TE_{011} mode changed from 1500 (300) up to 2100 (530), for simulations (experimental measurements), by increasing z-oriented symmetrical gap from 0 mm to 0.4 mm. With further gap size increase, a transformation of the TE_{011} mode into the TE_{111} mode was observed. This change in the mode configuration originates a deviation of the current on the sample surface from the desired straight path.

Application of the RDR with spacers is limited by the area of the linear current on the sample surface. Fig. 2.25 shows that asymmetrical type-A gaps along the z-axis determine a much smaller reduction of the straight-current region, here normalized to the x-y dielectric section area, with respect to the practically more feasible type-B gap.

The behaviour of the resonant frequency with increasing gap size was stud-
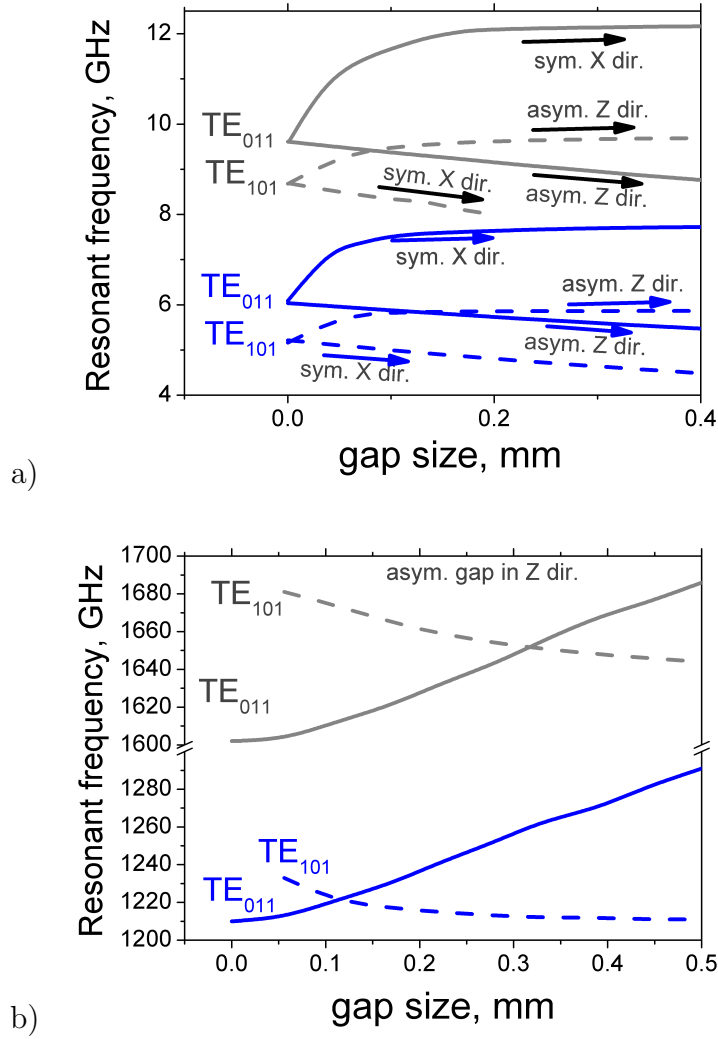
Figure 2.23: Resonant frequency (for asymmetric gap in Z and symmetric gap in X directions) (a) and Q-factor (for asymmetric gap in Z direction) (b) dependencies as a function of the asymmetric A-type gap size of the rutile and $LaAl_2O_3$ RDR with type A gap.
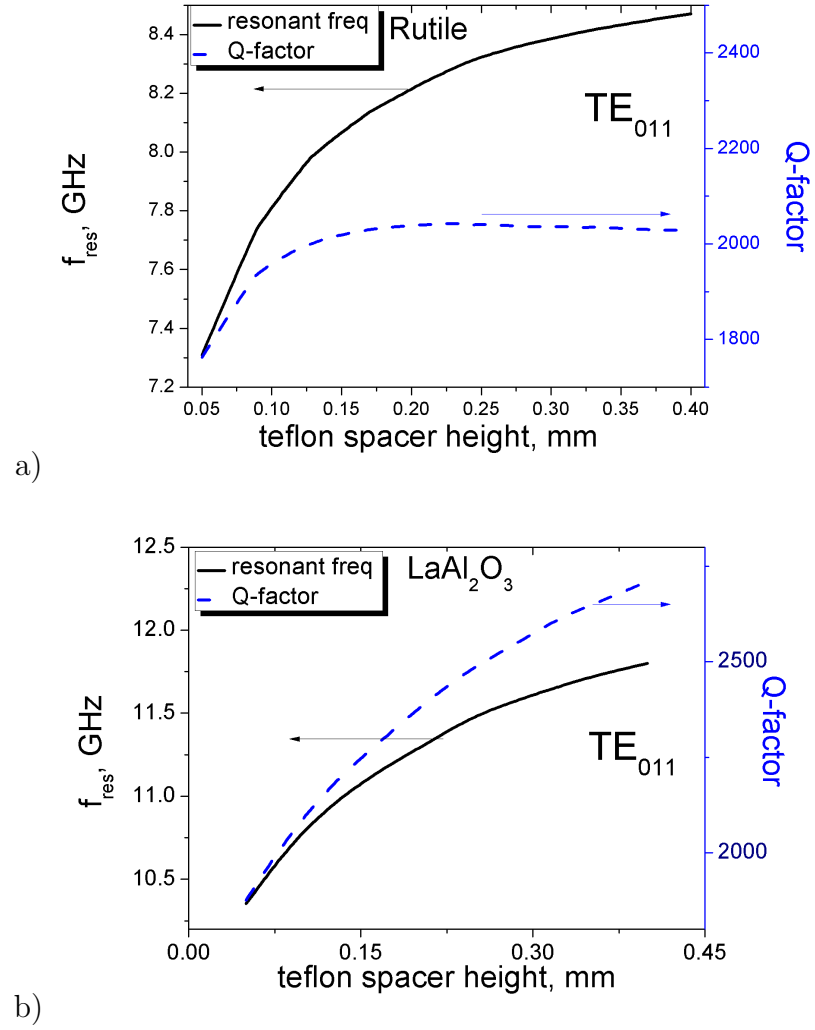
Figure 2.24: TE_{011} mode resonant frequency and Q-factor dependencies as a function of the asymmetric B-type gap size of the rutile (a) and $LaAl_2O_3$ (b) RDR.
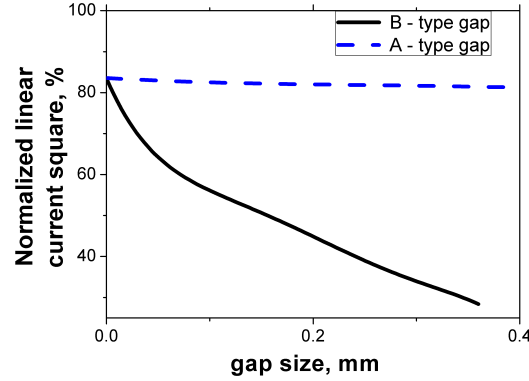
Figure 2.25: Normalized area of the linear current.

ied experimentally. Fig. 2.26 reports a comparison of simulation and experimental results concerning the impact of different types of gaps on the resonant mode frequencies. Experimental tests were performed at room temperature with Teflon spacers of various thicknesses. A good match between simulated and measured values can be observed.

Low temperature measurements (T=295 K-70 K) was also performed using type A RDR with the teflon spacer 0.4 mm and copper sample below the dielectric. It was shown that simulated temperature dependence of the resonant frequencies agree with the experimental data, but Q-factor is lower than estimated. At T=70 K the measured resonant frequency of the TE_{011} is 7.58 GHz which is 1% lower than calculated, Q-factor is 850 (half of calculated). In Fig. 2.27 comparison of experimental data and simulated resonant frequency of RDR in which copper metallic covering is used.

The possibility to generate straight microwave currents was demonstrated, and a loaded rectangular DR was designed. The mode determination was performed by comparison of the experimental and simulated data. Modeling of the gap presence in the "covered" rectangular DR was performed. It was shown that gap size increases the Q-factor and also the resonant frequency of the TE_{011} mode.

2.9   Conclusions

The methods of Z_s measurements have been reviewed. More precise methods use H-C type resonators. High quality of H-C DR is contrasted by the possibility of the measurements at a single frequency (possibility of the frequency
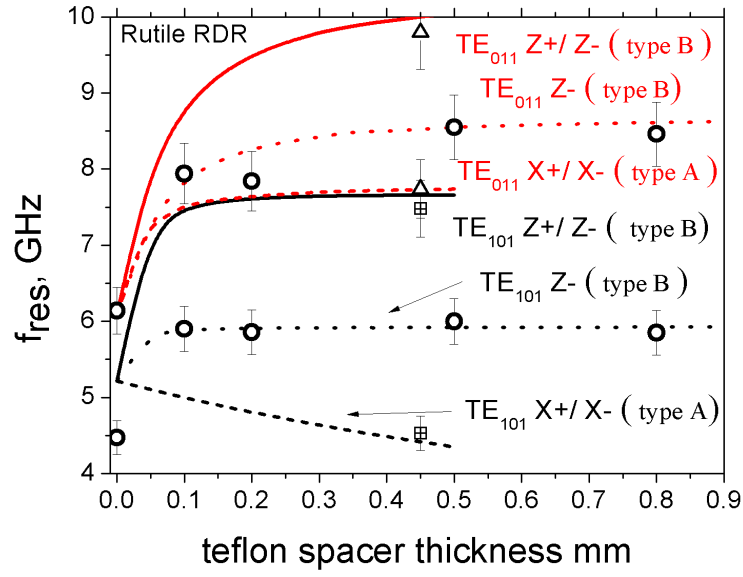
Figure 2.26: TE$_{011}$ (red line) and TE$_{101}$ (black line) modes resonant frequencies as a function of the gap size. Experimental and calculated data for the rutile RDR.
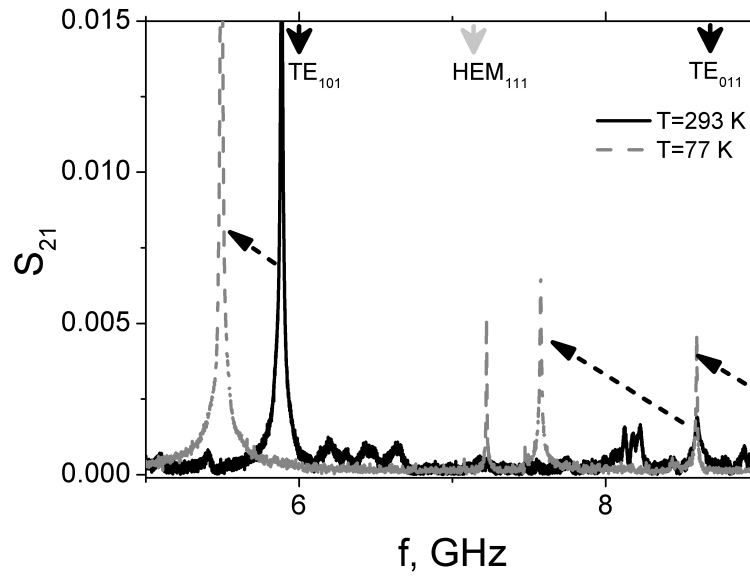
Figure 2.27: Measured transmitted power with respect to the simulated mode resonant frequencies of rutile RDR with copper covering. Its evolution with cooling up to T=77 K.

tuning leads to the more complex structure). To compensate this drawback, a wideband CD technique was used to obtain estimates of the frequency dependence of Z_s. One of the main problems in Z_s measurements in new superconductor structures is the small sample size. This leads to the decreasing of the resonator dimensions, so that sample can replace one of the bases, and needs correct choose of coupling mechanisms with possibility of its precise tuning. Three methods based on the DR technique were used: two H-C type resonators and a resonator in form of parallelepiped were designed and put into operation. This DRs and measurement technique were designed taking into account the small size of the samples under study, the available cryogenic equipment, and the need for the operation in presence of high external magnetic field. All designed measuring cells were tested at low temperatures.

As a future development, the creation of the measuring cell which allows to perform the measurements at tilted magnetic is planned. For this purpose the axial dimensions of the measuring cell has to be reduced to fit it in the cryostat between poles of the magnet. This measuring cell has to be used with various dielectrics including RDR structure.

Chapter 3

Ferromagnetism and superconductivity

At the present time the study of the superconductor/ferromagnetic (S/F) structures is an active field [91],[92]. Many interesting phenomena are observed. Large attention is devoted to the investigation of S/F multilayered structures both as a mean to unveil the fundamentals of superconductivity and for potential technological applications, such as spin switches and -junctions [93]. One of the most known properties is the oscillation of the order parameter in the depth of the ferromagnetic layer thickness [92], as opposed to the exponential decay, occurring in normal non-magnetic conductors. The behavior of F/S multilayers is strongly affected by the magnetism of the ferromagnetic material: hard ferromagnets depress the superconducting ordering and oscillations of the order parameter becomes undetectable. Similarly, a new interest in the vortex physics in S/F structures has arisen [94].

In this chapter the results of the multilayer S/F structures are presented. A study of the microwave surface impedance was performed to access the intrinsic properties of the complex structure.

3.1   Effects in S/F structures

Proximity effect

In the structures where a superconductor is placed in contact with a normal metal, the modification of both materials properties can be observed. In this situation, the Copper pairs penetrate in the normal metal at a characteristic distance which is proportional to the thermal diffusion length ($\sim \sqrt{1/T}$). This leads to the induction of superconducting properties in a normal conductor

and to a monotonous decay of the order parameter in the normal layer. This phenomenon is called proximity effect . Simultaneously, the leakage of Cooper pairs leads to a decrease of T_c of the superconducting system (so-called inverse proximity effect) [92, 95] (See 3.1a).

On superconductor-normal conductor boundary, the proximity effect determines a Josephson current through the normal conductor layer due to Andreev reflection [96, 97]. At superconductor/normal conductor boundary the transformation of the normal charge onto the Cooper pairs takes place, where normal electrons with energy below the superconducting energy gap are reflected from the boundary as holes. Correspondingly, a doubled charge is transferred into the S side as Cooper pairs.

In a S/F system, the presence of the spin energy bands in the ferromagnetic layer induces damped oscillatory decay of the S order parameter in it. The superconducting electrons in the ferromagnetic layer allow to study the effect of large exchange field on it also by the simple changing of the layered structures thickness. This effect is related to the splitting of the electron's level under the effect of the exchange magnetic field acting on the spins of the cooper pair electrons. In the ferromagnet layer one electron with spin along exchange field (it is proportional to the $\propto E_{ex}$, where E_{ex} is an exchange energy) decreases its energy by the value of E_{ex}, whereas the electron with opposite spin increases its energy correspondingly. Here I use the exchange field represented as E_{ex} in Kelvin degrees. To compensate this energy variations electrons change its kinetic energy, which leads to the appearance of the center of mass momentum $q=2E_{ex}/v_f$, where v_F is the Fermi velocity. This results in the modulation of the order parameter in the direction perpendicular to the S/F interface on the characteristic length scale of the superconducting correlation decay in the F layer ξ_F [98]. In the ferromagnet the electron's spin orientation along the exchange field is preferable, thus E_{ex} affects as a pair breaking parameter and reduces the value ξ_F.

By solving the generalized Ginzburg-Landau equations, one can show that the decay of the order parameter in the ferromagnetic layer is described as: $\psi(x) = \psi_0 \exp(-x/\xi_F)\cos(x/\xi_F)$, where the characteristic lengths is represented as $\xi_F = \sqrt{D_F/E_{ex}}$. In contrast, for S/N structure the decay of the S order parameter in the F layer is monotonous: $\psi(x) = \psi_0 \exp(-x/\xi)$ (See Fig. 3.1). Due to the damped oscillations of the order parameter the density of states also oscillates in space (this effect is widely studied [99, 100, 101]).

Theoretical description of these effects of the parameters oscillation in S/F multilayered structure can be described by Eilenberger [102, 103] or Usadel [104, 105] equations which are out of thesis topic.

The oscillating order parameter produces interesting effects, which depend
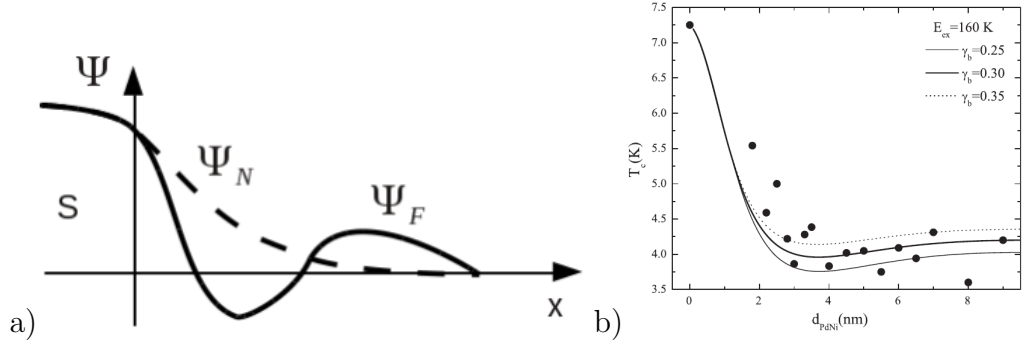
Figure 3.1: Schematic behaviour of the superconducting order parameter near S/N and S/F interfaces (a). Example of the critical temperature of the superconductor depending from the ferromagnetic layer thickness (b). Solid lines represent the fitting of the experimental data.

on the relation between the ferromagnetic layer thickness (d_F) and ξ_F. In the S/F multilayers when $d_F < \xi_F$, the change of the order parameter is small. In this case, there is no phase difference between the S layers. By increasing of F layer thickness up to the critical value $d_F^c \sim \xi_F$ the pair wave function crosses the zero in the middle of the F layer, yielding a difference of π between the wave function phases of the S layers [106]. Further increase of the F layer thickness leads to the periodical transitions between so-called 0 and π phases. An amplitude of these oscillations depends from the ferromagnetic material. For the weak F, the effect of the order parameter oscillations is more visible than in strong ones, where a strong pairbraking dominates.

Oscillation of the critical temperature in bilayers as a function of d_F has been widely observed in experiments [107, 108]. The experimentally observed temperature dependence of the critical temperature is explained by the so-called single(multi)-mode approximation, developed by Fominov [109]. In Fig. 3.1b the example of this fitting of the experimental data with the theoretical model is shown for bilayer samples $Nb/Pd_{0.84}Ni_{0.16}$ [110]. Increase of the ferromagnetic layer leads to a decrease of the critical temperature. Amplitude of the oscillation depends on the transparency of the S/F boundary, which define the diffusion of the Cooper pairs between the layers. For a fully transparent interface the oscillations are more pronounced. The increase of the transparency leads to a decreasing of the amplitude of the $T_c(d_F)$ oscillations and to the critical thickness d_F^c.

3.2   Samples characterization

3.2.1   Superconductor/ferromagnetic samples under study

Two kind of samples were studied. The first kind consists of pure Nb films with different thickness, 20 nm and 30 nm. They were grown and characterized for comparison. Second kind of samples consist of $Nb/Pd_{0.84}Ni_{0.16}/Nb$ super-conductor/ ferromagnetic/ superconductor (S/F/S) multilayers. The samples were grown at University of Salerno within a PRIN 2007 project. They were grown in the same conditions at room temperature by ultra-high vacuum dc diode magnetron sputtering. Samples differ in the $Pd_{0.84}Ni_{0.16}$ layer thickness (d_F= 1,2,8,9 nm) and have constant superconducting Nb layer thickness d_S= 15 nm. The coherence length of Nb is approximately ξ_S=6 nm [111]. So, one can approximately apply the models of S/F multilayers for $\xi_S \ll d_S$.

Nb was chosen as well known material with relatively high T_c=9.2 K (in bulk samples). The weak ferromagnet PdNi was chosen because its low exchange energy determines order parameter oscillations with comparatively large amplitude. It is known, that it is impossible to observe in practice more than two oscillation periods due to the pair-breking effect [110, 112]. Therefore the ferromagnetic thickness of the samples under study was chosen lower than 10 nm, which is of the order of ξ_F=3.3 nm (estimated for ferromagnet alloy $Pd_{0.84}Ni_{0.16}$ [111]).

S/F/S multilayers were deposited by dc sputtering on sapphire (Al_2O_3) substrate (5 x 5 mm and with the thickness 0.5 mm), which is more suitable for microwave measurements because of small dielectric losses and relatively low dielectric constant. Sputtering was performed by a multi-target Ultra High Vacuum system with a load-lock chamber. The main chamber sputtering pressure was 10^{-10}mbar, the sputtering Argon pressure was $4 \cdot 10^{-3}$ mbar and load-lock chamber pressure was 10^{-8}mbar. The load-lock chamber allows to perform simultaneous deposition on six substrates with the same deposit rate for all samples. The deposition rates were 0.28 nm s^{-1} and 0.4 nm s^{-1} for the Nb and $Pd_{0.84}Ni_{0.16}$ respectively was controlled by a quartz crystal monitor calibrated by low-angle x-ray reflectivity measurements of the film samples of each material. The samples with various ferromagnetic layer thickness were deposited in the same run to ensure the similarity of the deposited samples properties. Ni concentration was controlled by Rutherford-backscattering [113].

The magnetic properties of the PdNi alloy were studied using SQUID magnetometer (see ref. [114]) at the temperature T=10 K with a magnetic field applied parallel to the sample surface. In Fig. 3.2a and b the hysteresis loop and the temperature dependence of the magnetization of the F sample, 19.2-nm
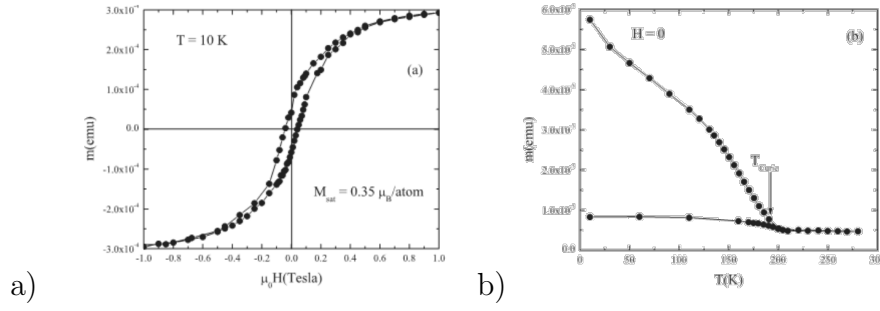
Figure 3.2: Magnetization loop for a 50 nm thick $Pd_{0.81}Ni_{0.16}$ film at T = 10 K (a) and temperature dependence of the magnetic moment (b)

thick, are reported [115]. At the temperature T=10 K the saturation magnetization is M_{sat}=0.35 μ_B/atom. The sample thickness varied from 3.3 to 70 nm M_{sat} varied from 0.27 μ_B/ atom to 0.35 μ_B/atom. The Curie temperature was determined by the temperature variation of magnetization. It corresponds to the temperature where the irreversibility appears. For $Pd_{0.81}Ni_{0.16}$ samples it is equal to 200 K. This value is independent from the sample thickness, at least in the interval from 3 nm up to 70 nm, and it agrees with the bulk sample case.

3.2.2 TEM

Since all trilayers under study were grown in similar conditions, only one of them (the one with d_F=4 nm) was studied in terms of its crystal structure through transmission electron microscope (TEM) measurements. In Fig 3.3a TEM (bright field) pictures of the sample cross-section are shown. It can be observed that the crystal structure of Nb layer is similar to the structure of the bulk one. Inter-atomic distance between the Nb atoms is 2.9 $\mathring{A}$.

PdNi layer crystalline structure was studied by TEM measurements in the diffraction regime (dark field). In Fig3.3b light and dark regions represent PdNi and Nb layers respectively. From these images a roughness of the PdNi layer can be detected. Heavy Pd atoms are diffused into S layer. This diffusion process leads to some specific effects that can be observed in the microwave measurements.

3.2.3 EXAFS analysis

Nb-K edge ($E_{Nb} = 18.986$ keV) x-ray absorption spectra (XAS) were collected at the GILDA-BM08 beamline at the European Synchrotron Radiation Facility (ESRF Grenoble, France) in fluorescence geometry. The x-ray absorption
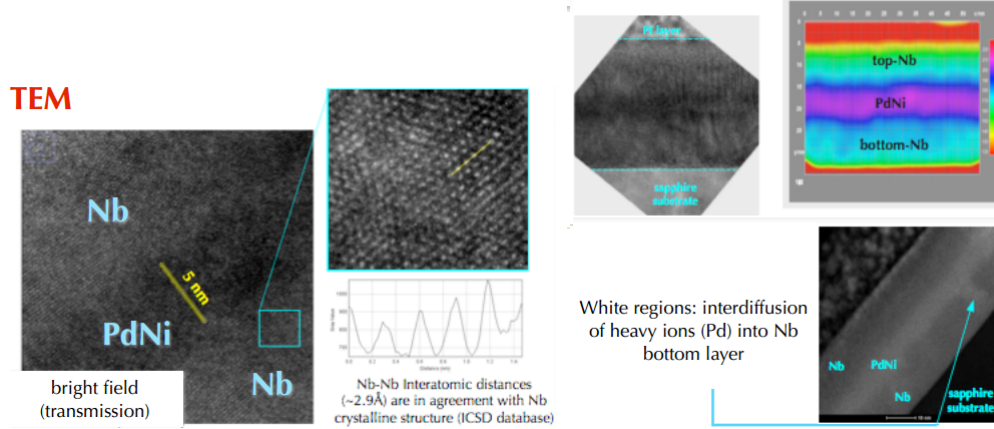
Figure 3.3: TEM pictures of the Nb/Pd$_{0.84}$Ni$_{0.16}$ sample with d$_F$=6nm

spectra were collected in fluorescence geometry keeping the samples at 77 K to reduce the structural disorder induced by thermal vibrations. The sample surfaces were oriented about 45° from the polarization direction of the incoming x-ray beam in order to reduce the polarization effects in the spectra.

Nb k$_\alpha$ fluorescence intensity (E$_{k_\alpha}$ ≈16.6 keV) was measured using a 13-element ultrapure Ge multidetector. Bragg reflections were identified by comparing the spectra collected with the different elements (I$_i$) and removed by interpolating the data under the peaks; the total fluorescence signal is calculated as I$_f = \sum_i I_i$. The incident intensity I$_0$ was measured using an Ar filled ionization chamber to calculate α(E)=I$_f$/I$_0$, proportional to the Nb linear absorption coefficient μ(E) (the thin Nb films ensure negligible self-absorption effects). Up to 8 spectra were measured for each sample and averaged up to improve the data statistics. Quantitative XAFS data analysis has been performed by least square data refinement procedure in the reciprocal space, by fitting the raw k-weighted spectra to the theoretical XAFS formula [116].

Nb has body centered cubic (bcc) crystallographic structure, depicted in Fig. 1, with lattice parameter (cube edge) a = 3.30 Å. The five coordination shells shown in Fig. 3.4a were used to refine the Nb K edge XAFS data. In the analysis the multiple scattering contributions have been considered. The multiple shell data refinement has demonstrated to improve the XAFS data analysis reliability [117, 118], as it allows to apply severe constraints among the structural parameters. An example of best fit, showing the partial contributions and the residual, is reported in Fig. 3.4b. The best fit parameters provided quantitative details about the Nb local structure. Firstly, we notice that the geometrical constraints based on bcc structure provide a satisfactory best fit in Nb with $d_N b$=30 nm as well as in Nb(15)/PdNi(x)/Nb(15) trilayers,
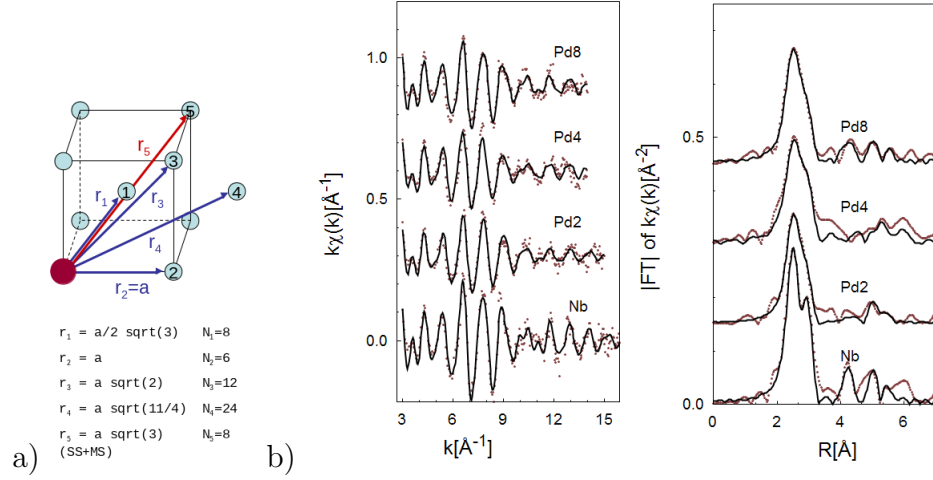
Figure 3.4: (a) Local geometry in bcc structure: the five coordination shells used in the analysis are highlighted. The bcc geometry constrains the scattering path lengths r_i and multiplicity numbers N_i of the coordination shells used for XAFS data refinement. (b) Experimental Nb K edge XAFS data (points) and best fit (full line) for all the investigated samples (vertically shifted for the sake of clarity)

thus confirming the validity of the model. The lattice parameter corresponds to what expected in bulk Nb. Therefore, the Nb local structure is close to the bulk Nb structure in all samples, and only weakly affected by the magnetic PdNi layer. Nevertheless, the structural disorder is larger in trilayers (about 40 % higher) than in pure Nb. The growth of the interlayer has then some effect on disordering the Nb atomic structure at the local scale. Interestingly, this effect is nearly independent from the interlayer thickness: the sample with d_F=8 nm exhibits comparable, or even smaller, disorder with respect to the one with d_F=2 nm.

The crystal structure was also studied after around one year after previous measurements. Ni K-edge ($E_{k_\alpha} \approx 8.33$ keV) XAS were measured in fluorescence geometry at the ELETTRA XAFS beamline. A Ketek silicon drift detector was used to collect the Si Ka fluorescence signal. More than 5 spectra were measured for each sample, Bragg peaks were removed and the spectra averaged up in order to have high quality data suitable for the analysis. Fit of the experimental Ni K edge XAFS data is shown in Fig. 3.5a. The samples with thinner PdNi layer (d_F=2, 4 nm) are characterized by weaker signal, which is an indication of bigger disorder in the structure. They, also, have a larger noise with respect to the samples with thick F layer, caused by low amount of Ni. The inter-atomic distance a=2.66$\mathring{A}$, which was found by fitting procedure,
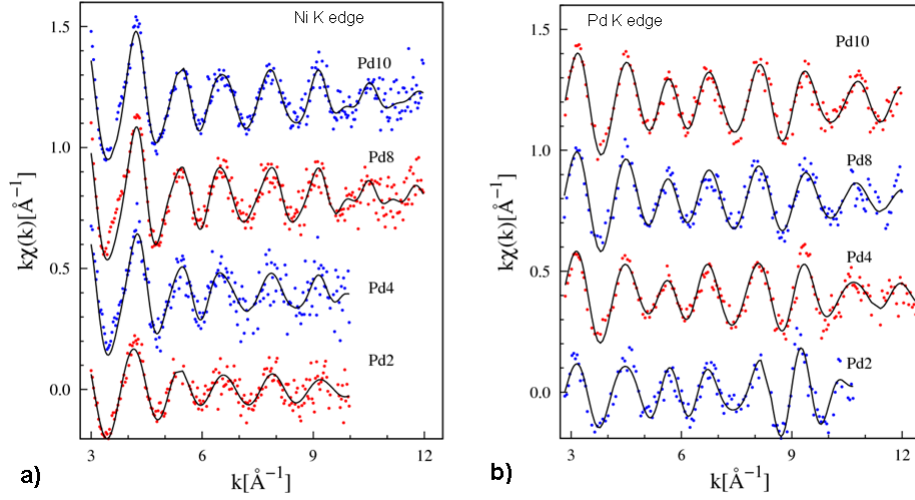
Figure 3.5: Experimental Ni (a) and Pd (b) K edge XAFS data (points) and best fit (full line) for all the investigated samples

corresponds to the structure of PdNi with bigger concentration of Ni (50% with respect to the nominal 16%). This fact suggests that part of the Pd atoms is unbounded from PdNi, which partially agree with the results of TEM study. It was, also, determined that in the sample with d_F=2 nm part of Ni atoms forms an additional phase with Nb. Based on the comparison with the structures presented in the literature it was shown, that $NiNb_5$ phase, which is characterized by the lattice parameter a=2.94$\mathring{A}$ and consists around 15% of Ni atoms, is formed in the sample with thinnest F layer.

The study of the Pd K-edge ($E_{k_\alpha} \approx$18.98 keV) confirms the presence of cubic crystal structure PdNi phase with a=2.66$\mathring{A}$. It indicates that part of the Pd atoms (around 35%) is unbounded with PdNi alloy and can form the compound with Nb. Taking into account an contribution of PdNb into the XAFS signal, the presence of the Nb_3Pd phase with lattice parameter a=2.81$\mathring{A}$ was detected.

The XAFS study of Nb/PdNi/Nb samples shows that due to the aging effect, not only PdNi phase appears but also part of Ni and Pd atoms forms stable phase with Nb and multiphase structure is formed.
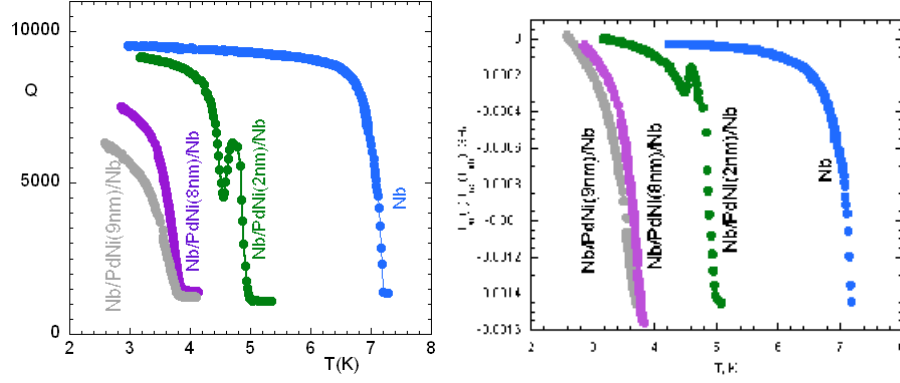
Figure 3.6: (a) Unloaded Q-factor and (b) the temperature dependence of the resonant frequency Nb/PdNi/Nb samples with d_F= 0,2,8,9 nm

3.3 Surface impedance measurements at zero magnetic field

Pure Nb film sample with thickness 30 nm and $Nb/Pd_{0.84}Ni_{0.16}/Nb$ samples with ferromagnetic layer thickness 2, 8 and 9 nm were studied at zero magnetic field through a 8-GHz DR, excited on the main TE_{011} mode and operated in transmission. Measurements were performed in the linear regime, as directly checked by varying the incident power over a factor of 10 without observing any variation in the response. Due to the small sample dimensions (5 x 5 mm), the configuration of the DR with the Teflon spacer and Al mask was chosen to exclude the effect of the sample border (see sec. 2.6). The measured temperature dependencies of the unloaded Q-factor and resonant frequency are reported in Fig. 3.6.

As it was shown in the technical chapter, the complex resistivity of the sample can be extracted from the raw data, obtained with DR, through the following relation;

$$\rho_s(T) = \rho_1(T) - i\rho_2(T) = Gd \left[\left(\frac{1}{Q(T)} - \frac{1}{Q(0)} \right) - 2i \left(\frac{f_0(T) - f_0(0)}{f_0(0)} \right) \right]$$
(3.3.1)

where G is the geometrical factor of the sample.

The temperature dependence of the real part of the resistance, which represents the losses, is shown in Fig. 3.7.

Looking at the raw data of the trilayer sample with d_F=2 nm, a peak is observed in the temperature dependencies of Q(T) and Δf_{res} near T=4.75 K

($T=0.88$ T_c, with $T_c=5.1$ K). The peak in the raw data excludes the possible error in data elaboration. It cannot originate from a double transition, usually caused by sample inhomogeneities, because it would give a step feature instead, contrary to the observed peak.

    The dependence of the resistivity (see Fig. 3.7a) with respect to the normalized temperature indicates that the increase of the PdNi layer thickness broadens the transition: for samples with $d_F=$ 2, 8 and 9 nm the corresponding transition Δ T_c=T(0.9 R_n)-T(0.1 R_n) is Δ T_c/T_c=0.11, 0.07 and 0.11 respectively.

    From the imaginary part of the resistivity the effective penetration depth (λ_{eff}) of the superconductor can be calculated. Then, from these data the London penetration depth (λ_L) and hence the superfluid density $n_S = [\lambda_L(T)/\lambda_L(0)]^2$ can be determined. Due to the peculiarity of dielectric resonator technique only the variations of ρ_2 instead of its absolute value can be determined. Therefore only variation (with respect to the reference value) of the effective penetration depth can be obtained:

$$\Delta\lambda_{eff}(T) = \lambda_{eff}(T) - \lambda_{eff}(T_{ref}) = \frac{2Gd}{\omega\mu_0}\left(\frac{f_0(T) - f_0(T_{ref})}{f_0(T_{ref})}\right) \qquad (3.3.2)$$

The effective penetration depth can be described in terms of the London penetration depth of superconducting thin films with the thickness d as follows [33]:

$$\lambda_{eff}(T) = \lambda_L(T)\coth\frac{d}{\lambda_L(T)} \qquad (3.3.3)$$

for the pure Nb thickness $d = d_{Nb}$, whereas in the trilayered samples $d = 2d_{Nb} + d_{PdNi}$.

    The penetration depth λ_{eff} at absolute zero can be determined only by some fitting procedure. From BCS theory it is known that there is no universal temperature dependence because of variation of the $\xi_0/\lambda(T)$ ratio, therefore numerical calculations are required. In the dirty local limit (which can be applied to our samples) in pure superconductors ($\xi_0 < \lambda(T)$) [10]:

$$\left(\frac{\lambda_{eff}(T)}{\lambda_{eff}(T_{ref})}\right)^{-2} = \left(\frac{\Delta(T)}{\Delta(0)}\right)\tanh\left(\frac{\Delta(T)}{2k_BT}\right) \qquad (3.3.4)$$

where $\lambda(0)$ becomes a parameter in the fits of the experimental data.

    Normalized energy gap is approximated numerically as [112]:

$$\left(\frac{\Delta(T)}{\Delta(0)}\right) \approx \left[\cos\left(\frac{\pi T^2}{2T_c^2}\right)\right]^{1/2} \qquad (3.3.5)$$

a)

b)
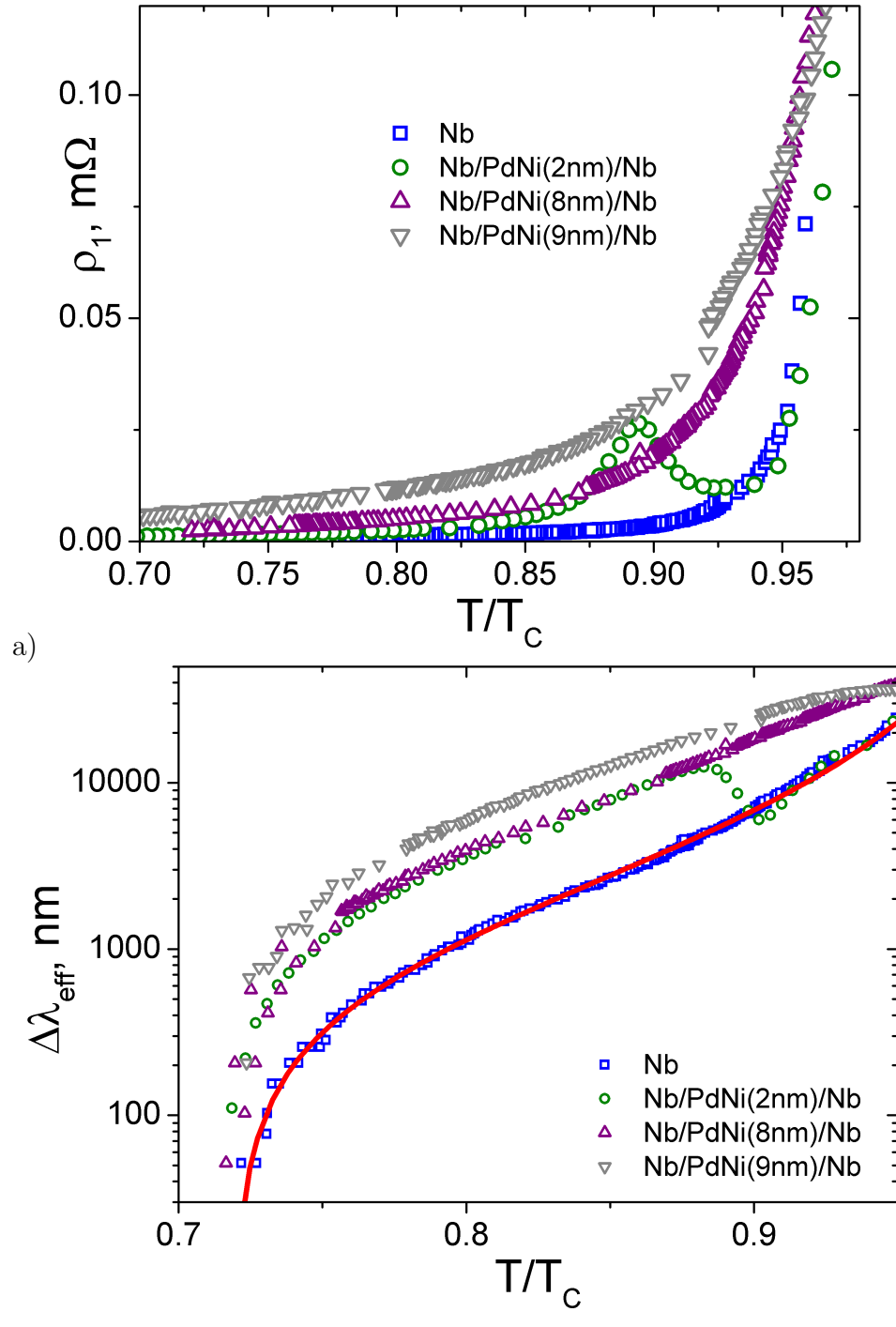
Figure 3.7: (a) Temperature dependence of microwave real resistivity and (b) penetration depth Nb/PdNi/Nb samples with $d_F = 0,2,8,9$ nm (solid line in panel (b) represents the BCS fit)
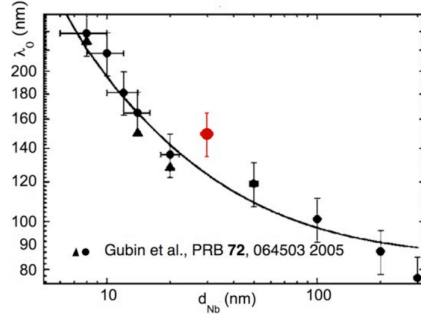
Figure 3.8: Comparison of the measured value of $\lambda_{eff}(0)$ for film Nb sample with data from the literature based on the dependence from d_S

The estimate of $\lambda_L(0)$ for the pure Nb is possible by applying the fitting procedure, which is based on the classical theories (like BCS). By fitting $\lambda_{eff}(T)$ for 30-nm Nb sample (Fig 3.7) using BCS expression 3.3.4 one obtains $\lambda_L(0) =150$nm. This value corresponds to the $\lambda_L(0)$ film thickness dependence obtained in [119]. In Fig.3.8 the comparison of this results is shown.

For the thinnest F layer, the effect is only in the decrease of the critical temperature. The superconducting properties are leaved untouched. In this case the sample with $d_F=1$nm behaves like a pure Nb one. With the increase of the ferromagnetic layer the critical temperature oscillates as we can see from Fig. 3.8.

On the other hand, measurements of the trilayer $Nb/Pd_{0.84}Ni_{0.16}$ samples shows that BCS approximation for $\lambda_{eff}(T)$ does not yield satisfactory fits of the data. In the literature there is no theoretical background which can precisely describe the temperature dependence $\lambda_{eff}(T)$. But it is possible to obtain rough estimates by using two-fluid model relation:

$$\left(\frac{\lambda_{eff}(T)}{\lambda_{eff}(0)}\right)^{-2} = \left(1 - \frac{T}{T_c}\right) \tag{3.3.6}$$

It is found, that with the increase of d_F from 2 to 9 nm $\lambda_{eff}(0)$ increases from 300 nm up to 435 nm.

3.3.1   Discussion

I now comment on the peak, observed on the temperature dependence of the losses and of λ_{eff} in the Nb/PdNi/Nb sample with $d_F=2$ nm (see Fig. 3.7). It can be argued that the PdNi layer drives a crossover away from the BCS behaviour. Observing Fig. 3.7b it can be seen that the sample with 2-nm F
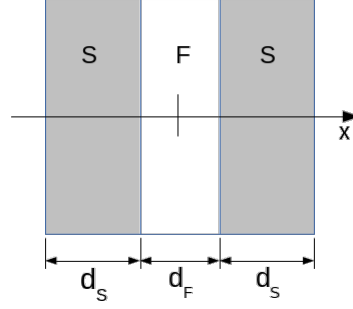
Figure 3.9: S/F multilayer structure. The x axis is choosen perpendicular to the planes if the S and F layers.

layer behaves like the trilayers with larger F layer thickness for T≪T$_c$ indicating that the Nb layers are decoupled. On the other hand, near T$_c$ the BCS behaviour is recovered and the two Nb layers are coupled and behave as the pure Nb sample.

To obtain the theoretical description of the experimentally observed temperature dependencies for the trilayers with various d$_F$, models which describes the oscillations of the critical temperature with d$_F$ can be used.

For the general case of S/F multilayer structure, where d$_F$ and d$_S$ are the F and S layer thicknesses correspondingly (see Fig. 3.9), the 0 state corresponds to the same sign of the wave function in each S layer, otherwise for the π phase the sign if the wave function in the S layers differ from layer to later. The S/F multilayered structures can be described by the Eilenberger equation can be used. Within this model, the multilayer S/F structure can be described as an array of S/F bilayers [106]. Usually the electron elastic scattering time $\tau = l/\nu_f$ for S/F multilayers is small, and the Eilenberger equations can be rewritten in the dirty limit. In case of the weak ferromagnet (as PdNi alloy) and under the conditions T$_c\tau \ll 1$ and E$_{ex}\tau \ll 1$ the Eilenberg equations can be transformed in simpler linearised Usadel equations. As was shown experimentally and theoretically [93, 120] the state of the S/F/S coupling is determined by the thickness of the F layer. Increase of the thickness d$_F$ produces the crossover between the 0 and π states of the S layers coupling (see Fig. 3.9 from [93]). A thickness d$_F^c$ at which the crossover occurs is called critical thickness. This thickness is temperature dependent value.

The temperature, which corresponds to the crossover and corresponding F layer thickness, strongly depends on the parameters such as the exchange energy of the F, E$_{ex}$, and S/F boundary transparency (described by transparency parameter γ_B). These parameters can not be measured directly, but can be determined by present theories of the S/F multilayers, as an example, by the

fit of the experimental dependence of the critical temperature versus F layer thickness.

A comparison of the results measured for S/F/S samples with data in the literature can be obtained based on the F layer thickness dependence of the critical temperature. It was shown, that with the increase of the ferromagnetic layer the critical temperature of the Nb/PdNi/Nb samples decreases rapidly down to T_c=3.5 K for d_F=3 nm. This dependence can be described from the point of view of Fominov's theory [109], which is based on the linearised Usadel equations and was successfully applied for the case of bilayers Nb/PdNi. This model can be used only for the description of the multilayered S/F structures 0-state in the dirty limit. I skip here the full description of the model [109]. Fig. 3.10 represents the fit of the F layer thickness dependence of the transition temperature of Nb/Pd$_{0.84}$Ni$_{0.16}$/Nb samples. This model takes into account two parameters as independent: the exchange energy (E_{ex}) as pairbreaking parameter and γ_B, which depends from the S/F interface transparency: larger transparency corresponds to lower γ_B. The parameter γ_B=0 indicates fully transparent S/F boundary and it is associated to the bigger amplitude of the order parameter oscillations. Larger E_{ex} reduces the value of the critical temperature.

For the fit (see Fig. 3.10) I use Fominov's model in the so-called single mode (it takes into account only real roots in Usadel equation). It has to be noted that this approximation is valid for $d_F \sim \xi_F$, which is the case of the thickness of the samples under study, then the conditions $\sqrt{E_{ex}/\pi T_{c0}} \gg 1/\gamma_B$. A large number of microscopical parameters were used during the fitting procedure. Part of them, like resistance of PdNi and Nb, can be obtained experimentally for the case of the bulk samples. The Nb coherent (thermal diffusion) length is calculated based on expression: $\xi_S = \sqrt{D_S/2\pi T_{c0}}$, where T_{c0} is the temperature of superconducting transition of the pure Nb and D_S is the diffusion coefficient of superconductor. The diffusion coefficient is related to the characteristic length of pure Nb l_S=2.3 nm [121] and expressed in the form: $D_S = v_S l_S/3 = 1.9 \cdot 10^{-4} m^2/s$, where $v_S = 2.73 \cdot 10^7$ cm/s is the Fermi velocity. As opposite to models [106, 103], which take into account the coherent length determined within the dirty limit $\xi_F = \sqrt{D_F/E_{ex}}$, the model described here operates with thermal diffusion length: $\xi_F^* = \sqrt{D_F/2\pi T_{c0}}$. Here the diffusion coefficient $D_F = v_F l_F/3 = 2.3 \cdot 10^{-4} m^2/s$ (see ref. [110]), where $v_F = 2 \cdot 10^7$ cm/s and $l_F = 3.5$ nm are Fermi velocity and average of mean-free path correspondingly. Fit of the experimental data is sensitive to experimental parameter γ, which is a measure of the strength of the proximity effect between superconductor and ferromagnet: $\gamma = \frac{\rho_S \xi_S}{\rho_F \xi_F}$. It is determined by the relation between low temperature resistivities of F ($\rho_S = \rho_F = 50\mu\Omega cm$) and

S ($\rho_F = \rho_S = 24\mu\Omega cm$ [110]) materials and can be determined based on the dc measurements of thin single layer films. Applying this values the parameter $\gamma = 0.44$ was determined and was used as fixed parameter.

The parameter γ_B can be determined by the vertical position of the fitted $T_c(d_F)$ curve. The ferromagnet layer thickness d_F^*, at which the critical temperature is minimum can be determined. This value is connected to the coherent length in ferromagnet layer by the relation $d_{F,min} = 0.7\pi/2\xi_F$ [109]. Taking into account the diffusion coefficient D_F=2.3 $\cdot 10^{-4} m^2/s$ the exchange energy can be determined. In the Fig. 3.10 the fit made with different values of γ_B: 0.01, 0.1 and 0.2, corresponding to the different S/F interface transparency, was shown. The curve with $\gamma_B = 0.2$ fits the data. The fit was made taking into account the slope of $T_c(d_F)$ dependence. Best fit was obtained with $d_{F,min} = 2.9nm$ which corresponds to the ferromagnetic layer coherent length $\xi_F \sim 3.3$ nm. This value corresponds to the nominal coherent length for $Pd_{0.84}Ni_{0.16}$ $\xi_F \sim 3.14$ nm and $E_{ex} \sim 14$ mEv from ref. [110]. $d_{F,min}$ corresponds to the first minimum of $T_c(d_F)$ and can be used as approximated point for $0 - \pi$ transition.

Fominov's model is widely used for the fitting of the experimental data up to one period of the critical temperature oscillation. More general model developed by Buzdin [92] takes into account separately contribution of 0 and π phases, and possible temperature induced phase transition. Therefore, this model can be used for the qualitative description of $0 - \pi$ transition effect. In Fig. 3.10 the thickness dependencies of 0 and π phases are shown. It was determined that the temperature induced $0 - \pi$ crossover is possible only at F layer thicknesses $d_F < d_F^*$ near the crossing of the thickness dependencies of T_c^0 and T_c^π. Here $T_c^{0,\pi}$ is determined by the characteristic relation:

$$\ln(T_c^{0,\pi}/T_{c0}) = \Psi(1/2) - \Re[\Psi(1/2 + \Omega_{0,\pi}(T_c^{0,\pi}))] \qquad (3.3.7)$$

where Ψ is digamma function; Ω is depairing parameter responsible for the destruction of the cooper pairs in S layer due to the proximity effect.

The superconducting energy gap calculated within this model allows to determine the G-L energy. The crossover of the G-L energies at certain F layer thickness and temperature T_0 was shown. To minimize the total energy, the transition from $\pi-$phase to $0-$phase occurs. The temperature of the transition can be determined by [122]:

$$\frac{T_c^\pi - T_0}{T_c^0 - T_0} = \frac{a^\pi T_c^0}{a^0 T_c^\pi}\sqrt{\frac{b^0}{b^\pi}} \qquad (3.3.8)$$

where $a^{0,\pi} = 1 - \Re[\Omega_{0,\pi}\Psi^{(1)}(1/2 + \Omega_{0,\pi})]$ and
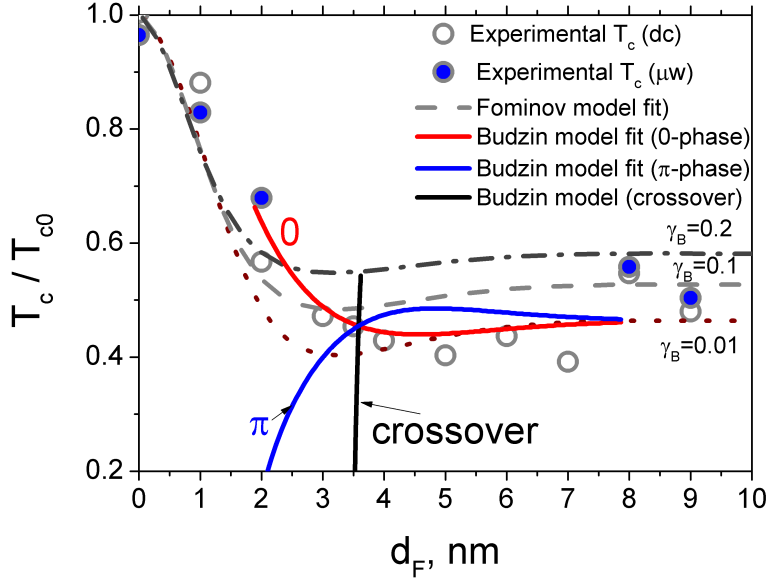
Figure 3.10: Oscillation of the critical temperature of Nb/PdNi/Nb samples with increasing of ferromagnetic layer thickness. Solid line shows the fit based on the Fominov's model. Dashed lines indicates the corresponding values of T_c for 0 and π phase based on the Budzin's model

$b^{0,\pi} = \frac{-1}{16(\pi T_c^{0,\pi})^2} \Re \left[\Psi^{(2)}(1/2 + \Omega_{0,\pi}) - \Omega_{0,\pi} \frac{i/2 \mp 4\gamma_1 q^2 e_f}{3 \mp 4e_f} \Psi^{(3)}(1/2 + \Omega_{0,\pi}) \right];$

$\Psi^{(n)}(z) = \frac{d^n \Psi(z)}{dz^n};$ q and ε_f are the F layer thickness dependent parameters.

It can be shown (Fig. 3.10), that the switching temperature decreases rapidly with F layer thickness decreasing starting from $d_F^c(T \to T_c)$. Therefore the temperature induced crossover is possible only for F layer thickness in vicinity to $d_F^c(T_c)$. This fact and the experimentally observed thermally induced crossover in S/F/S sample with $d_F = 2$ nm around $T = 0.9 T_c$ bring the reasonable hypothesis that the crossing of the thickness dependence of the critical temperatures of 0 and π state is near $d_F = 2$ nm. Therefore the parameters of S/F/S samples are different from the reported data for bilayers. This agrees with the observed discrepancy of the experimental data and Fominov's model fit. Large variation of the critical temperature of trilayers does not permit the application of the models, which take into account low S/F boundary transparency.

3.3.2   Effect of ageing

Additional information is obtained by additional measurements after ageing. At zero magnetic field three reference samples: Nb and Nb/PdNi/Nb samples
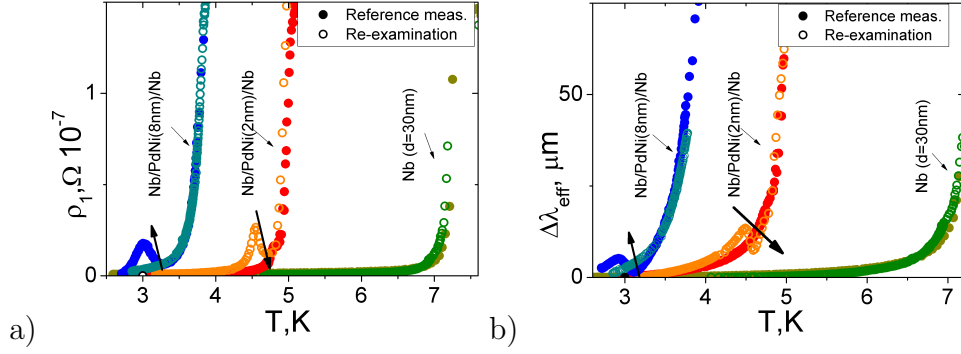
Figure 3.11: Ageing effect on the (a) microwave real resistivity and (b) the penetration depth variation temperature dependencies of Nb/PdNi/Nb samples with d_F= 0,2,8 nm

with d_F=2 nm and 8 nm, were studied. No changes in critical temperature was determined. For Nb sample both losses and penetration depth temperature dependencies agree with previous measurements.

The measurements after ageing show the appearance of the peaks on the dependencies $\rho_1(T)$ and $\lambda_{eff}(T)$ of the sample with d_F=8 nm (at the temperature T=0.73 T_c). Previously observed peaks characterized both $\rho_1(T)$ and $\lambda_{eff}(T)$ of S/F/S sample with 2-nm F layer. These changes in the temperature dependencies could result from the structural changes in the amorphous ferromagnetic layer. Since TEM measurements show that the heavy Pd atoms interdiffuse in the Nb layer and the magnetic properties of PdNi alloy are determined by the Ni concentration, interdiffusion of the Pd atoms can change the exchange energy of the ferromagnet which originates the peak appearance. Possible changes can be caused by long time thermal and mechanical stresses.

In the ageing process the level of the interdiffusion grows and structure of the sample becomes more complex. One can notice that reducing of the Nb layer due to the ageing effect can modify T_c, which is not observed in studied samples. For sample with $d_{F,nom}$=2 nm ageing could possibly form structures where Nb layers are coupled and F layer transforms to ferromagnet inclusions. Such inclusions still work as pairbrakers and T_c remains approximately unchanged. The decrease of the Nb layer thickness is small (due to the low percentage of PdNi) to be visible and it is partially compensated by NiNb phase. Peak in temperature dependence of the sample with $d_{F,nom} = 8\ nm$ can not be described by considering the trilayered structure of the samples because on the S-F boundaries the crystal multiphase structure was formed including the combinations of Ni and Pd with Nb.

3.4 Flux- flow resistivity of S/F/S multilayer

We perform measurements of the vortex motion resistivity using both the DR and Corbino disk techniques. The wideband Corbino disk method measurements cover the frequency range from 1 GHz up to 20 GHz. They are less precise than the DRs one and additional fitting procedure is needed, but they allows to measure frequency dependence of the complex resistivity. The cryogenic system which was used includes the superconducting magnet system. It allows to apply a magnetic field up to 12 T. Measurements in the temperature range 2.5 - 10 K were performed and fields up to H_{c2} were applied.

The CD is particularly sensitive to various sources of perturbation, being a nonresonant technique. In particular, it is sensitive to mismatch in the coaxial line due to, e.g., temperature gradient. Such perturbations become less and less important with increasing dissipation levels, so that in the flux-flow regime of interest here this is not a large source of uncertainty. In this study the CD technique is used to determine the vortex motion regime of the samples under study due to the its previously unknown properties.

To determine the vortex motion parameters from the CD measurements the fitting of the experimental data is needed. The motion of the vortices in presence of periodically time varying currents is defined by forces such as viscous drag force, pinning force, thermally induced force. There are several models which describe the vortex motion resistivity frequency dependence [23], [25], [27]. A complete description of the vortex motion resistivity (ρ_{vm}) can be given the Coffey-Clem model [23]:

$$\rho_{vm,CC} = \rho_1 + i\Delta\rho_2 = \rho_{ff}\frac{\epsilon + \mathrm{i}\frac{\omega}{\omega_0}}{1 + \mathrm{i}\frac{\omega}{\omega_0}} \tag{3.4.1}$$

where $\rho_{ff} = \frac{\phi_0 B}{\eta}$ is the flux-flow resistivity (vortex motion induced power dissipation only), ϵ represents the the effect of creep (thermally activated vortex depinning), ω_0 is the characteristic angular frequency which includes the depinning characteristics: pinning frequency ω_p and creep parameter $0 \leq \epsilon \leq 1$.

This model was used for the fitting of the experimental data (continuous line in Fig. 3.12). Some parameters (ρ_{ff} and viscous drag coefficient η) can be estimated without fitting to the model, but a full physical description is possible only with a correct selection of the model [27]

Apart from the need of the vortex motion model, a switching phenomenon is observed in the frequency dependence of ρ_{vm} obtained by CD technique. The nature of this phenomenon is unclear. The peaks appears upwards on ρ_1 and downwards on ρ_2 at magnetic fields $H > 0.5H_{c2}$. This is an indication of a quasi-periodical switching to a more dissipative regime. In addition,
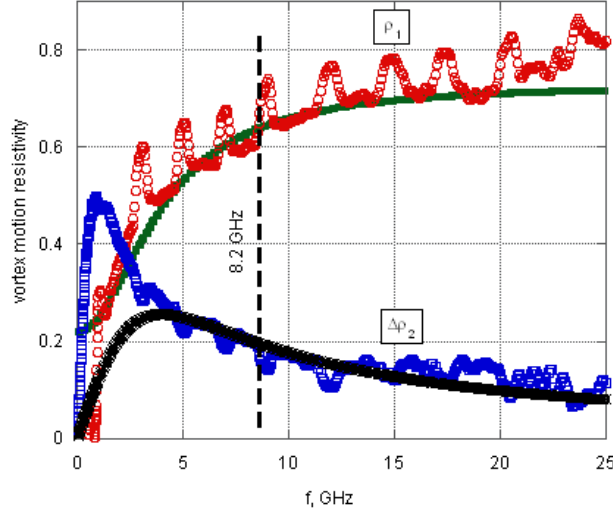
Figure 3.12: Typical measurements of $\rho_1(f)/\rho_n$ taken with the CD. The vertical dashed line is the cut at 8.2 GHz.

the amplitude of these peaks is frequency independent and microwave power independent. It could be a result of the thermal-driven metastability of the unconventional vortex motion regime generated by the strong vortex motion velocity gradients in CD [123].

The fundamental advantage of the CD resides in the possibility to gain access to the full frequency dependence of the microwave resistivity. In Fig. 3.12 I report a sample measurement of $\rho_1(\omega)$ and $\rho_2(\omega)$ as measured in the Nb film at the lowest temperature attainable and selected fields. The typical increase of ρ_1 with frequency is visible.

With increasing frequency, the real part of ρ_{vm} (ρ_1) reaches a plateau. Based on the CC model (see eq. 3.4.1) this plateau corresponds to the situation at which $\omega \gg \omega_0$. This indicates that the true flux-flow resistivity can be measured directly at high frequencies. Therefore the viscous drag coefficient can be obtained. The imaginary part ($\Im(\rho_{vm}) = \rho_2$) has a maximum at the so-called pinning frequency ω_0, that represents the transition between elastic vortex motion at low frequencies and dissipative motion at high frequencies.

In Fig. 3.13 the comparison of the field dependencies of the real part of the complex resistivity measured with DR and CD techniques is represented. The results obtained by the DR method agree with the CD measurements. Both methods have advantages and disadvantages which could be compensated. As an example the results of the measurements at a single frequency (DR method) are compensated by the wideband CD method. Noisy CD data in the temperature and field ranges up to normal state of the superconductor
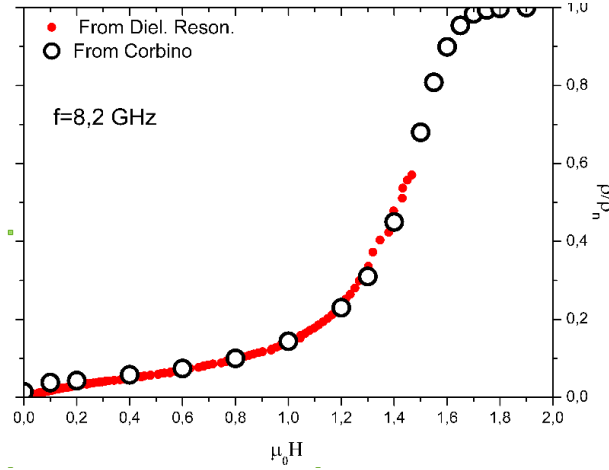
Figure 3.13: Typical measurements of $\rho_1(f)/\rho_n$ taken with the DR; crossed circles are measurements taken with the CD at 8.2 GHz (from Fig. 3.12).

are compensated by the precise DR up to 80% of H_{c2}. The impossibility of the full superconducting transition measurements which comes from the big losses in the superconductor in the normal state which reduces significantly the Q-factor of the DR and creates the difficulties in the resonant frequency determination.

The DR method is more precise, but allows to perform measurements only at a single frequency. Here the rutile DR at the $f_{res} = 8.2GHz$ was used at liquid He temperature. Based on the CD data it was shown that for the trilayered Nb/PdNi samples the characteristic frequency is much lower than the resonance frequency of the DR, and it decreases with the magnetic field due to the weakening of the pinning. Therefore, based on the vortex motion models, we can assume that the DR method allows a direct measure of the resistivity close to the flux-flow resistivity ρ_{ff} without the need for any fitting procedure. The fact that $\omega \gg \omega_0$ (CC model) was confirmed also experimentally. In that way, there is no need for precise measurements of the resonant frequency (source of the ρ_2). This simplifies the measurements process as f_{res} is more thermal fluctuation sensitive and extreme thermal stabilization is needed for its precise measurements. Thus, the field dependence of the flux-flow resistivity in Nb and Nb/Pd$_{0.84}$Ni$_{0.16}$ samples with various ferromagnetic layer thickness was studied.

First, $\rho_{ff}(H)$ in pure Nb sample was determined at the temperatures T=3.5 K-T_c. Here an upward curvature of $\rho_{ff}(H)$ was observed (Fig. 3.14a). These measurements were performed using both CD [124] and DR techniques to compare and to supplement the results.
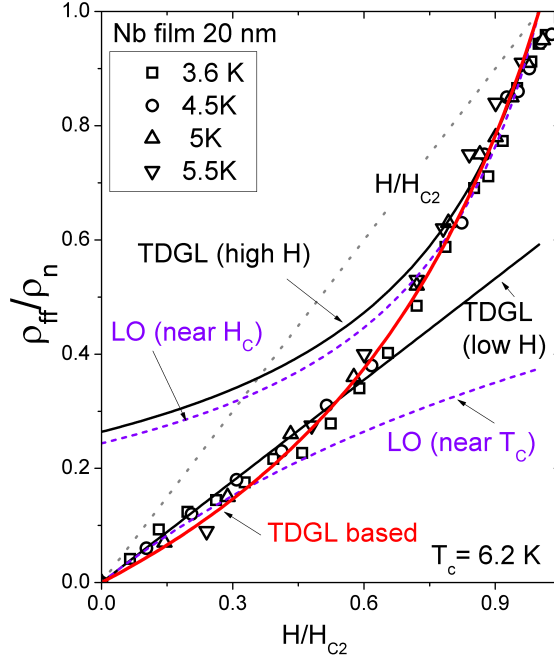
Figure 3.14: Frequency dependence of the field dependence of ρ_{ff} versus reduced field of Nb 30-nm sample

A very similar dependence characterizes also the sample with $d_F = 1$ nm. This dependence is reported in Fig. 3.15. It is worth stressing that the upward curvature and the fact that $\rho_{ff} < H/H_{c2}$ cannot be ascribed to pinning or creep since from the full frequency dependence of the real part of the resistivity based on CD measurements this vortex motion characteristics was determined and it was accepted that the measured resistivity indicates approximately the flux-flow regime.

There are few more refined theories for the flux-flow regime. The most used theory for ρ_{ff} is Bardeen-Stephen [17]. It is based on the experimental data obtained by Kim [125] which assumes the linear dependence of the reduced ρ_{ff}:

$$\rho_{ff}/\rho_n = (B/(\mu_0 H_{c2}))f(T/T_c) \qquad (3.4.2)$$

where the function $f(T/T_c)$ include non-linearity near T_c.

Hence, the observed upward curvature (see Fig. 3.14 and 3.15) reflects an overestimate of $\rho_{ff}(H)$ by the BS model. The more refined microscopic theory of Larkin and Ovchinnikov (LO) [126], also, is not able to fit our data in the whole range of the magnetic field, and only qualitative agreement is obtained at low and high fields: for $T \to T_c$ the theory predicts

$\rho_{ff}/\rho_n = 1 + \frac{1}{(1-T/T_c)^{0.5}}(H_{c2}/B)\tilde{f}(B/H_{c2})$ for H near H_{c2} one has instead: $\rho_{ff}/\rho_n = [1 + \tilde{a}(1 - B/(\mu_0 H_{c2}))]$. The fit of the experimental data is presented in Fig. 3.14 and 3.15.

The upward curvature was observed, also, in Nb_3Ge [127] and MoGe [94]. An alternative way to describe the experimental data comes from the time-dependent Ginzburg-Landau (TDGL) framework. We found that a full calculation within the TDGL theory [128] matched very well our data. For dirty superconductors the normalized ρ_{ff} field dependence of can be written as [129]:

$$\frac{\rho_{ff}}{\rho_n} = \frac{ua}{2}(H/H_{c2}) \tag{3.4.3}$$

at low fields, and

$$\frac{\rho_{ff}}{\rho_n} = 1 + \frac{u}{2}\frac{1 - H/H_{c2}}{\beta(1 - 1/2k^2)} \tag{3.4.4}$$

at high fields

A simplified relation within TDGL theory was proposed in [94], where the dependence for the normalized flux flow resistivity was given in the following form:

$$\frac{\rho_{ff}}{\rho_n} = \left[1 + \frac{\mu_0 H_{c2} - B}{\alpha B}\right]^{-1} \tag{3.4.5}$$

where α is a constant and it varies between 0.1 and 0.4 for our data.

This model fits well experimental dependence $\rho_{ff}(H/H_{c2})$ up to H_{c2}.

In Fig. 3.16 the normalized field dependence of ρ_{ff} is shown for different temperatures from $T=0.5T_c$ up to $T=0.98T_c$ in S/F/S sample with $d_F=2$ nm. For this sample change of the curvature with temperature and with magnetic field was observed. One has to note that this result is correlated to the observation without the magnetic field, where a peak was determined on the temperature dependencies of the complex resistivity. As opposed to the pure Nb sample, where the reduced field dependencies ρ_{ff} are scalable with H/H_{c2}, in the sample with $d_F=2$ nm this is impossible.

A possible speculation of this phenomenon is that, with the increase of the ferromagnet layer, the order parameter acquires a modulation across the sample (connected to the observed oscillated dependence of $T_c(d_F)$ [105]). The magnetic field triggers this delicate state, inducing a relatively wide region where the order parameter is substantially depressed. The electromagnetic field, uniform along the thickness of thin films, would give a response as if part of the multilayer would be essentially normal (effective thickness smaller than the geometrical thickness), and dissipation larger than expected would be observed.
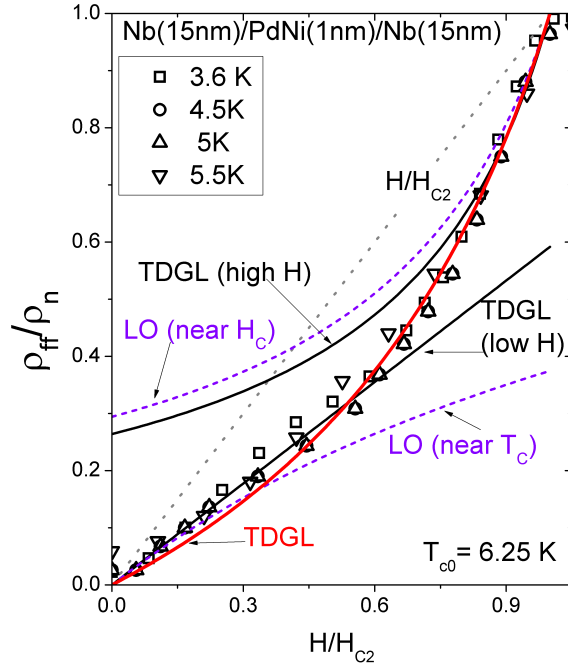
Figure 3.15: Normalized flux flow resistivity magnetic field dependence in the sample with d_F=1 nm
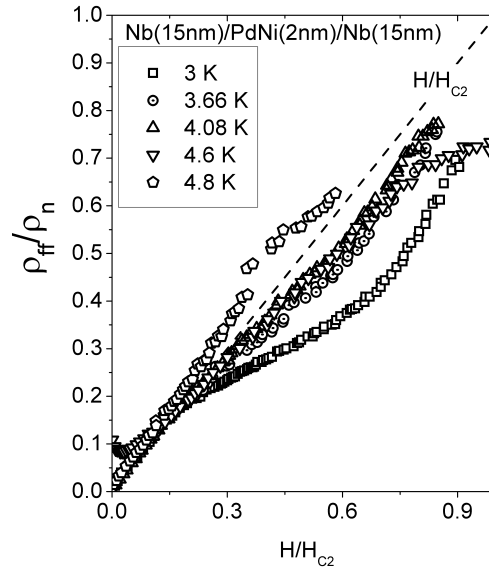
Figure 3.16: Normalized flux flow resistivity magnetic field dependence in the sample with d_F=2 nm
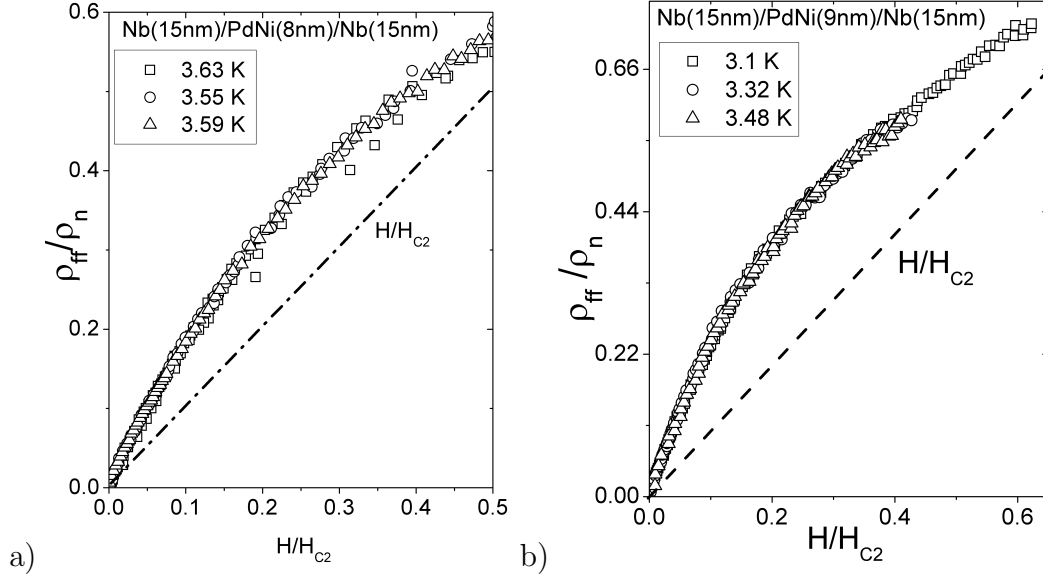
Figure 3.17: Normalized flux flow resistivity magnetic field dependence in the sample with $d_F=8$nm and $d_F=9$nm

Fig. 3.17a,b show the reduced flux-flow resistivity of the samples with thicker ferromagnetic layer. Here a clear downward curvature is determined. For both samples ($d_F=8$ nm and $d_F=9$ nm) ρ_{ff} can be scaled with H/H_{c2}, which indicates an "intrinsic" nature of ρ_{ff} even if the curvature does not find an explanation in existing theories.

To check if the disorder affect the observed behaviour, extended X-ray absorption spectroscopy (EXAFS) at the Nb K-edge is used to probe the local atomic structure on the samples under study. These results were discussed previously. The study shows that there is no correlation between the ferromagnetic layer thickness and the disorder. Shortly, this study showed independence of the disorder level in the samples with ferromagnetic layer thickness and only slightly bigger disorder in Nb layer in the sample with $d_F=2$ nm was detected.

For all the samples studied the upper critical field H_{c2} was determined experimentally. A linear temperature dependence of H_{c2} was observed (see Fig. 3.18). This result is in agreement with models in the literature and with experimental results in S/F structures [130]. It is shown that, with increasing d_F, the slope of the $H_{c2}(T)$ decreases from $\mu_0 H_{c2}/T=3.46$ TK^{-1} for $d_F=1$ nm to $\mu_0 H_{c2}/T=1.25$ TK^{-1} for $d_F=9$ nm.

To compare the measured dependencies I draw the flux-flow resistivity field dependencies of the measured samples on one figure. In Fig. 3.19 the field de-
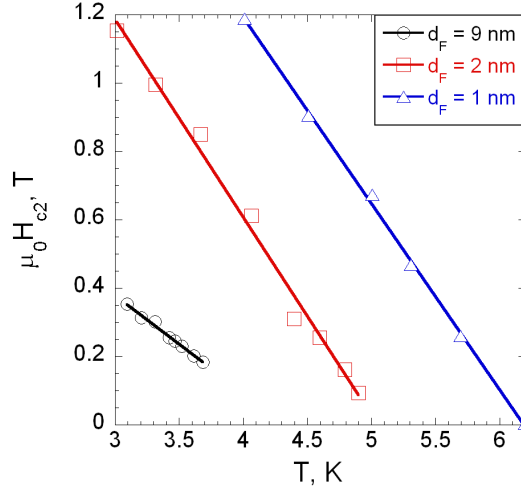
Figure 3.18: Critical temperature field dependence for the samples with different d_F

pendence of the normalized flux flow resistivity for the three multilayer samples is shown for $T/T_c \sim 0.8$. It can be seen that by increasing the thickness d_F the field dependence of ρ_{ff} progressively changes curvature, from upward for $d_F=1$ nm to downward for $d_F=9$ nm. For all samples there is no proportionality of ρ_{ff} with the reduced field H/H_{c2}, as predicted by the BS model, neither is possible a fit with the TDGL expression (eq. 3.4.5) due to observed downward curvature. While the samples with very small d_F behave essentially like an ordinary superconductor, as previously shown, increasing of d_F induces a progressive crossover between a "conventional" behaviour and a novel flux flow regime.

Fig 3.20 reports ρ_1/ρ_n as a function of the ferromagnetic layer thickness d_F at fixed normalized magnetic field $h=H/H_{c2}$ and temperature $t=T/T_c$. The date are compared with theoretical predictions. It is clearly seen that, the BardeenStephen limit is exceeded as d_F grows and the TDGL theory applies only at low d_F. It is highlighted how, by increasing d_F, dissipation in the vortex core changes from a conventional behaviour to a strongly dissipative regime, which can be an indication of new phenomena in the vortex cores. These results indicate that an extension of the measurements in samples with different d_F, and possibly with different F materials, would be useful to clarify the anomalous flux-flow behaviour here observed.

From the measurements taken with the DR one directly obtains ρ_1/ρ_n at 8.2 GHz, which is very close to the real ρ_{ff}. To compare this result with the data obtained with CD, ρ_1 at 8.2 GHz and the resistivity, which corresponds
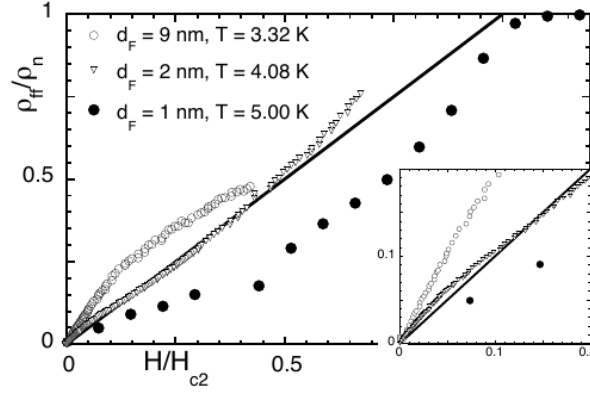
Figure 3.19: Normalized flux flow resistivity (ρ_{ff}/ρ_n) vs. reduced field (H/H_{c2}) at approximately the same reduced temperature t$\approx$0.8 for three trilayers with d_F=1, 2, 9 nm. Continuous line: BS prediction ($\rho_{ff}/\rho_n = (B/(\mu_0 H_{c2}))$). In the inset the enlargement at small reduced fields is shown.
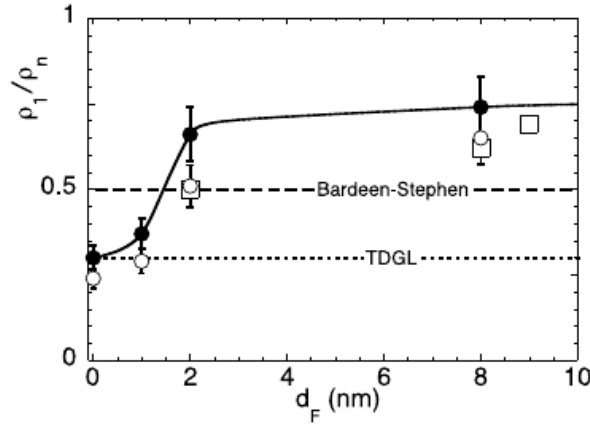
Figure 3.20: Measurements of ρ_1/ρ_n at t=0.86 and h=0.5 as a function of d_F. Full dots: plateau resistivity (approximation to ρ_{ff}) as measured with the Corbino disk. Continuous line is a guide to the eye. Open circles: ρ_1/ρ_n at 8.2 GHz from the CD measurements at 8.2 GHz. Open squares: ρ_1/ρ_n obtained with the dielectric resonator at 8.2 GHz.

to the plateau on the frequency dependence of the resistivity (an estimate of ρ_{ff} (see eq. 3.4.1)) were determined from CD measurements. In Fig. 3.20 the data for ρ_1/ρ_n at h=0.5 and t=0.86 as a function of d_F. It has to be noted that at large d_F, ρ_1/ρ_n at 8.2 GHz approaches ρ_1/ρ_n at the plateau. This is a direct indication that vortex pinning becomes less effective with the increase of the ferromagnetic layer thickness. This figure clearly shows the good agreement of the measurements with CD and DR at the same frequency, as already noticed (see Fig. 3.13). It is shown that ρ_1/ρ_n clearly increases with d_F, and reaches values well above the BS limit at large d_F. This is unexpected, since the BS value should be an upper limit. The horizontal dashed line is the BS prediction based on eq. 3.4.2. The horizontal dotted line is a full calculation within a time-dependent GinzburgLandau (TDGL) framework [94] as reported in [128], where the dc flux-flow resistivity was found to follow closely the TDGL calculation. As it was shown, at low d_F (including pure Nb) the TDGL model is compatible with the data. At large d_F, the experimental ρ_1 exceeds the BS value. Since the true ρ_{ff} is not smaller than the measured ρ_1, this is a direct demonstration that the flux-flow resistivity in our superconductor/ferromagnet/superconductor trilayers exceeds the ratio $\rho_n H/H_{c2}$. This observation points to new phenomena in the vortex cores

The CD measurements highlight the observed phenomenon. Fit of the measured frequency dependence of the real part of the vortex motion resistivity by equation 3.4.1 yields the vortex parameters with a small uncertainty. From this fit such vortex parameters as pinning coefficient and creep factor were determined. They are reported in Fig. 3.21. Here, we observe that the ferromagnetic thickness d_F has a dramatic influence on pinning and creep. In pure Nb, the depinning frequency $\nu_p \approx 3.5$ GHz points to rather strong pinning, in agreement with other estimates [131]. The sample with thinner d_F does not change much in pinning, but the sample with d_F=2 nm shows an abrupt collapse of the depinning frequency to $\nu_p \approx 2$ GHz. By contrast, thermal activation increases sharply immediately when ferromagnetic layer exists, and steadily keeps increasing with increasing d_F. Thus, S/F/S multilayers clearly show a much weaker pinning and larger thermal activation.

Comparison of this result and local structure measurements shows that there is no visible correlation between the disorder and the change in ν_p and ϵ. In fact, while the local structural disorder is larger in S/F/S trilayers than in the pure Nb film, the trend is not a monotonous function of d_F. The larger disorder is found by EXAFS in the sample with d_F=2 nm, which does not exhibit neither the weakest pinning, nor the larger thermal activation. Thus, I must argue that the magnetic properties of the F layer play a role in modifying the superconducting response of trilayers. In fact, both the depin-
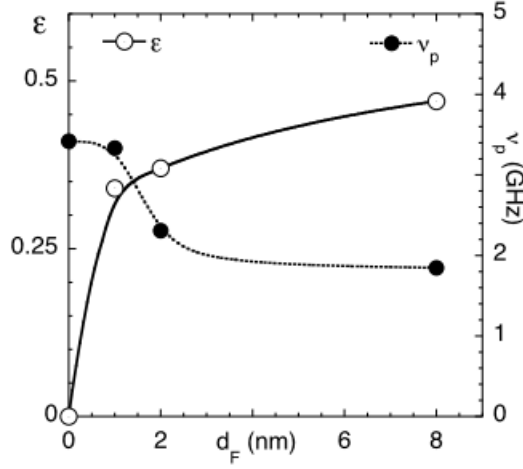
Figure 3.21: Pinning parameter ν_p (depinning frequency), right axis, and creep parameter, left axis, as a function of the ferromagnetic layer thickness d_F. As it can be seen, the increase of the ferromagnetic thickness determines a decrease of pinning strength and an increase of thermal creep. All measurements have been taken at t=0.86 and h=0.5. Lines are a guide to the eye

ning frequency and the creep factor are related to the condensation energy: the largest the condensation energy of the condensate, the larger the pinning strength, the smaller the creep factor. Thus, it can be reasonably argued that the ferromagnetic layer affects vortex pinning and creep through a reduction of the condensation energy. This explanation would be in agreement with the observed reduction of the superfluid fraction observed in S/F bilayers [112].

3.5   Conclusions

The dielectric resonator technique allows to access the microscopic properties of the superconducting structures with good sensitivity. It was shown that this type of the measurements gives access to the flux-flow resistivity regime in superconductors in the vortex state. The disadvantage of the measurements at a single frequency is compensated by wideband measurements. Comparison of two different techniques allows to obtain more information.

Nb/Pd$_{0.84}$Ni$_{0.16}$/Nb samples with different ferromagnetic layer thickness were studied both at zero magnetic field and in the mixed state. With DR the resistivity, which is near the flux-flow (ρ_{ff}) value, was measured. CD data shows the full frequency dependence of the complex resistivity and give direct measurements of the depinning frequency and of ρ_{ff}.

I have shown that ρ_{ff} never obeys the BS model in a regime where the model itself is supposed to hold. At small d_F, and in the pure Nb sample, ρ_{ff} is lower than predicted by BS model. This observation is compatible with existing models for ρ_{ff} based upon microscopic LO or TDGL calculations, and they are in agreement with data in the literature. By contrast, at relatively large ferromagnetic thickness ($d_F > 2$ nm) one finds, that ρ_{ff} exceed the BS value and can not be fitted by existing models for ρ_{ff}.

Chapter 4

Study of the anisotropy in YBCO/BZO

4.1 Introduction

In the last years several groups devoted many efforts to the improvement of the transport properties of type-II high temperature superconductors (HTS), mainly by increasing the maximum current (critical current J_c) and field at which superconductor remains lossless. The dissipation in the mixed state is due to the motion of vortices. Their mobility is reduced in presence of crystal defects or impurities, which act as pinning centres for the vortices. Hence, one possible way to reduce the vortex mobility is the artificial introduction of additional pinning centres, which can be point-like [132] or columnar-like [133]. In ref. [134], a method for increasing the pinning by using insulating $BaZrO_3$ (BZO) inclusions was proposed for $YBa_2Cu_3O_{7-\delta}$ (YBCO).

The effectiveness of artificial inclusions depends also on the growth technique (epitaxial growth, eg. by pulsed laser deposition (PLD), or chemical deposition from liquid phases (CSD)). In the following, I illustrate the results of a microwave investigation on BZO added YBCO thin films grown by different techniques (PLD and CSD).

4.2 Scaling approach

In this section anisotropic materials are considered. However, main theories assume an isotropic properties. The interpretation of experimental data in anisotropic materials the scaling approach was proposed [15].

Within it, the uniaxial anisotropy of HTC gives rise to electronic mass anisotropy, which defines the so-called anisotropy ratio $\gamma^2 = M/m$, where

$m = m_x = m_y$ is the in-plane mass, and $M = m_z$ is the mass along the anisotropy axis. The scaling approach is based on the G-L equation for the isotropic superconductor. The anisotropy is introduced in the Gibbs free energy by rescaling various quantities as follows: vector potential is scaled as $A = (\widetilde{A_x}, \widetilde{A_y}, \widetilde{A_z}\gamma)$; coordinates as $r = (x, y, z) = (\widetilde{x}, \widetilde{y}, \widetilde{z}/\gamma)$; magnetic field is scaled as $B = (\widetilde{B_x}\gamma, \widetilde{B_y}\gamma, \widetilde{B_z})$ (no field fluctuations are taken into account). The pinning was introduced by a scalar disorder in the G-L coefficient describing disorder in the transition temperature T_c $a(r) = a_0 + \delta a(r)$, where $\langle \delta a(r) \rangle = 0$ and $\langle \delta a(r) \delta a(r') \rangle = \zeta \delta \langle r - r' \rangle$.

The minimization of the magnetic field energy gives the rescaled magnetic field $\widetilde{B} = (H_x/\gamma, H_y/\gamma, H_z)$. Therefore, in the rescaled case the magnetic field reduces to $\widetilde{B} = \varepsilon_\theta B$ where $\varepsilon_\theta^2 = \gamma^{-2}\cos^2(\theta) + \sin^2(\theta)$ and θ is the angle between the anisotropy axis and the applied magnetic field.

The general scaling rule states that each quantity of the uniaxially anisotropic superconductor (Q) can be obtained from the isotropic case quantity ($\widetilde{Q}$) [15, 14] as:

$$Q(\theta, H, T, \xi, \lambda, \varepsilon, \zeta) = s_Q \widetilde{Q}(H/\gamma, T\gamma, \xi, \lambda, \varepsilon, \zeta\gamma) \qquad (4.2.1)$$

where $\xi, \lambda, \varepsilon, \zeta, H$ are in-plane coherence length, in-plane London penetration depth, anisotropy, scalar disorder strength and applied tilted magnetic field respectively.

Scaling factors for various quantities are different: $s_Q = \varepsilon_\theta$ for the volume, energy and temperature; $s_Q = 1/\varepsilon_\theta$ for the magnetic field. The scaling rule can be used for the transformation of the known Q for isotropic case to the results describing an anisotropic material. For the purpose of this work the scaling rule allows to check of the experimental data. The scaling rule is valid only for the samples in which there is no directional pinning present. Therefore, the scaling rule allows to separate the parameters which are affected by natural the anisotropy of the superconductor itself from extrinsic effect which raises to not scaled quantities.

4.3 Anisotropic flux-flow resistivity

The measurement technique, which is based on the dielectric resonator, allows to induce circular currents on the sample surface. This fact makes the comparison of the experimental data and a theory difficult. Part of the measurements, concern the study of the directionality in superconductors with artificial pinning centres. It requires an external magnetic field tilted with respect to the axis of the anisotropy. The circular current and tilted magnetic field leads to
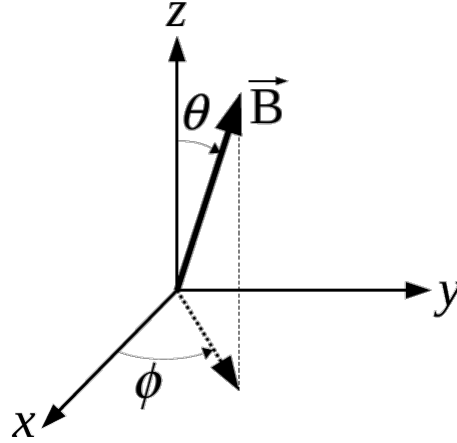
Figure 4.1: The definition of the magnetic induction field B applied along a generic direction at the polar and azimuthal angles.

a Lorentz force which varies with the angle.

In ref. [135] the theory, in which the flux-flow resistivity in the anisotropic superconductors has been developed. It is based on the TDGL theory and takes into account the main sources of the dissipation in HTS in the flux-flow state: Joule heating and relaxation of the order parameter. An anisotropic tensor of the resistivity is introduced. The external current in anisotropic SC is defined as the sum of the transport dissipative current $(\overrightarrow{J^T} \perp \overrightarrow{B})$ and supercurrent in the direction of the external magnetic $(\overrightarrow{J^s} \parallel \overrightarrow{B})$ field which describes the whole translation of the superfluid: $J^{ext} = J^T + J^s$. The flux-flow resistivity tensor can be defined from the relation:

$$J_i^T = E_j/\rho_{i,j} \tag{4.3.1}$$

where the transport current J_i^T is the spatial average of the electric current density.

For the purpose of this thesis the current J_i^T is considered to be applied along the surface of the sample (ab-plane) along a single direction. Here the crystallographic axes of the sample are taken as x≡a, y≡b and z≡c. The direction of the external magnetic field is defined by polar coordinates with respect to the c-axis: $\overrightarrow{B} = (B_1, B_2, B_3) = B(\sin\theta sin\phi, \sin\theta\cos\phi, cos\theta)$ (see Fig. 4.1), where θ is the angle between the c-axis of the superconductor and the applied magnetic field. ϕ is the angle between the applied external current and the projection of $\overrightarrow{B}$ on ab-plane. Indexes 1, 2, 3 indicate the directions along a, b and c axis correspondingly.

The electric field, induced by the vortex motion $\overrightarrow{E} = (E_1, E_2, E_3)$ is always perpendicular to $\overrightarrow{B}$. This restricts the relative orientation of the transport current and magnetic field: $\rho_{i,j} B_i J_i^T = 0$. In anisotropic superconductors this relation can be rewritten in the following form:

$$\rho_{11} J_1^T B_1 + \rho_{22} J_2^T B_2 + \rho_{33} J_3^T B_3 = 0 \qquad (4.3.2)$$

where the Hall elements in the resistivity tensor $(\rho_{ij}, i \neq j)$ are ignored due to their smallness with respect to the diagonal (dissipative) elements.

One can derive the flux-flow resistivity for the axial anisotropic material as was done in ref. [136, 137]:

$$\rho_{ff}(\theta, \phi) = \rho_{11}(\theta) \frac{\rho_{11}(\theta) \sin^2 \theta \sin^2 \phi + \rho_{33}(\theta) \cos^2 \theta}{\rho_{11}(\theta) \sin^2 \theta + \rho_{33}(\theta) \cos^2 \theta} \qquad (4.3.3)$$

where ρ_{11}, ρ_{33} are the intrinsic a, b plane and c axis flux flow resistivity. and ρ_{ff} stands for the experimentally measured, in-plane flux flow resistivity.

This relation was, also, obtained in [138, 139] by using the more general approach with the use of the tensor algebra. The relation 4.3.3 can be simplified at certain conditions: 1) the anisotropic scaling applies, 2) the flux flow resistivity is linear with the field (Bardeen-Stephen model [17]), and 3) $\rho_{33}/\rho_{11} \simeq \gamma^2$. Then, it is possible to recalculate the approximate equation.

$$\rho_{ff}(\theta, \phi) = \rho_{ff,11}(B/B_{c2}(\theta)) \frac{\gamma^{-2} \sin^2 \theta \sin^2 \phi + \cos^2 \theta}{(\gamma^{-2} \sin^2 \theta + \cos^2 \theta)} = \rho_{ff,11}(B/B_{c2}(\theta)) f_L(\theta, \phi)$$
$$(4.3.4)$$

In this relation $\rho_{ff,11}(B/B_{c2})$ is related to the intrinsic a-b plane resistivity. It can be determined experimentally by measurements in magnetic field applied parallel to the c-axis (see eq. 4.3.3 and [136, 137]). The second term contains the extrinsic angular dependence and can be represented as scaling function $f_L(\theta, \phi)$.

At the angle $\phi = \pi/2$ the magnetic field is perpendicular to the current, one has direct access to the intrinsic flux-flow resistivity [138]. The flux-flow resistivity $\rho_{ff}(\theta, \phi)$ is the quantity which can be determined experimentally. To access the intrinsic flux-flow resistivity, the function $f_L(\theta, \phi)$ has to be determined, which, also, need the knowledge of the anisotropy factor γ.

In practice for measurements of the resistivity in a.c. the techniques, in which the rotational symmetric planar current exists, are used. For circular planar currents and uniaxial anisotropy of the sample, the measured resistivity $(\rho_{ff,eff}^\circ(\theta))$ is represented as an angular average over the current pattern over

all possible values of ϕ:

$$\rho^{\circ}_{ff,eff}(\theta) = \frac{1}{2\pi} \int_0^{2\pi} \rho_{ff}(\theta, \phi) d\phi \qquad (4.3.5)$$

This relation results in:

$$\rho^{\circ}_{ff,eff}(\theta) = \rho_{ff,11}(B/B_{c2}(\theta)) \frac{\frac{1}{2}\gamma^{-2}\sin^2\theta + \cos^2\theta}{\gamma^{-2}\sin^2\theta + \cos^2\theta} = \rho_{ff,11}(B/B_{c2}(\theta))f_L(\theta)$$
$$(4.3.6)$$

It implies, that an intrinsic flux-flow resistivity $\rho_{ff,11}(B/B_{c2}(\theta))$ can be extracted. But still the scaling function $(f_L(\theta))$ has to be determined.

4.4   Samples under study

The film samples, used during this work were grown at ENEA, Frascati. The sample quality was checked by various techniques. The ENEA group also performed the measurements in d.c. to show the effect of the BZO on the pinning.

Two sets of samples were prepared: pure $YBa_2Cu_3O_{7-x}$ samples and $YBa_2Cu_3O_{7-x}$ with added $BaZrO_3$ inclusions, using two different growing techniques. The first set of samples included YBCO /BZO prepared by pulsed laser deposition (PLD) with a BZO concentration of 0% and 5%. The samples, 120-nm thick and, c-oriented, were grown at identical conditions to separate the effect of BZO.

The second class of samples included YBCO with 0% and 10% of BZO, grown using CSD metal-organic decomposition technique (CSD) on $SrTiO_3$ substrate. This method is cheaper and, most important, scalable with respect to PLD, in the perspective of a production process. The CSD film samples are characterized by a thickness of 230 nm.

4.4.1   YBCO/BZO samples prepared by PLD

In this section I present the results of the study of two series of the samples grown using the PLD: pure YBCO and YBCO with 5 mol. % of BZO inclusions.

Composite YBCO/BZO targets were obtained by mixing YBCO powders and BZO powders obtained either by solid state reactions or by chemical decomposition. The obtained targets and a pure commercial YBCO target were used in PLD deposition processes in order to grow superconducting thin films.

The films were grown on (00l) $SrTiO_3$ single crystal substrate using a 308 nm XeCl excimer laser (Lambda Physik 110i cc) with 2-3 J/cm^2 energy density and with a repetition rate of 10 Hz. The substrate temperature and the background oxygen pressure during the deposition of YBCO-BZO films have been varied in order to optimize the films critical temperature. The number of laser shots was 7000 corresponding to a film thickness ranging from 120 to 150 nm, confirmed by stylus profilometer measurements performed on each sample after patterning [140].

Structural study of the samples was done by X-ray technique. X-ray diffraction spectra recorded in the $\theta - 2\theta$ configuration revealed an epitaxial growth of (00l) -oriented YBCO films with a (005) YBCO rocking curve full width half maximum (FWHM), which was less than $0.2°$, evidencing good structural properties. The BZO crystallites were (h00) oriented, this indicates a preferred out of plane alignment between BZO and YBCO cells [140].

The crystal structure was checked by Scanning Transmission Electron Microscopy (STEM). On the STEM image (see Fig. 4.2) the columnar-like defects are well recognizable and approximately perpendicular to the film surface. These defects are not typical for the pure YBCO films. SEM investigation after chemical etching showed a surface areal density of pits consistent with the density of nanorods given by STEM. From the STEM measurements the average size of BZO particles can be evaluated. The average diameter results to be s_d=5−7 nm, and the density of columnar defects are n_d =10-20 μm^{-2} and n_d=600 μm^{-2} for YBCO and 5 mol.% YBCO-BZO correspondingly [141]. Similar results were obtained by etching in a solution of 1 vol.% Br in ethanol. The YBCO film exhibits larger and less dense etch pits if compared with 5 mol.% YBCO-BZO film. This method assumes that the density of etch pits on the film surface is the same as the density of linear defects inside the film structure. By sampling different region of the surface it is possible to obtain a reliable mean value of the defect density. The lattice fringes visible on BZO particles are consistent with a cubic lattice.

The critical temperature T_c of the samples is around 90.5 K. As it was shown before [142], the BZO inclusions does not strongly affect the critical temperature of the samples.

In ref. [140] the effect of the BZO inclusions on the critical current was also studied. It was observed that the introduction of 5 mol.% of BZO increases the critical current from $0.017J_{c0}$ and $0.0025J_{c0}$ for pure YBCO at 3 and 5 T respectively, to $0.052J_{c0}$ and $0.0125J_{c0}$ for 5 mol.% YBCO-BZO film, where J_{c0} is the critical current without applied magnetic field.

The measured pinning force also shows the improvement of the pinning, as shown in Fig. 4.3a. Based on the study of the J_c(H) dependence shape for the
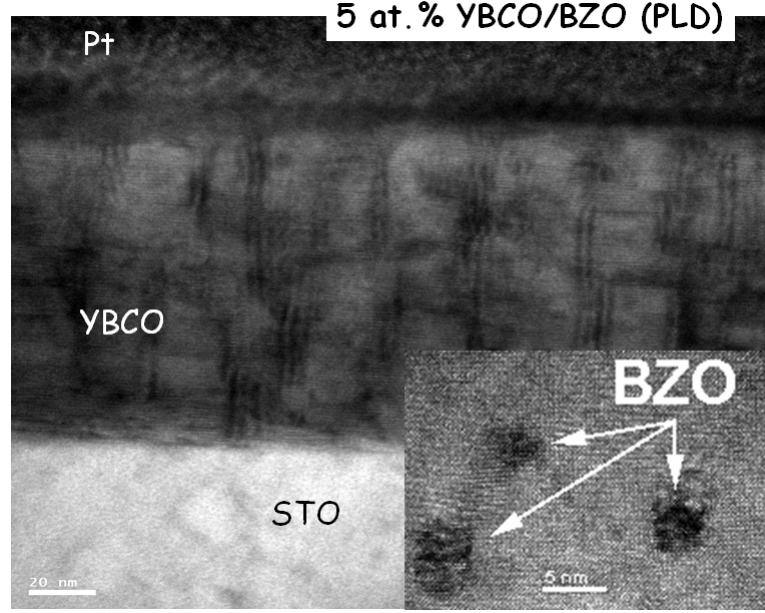
Figure 4.2: TEM image of the sample YBCO/BZO

various concentrations of the BZO, it was determined that up to 2.5 mol.% of BZO the shape of the field and angular dependencies are not changed. Samples with BZO concentration higher than 5 mol.% shows the change in both dependencies: angular and field. $J_c(H)$ shows plateau up to about 1 T in the low field region (see inset in Fig. 4.3a). By varying the angle θ between the c-axis of the sample and applied magnetic field, $J_c(\theta)$ exhibits a broad peak centred at $\theta = 0°$ (as shown in Fig. 4.3b). This suggests that the introduction of BZO does not merely improve pinning efficiency but also leads to the activation of different pinning mechanisms, namely, correlated pinning due to the presence of the columnar-like defects. $J_c(H)$ in presence of more than 5 mol.% of BZO changes its their curvature from the power law decay $(\sim H^{-\beta})$ to an exponential decay (Fig. 4.3a). This sets in at a magnetic field value, which is temperature independent. It can be determined by calculating the derivative of the dependences by the minimum in the absolute value. First derivative of $J_c(H)$ gives the minimum around $\mu_0 H$=0.9 T and suggest the change in the flux lattice dynamics. This value corresponds to the matching field effect where Mott insulator phase [143] appears [140].

Figure 4.3: a) Magnetic field dependence of the pinning force. In the inset the: Magnetic field dependence of the critical current density measured for YBCO and YBCO with 5 mol.% BZO (PLD) films at magnetic field parallel to the c-axis). b) Angular dependence of the critical current density measured for YBCO/BZO (PLD)

4.4.2   YBCO/BZO samples prepared by CSD

Another series of the samples was prepared by chemical solution decomposition (CSD-TAF-MOD). The detailed process of the preparation is described in refs. [144] and [145].

Usually the pyrolysis process is long (more than 20 hours), due to the low rate of hydrofluoric acid elimination and to preserve the YBCO film from cracks. These samples were prepared with reduced pyrolysis time (4 h) by using low fluorine contents. The coating solution was prepared starting from yttrium acetate $Y(CH_3COO)_3 + 4H_2O$, barium trifluoroacetate $Ba(CF_3COO)_2 + H_2O$ and copper acetate $Cu(CH_3COO)_2 + H_2O$ corresponding to the 1:2:3 YBCO stoichiometry. While the Ba trifluoroacetate was dissolved in methanol, the Y and Cu acetates were separately dispersed in methanol, treated with an excess of propionic acid C_2H_5COOH, further neutralized with NH_4OH until the solutions became clear. To add BZO coating solution the methanol-propionic acid Ammonia and propionic acid were added. All solutions were mixed together under stirring and concentrated by the removal of solvent under vacuum. The as-prepared solution, with a concentration of about 1.4 M, was spin coated on the substrate at a constant spin rate of 2000 rpm for 60 seconds on $SrTiO_3(001)$ single crystals (STO) [145].

In order to obtain the YBCO epitaxial films, the precursor films were heat treated in two stages. In the first stage, the samples were heat treated up to 400 °C under humidified oxygen (about 17 Torr and balance oxygen to about 800 Torr) as follows: up to 80 °C with a 10 °C/min rate, up to 200 °C/min with
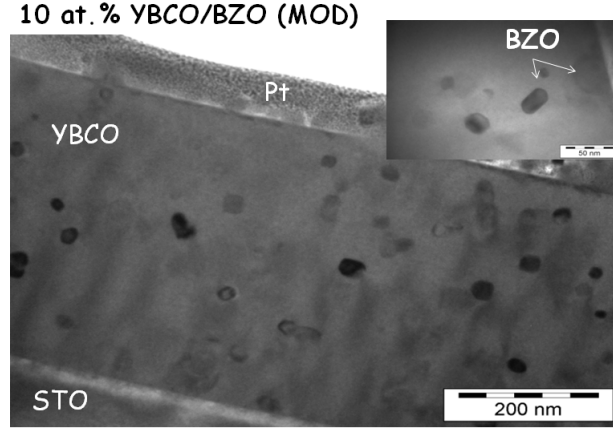
Figure 4.4: SEM images of a 130-nm-thick 10 mol.% YBCO/BZO film derived from low-fluorine modified CSD method.

2 °C/min, upto 300 °C with 0.5°C/min and finally to 400 °C with 10 °C/min, and then cooled to room temperature in the same nominal gas environment. The crystallization thermal treatment has been performed at 850 °C (heating rate of 10 °C/min) for one hour in a humid oxygen/nitrogen mixture (dew point 20 °C) and for further 10 minutes in dry oxygen/nitrogen mixture. Finally, the samples were cooled to 450 °C in the same nominal gas atmosphere with a rate of 10 °C/min, kept at this temperature for 45 minutes in oxygen and subsequently cooled to room temperature [144].

The structural properties of the YBCO films were analyzed by X-ray diffraction (XRD) technique, by the Cu K_α radiation. The $\theta - 2\theta$ spectra and ω-scans were collected using a Rigaku Geigerflex diffractometer equipped with a graphite monochromator on the diffracted beam.

A LEO 1525 field-emission high resolution scanning electron microscope (SEM) was used for film surface morphology investigations. In Fig. 4.4 the morphology of YBCO/BZO sample on STO substrates is shown. This study shows that BZO inclusions forms the defects in form of the particles with mean dimension around 25 nm. No vertical arrangement was detected, as opposed to PLD-grown samples.

The study of the effect of the BZO inclusions on the critical current in YBCO (CSD) shows that add 10 mol.% of BZO increases the critical current density from J_{c0}=1 MA/cm² for pure YBCO to J_{c0}=4 MA/cm² for 10 mol.% YBCO-BZO films at T=77 K and zero magnetic field. These values are compatible with the YBCO/BZO (PLD). Fig. 4.5a shows the field dependence of the pinning force determined for pure YBCO (CSD) and 10 mol.% YBCO-BZO (CSD) samples. Visible improvement of the pinning can be seen. However, it
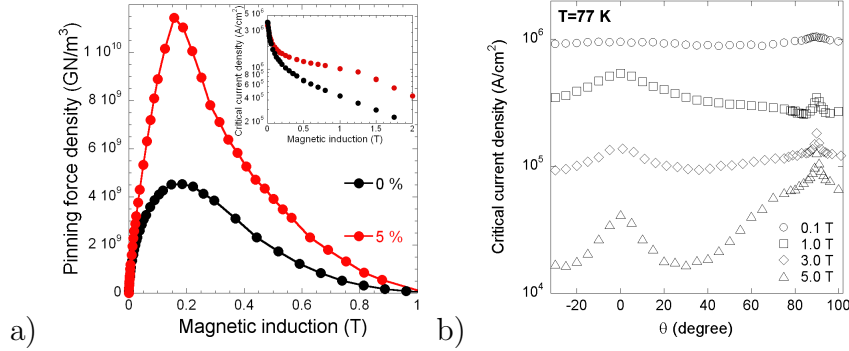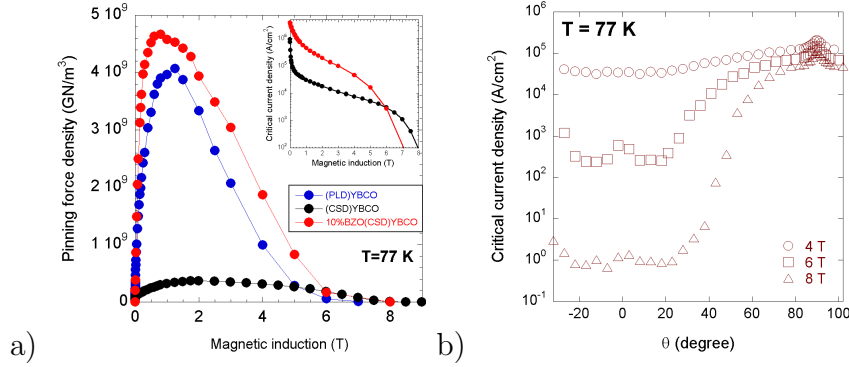
Figure 4.5: a) Magnetic field dependence of the pinning force. In the inset the: Magnetic field dependence of the critical current density measured for YBCO and YBCO/BZO (10 mol.%) CSD samples at magnetic field parallel to the c-axis).b) Angular dependence of the critical current density measured for YBCO/BZO (10 mol.%) (CSD)

has to be noted that the maximum pinning force of pure YBCO (CSD) sample is 10 times lower than the one for pure YBCO (PLD) results. The introduction of 10 mol.% BZO increases this value up to the corresponding for pure YBCO (PLD). In addition, there was no plateau detected in $J_c(H)$, which indicates the absence of the matching field effect (see inset in Fig. 4.5a), thus no matching field effect was found. The angular dependence of the critical current density (Fig. 4.5b) shows the presence of a very large peak at $\theta = 0°$, that is when external magnetic field applied parallel to the c-axis of the YBCO. But the height of this peak corresponds to the same peak in $J_c(\theta)$ for the pure YBCO (PLD) samples (no correlated pinning component) [145]. Therefore, it seems from dc. measurements that CSD-YBCO/BZO do not change the native pinning.

The study of the YBCO (CSD) characteristic in d.c. shows that the pinning force in 10 mol.% YBCO/BZO increases up to the characteristics of the YBCO (PLD) (see Fig. 4.5a). These inclusions improve the poor quality of pure CSD sample rather than to BZO effects.

4.5 YBCO/BZO-PLD microwave resistivity measurements in tilted magnetic fields

The microwave complex resistivity of the samples was measured in presence of the external magnetic field by the 47 GHz sapphire dielectric resonator (see Section 2.7). The results of the microwave measurements were compared to

d.c. critical current density measurements. An external magnetic field up to 0.8 T was generated by an electromagnet. The measurements were performed with the magnetic field tilted by an angle θ with respect to the normal to the superconductive sample surface (it corresponds to the crystal c-axis)

The main part of the measurements was performed in a temperature range sufficiently below T_c to increase its quality and minimize the contributions to the microwave response from pairbraking but still keeping an acceptable signal-to-noise ratio $\theta \to 90°$. To avoid the substrate resonances, which are typical for the $SrTiO_3$ substrates [34], the measurements at fixed temperature were done by choosing of the correct temperature outside the substrate resonances temperature range (around 80 K). The performed measurements were classified in two types: i) measurements of the response at fixed angle and varied magnetic field intensity, at the fixed temperature T=81 K; ii) angular measurements at fixed magnetic field (μ_0 H_1=0.4 T and $\mu_0 H_1$=0.6 T) and changing the angle.

Complex vortex motion resistivity was determined from the surface impedance measurements. Neglecting field-induced pair breaking effects, relevant only near T_c, the change of ρ due to the magnetic field, yields directly to the vortex motion resistivity (ρ_{vm}):

$$Z_S(H) - Z_S(0) = \Delta Z_S = \Delta R_S + i\Delta X_S = \frac{\Delta\rho}{d} = \frac{\Delta\rho_1 + i\Delta\rho_2}{d} = \frac{\rho_{vm}}{d} \quad (4.5.1)$$

where the thin film approximation $\Delta Z_s = \Delta\rho/d$, which is valid for d$\ll \lambda$, has been used for the film with thickness d=120 nm.

In Fig. 4.6a,b at various angles between the field and the complex resistivity at the field perpendicular to the sample surface is shown. In Fig.4.6c,d the measured angular dependencies of the real and imaginary parts of the complex vortex motion resistivity (sample I) at fixed fields are shown. As it can be seen, the field dependencies of both the real and imaginary parts progressively decrease with the tilt of the external magnetic field from the orientation, where it is parallel to the c-axis of the sample, to perpendicular orientation, where the magnetic field is applied along the sample surface (a-b plane). This effect can be due to the mass anisotropy and/or to some directionality in pinning properties.

To ascertain the role of directional pinning, the role of the mass anisotropy must be determined. This is usually done by the application of the so-called scaling rule to the measured data (scaling rule was discussed in Chapter 4.2). In the London approximation the thermodynamic and intrinsic transport properties obey the scaling behaviour: when, as in thermodynamic properties, the field and angular dependencies are combined into the single one on the reduced field H/H$_{c2}(\theta)$=H$\epsilon(\theta)$ [15], then, the measurements taken at different
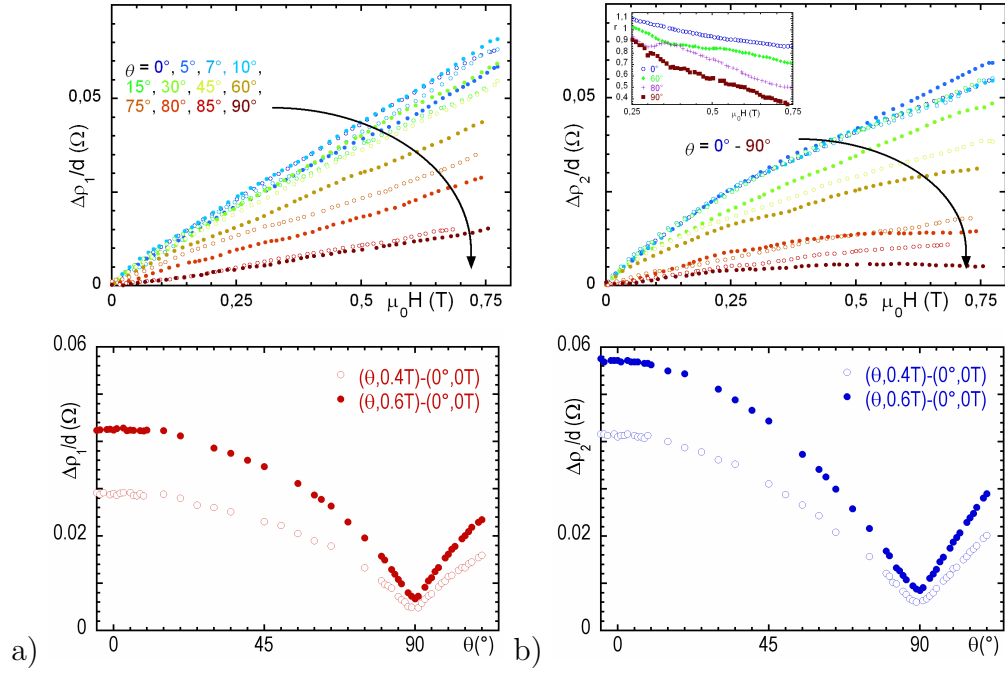
Figure 4.6: Variation of the real (a) and imaginary (b) parts of the surface complex resistivity as a function of the angle - sample II (lower plot) and applied magnetic field - sample I (upper plot) for the YBCO/BZO at T=81 K. Inset: field dependence of the ratio $r = \Delta\rho_2/\Delta\rho_1$.

fields and angles and plotted as a function of $H\epsilon(\theta)$ are expected to collapse on a single curve. It is an important point that such scaling is grounded on the existence of only one field scale, whereas extrinsic properties, such as pinning, may depends on different field scales, e.g. the matching field in samples with regular lattices of defects, and extrinsic preferential directions can exist (e.g., columnar defects at a specific angle). Thus, the scaling rule is expected to break in extrinsic-dependent parameters.

To check the possibility of the scaling of the measured complex resistivity field and angular dependencies, I use the raw data taken directly from the resonant measurements. Since, the real and imaginary parts of ρ_{vm} can be determined by following relations (see Chapter 2):

$$\Delta\rho_1 = Gd\left(\frac{1}{Q(H,\theta)} - \frac{1}{Q(H,0)}\right) = Gd\Delta(1/Q) \qquad (4.5.2)$$

$$\Delta\rho_2 = -i2Gd\left(\frac{f_0(H,\theta) - f_0(H,0)}{f_0(H,\theta)}\right) = -i2Gd\Delta f_0/f_0 \qquad (4.5.3)$$

The effect due to the error in the determination of the geometrical factor G or sample thickness d, because of its angular and field independence on the scaling rule was removed. For this purpose I will use the raw data $\Delta(1/Q)$ and $\Delta f_0/f_0$ which correspond to $\rho_{vm,1}$ and $\rho_{vm,2}$ correspondingly. Scaling rule includes some empirical scaling function $\epsilon_{emp}(\theta)$, which gives the overlapping of each field dependence to the curve taken at $\theta = 0$. This empirical function $\epsilon_{emp}(\theta)$ was chosen in order to accept some effective anisotropy, and more generally to release some possibly too tight theoretical constraint. However, even in this somewhat less rigorous version, a proper scaling of the data was not obtained. While it is possible to scale $\Delta(1/Q)$, it is never possible to scale both $\Delta f_0/f_0$ and $\Delta(1/Q)$ with the same $\epsilon_{emp}(\theta)$ as shown in Fig. 4.7.

One should consider that in the measuring system the circular currents on the sample surface might be a reason of the impossibility to scale the raw data. This can be due to the spatial variation of the Lorentz force, acting on the flux lines, with tilting of the magnetic field. This possible effect needs future investigation.

Indeed, by tilting the field away from the perpendicular orientation, fluxons are not more perpendicular to the current, this angle depends on the position on the sample surface. As a consequence, the overall effect has to be averaged over the sample surface (see eq. 4.3.5). But in this case the resistivity includes a factor proportional to the electric field originating from the Lorentz force $(f_L(\theta))$. This factor can acquire a very complicated angular dependence in anisotropic superconductors (see eq. 4.3.6 [138]). The essential point is, that $f_L(\theta)$ is multiplier to the resistivity and, also, to both $\Delta f_0/f_0$ and $\Delta(1/Q)$.
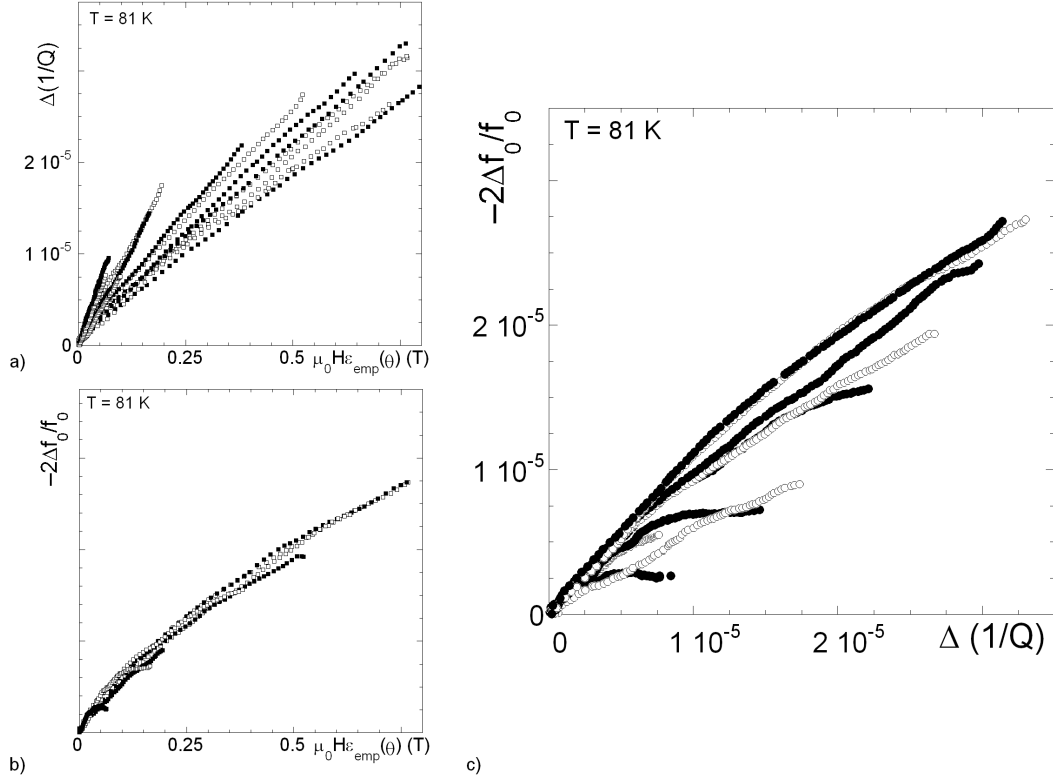
Figure 4.7: Failing of the simultaneous scaling with empirical function $\epsilon_{emp}(\theta)$ of the $\Delta(1/Q)$ and $\Delta f_0/f_0$, measured with the angles of the tilting from $\theta = 0°$ up to $\theta = 90°$ (sample I at T=81 K). It is not possible to scale both the real and imaginary part of the complex microwave response: by scaling the imaginary part (b), the real part (a) does not scale. c) $-2\Delta f_0(H, \theta)/f_0(H, \theta)$ vs $\Delta Q^{-1}(H, \theta)$, with H as running parameter and selected angles $\theta = 0° - 90°$. It can be seen that the various curves have different steepnesses and therefore do not overlap, meaning that it is not possible to make them scale through any reduced field $H\epsilon_{emp}(\theta)$.

In order to exhaustively test the possible scaling of $\Delta(1/Q)$ and $\Delta f_0/f_0$, the plot of $\Delta(1/Q)$ vs. $\Delta f_0/f_0$ was considered, which is a representation largely used in literature [146]. This type of the data representation removes the function $f_L(\theta)$ effect on the scaling. In Fig. 4.7c several curves at different θ are plotted with H taken as parameter. It is clearly seen that the various curves do not collapse together. Also, their steepness is angle dependent. This is the demonstration that the vortex complex resistivity does not exhibit angular scaling in YBCO samples with columnar-like BZO inclusions. This indicates that in the samples studied the anisotropy is caused by all three sources: anisotropy of the electron mass, pinning due to the layered structure of YBCO and due to the columnar-like BZO inclusions. Some preliminary indication can be gained by the investigation of the ratio $r = \rho_{vm,2}/\rho_{vm,1}$ (reported in the inset of Fig. 4.6b), which represents the balance between reactive and dissipative components of ρ_{vm}. It clearly shows that the dissipative component dominates up to the angle 90^0.

In order to clarify the role of the role of the different sources of the anisotropy one should note, that the complex vortex motion resistivity includes two contributions: the free vortex motion, which is an intrinsic quantity, and pinning due to the presence of the pinning centers or due to the layered YBCO structure. To separate different contributions the flux-flow resistivity, and the pinning coefficient (Labusch parameter) were extracted from field and angular dependencies of ρ_{vm}, resorting to standard vortex motion models (eg. Gittleman-Rosenblum [147]) using the methods proposed in [27].

4.6   Directionality of the flux-flow resistivity

From the measured ρ_{vm}, based on the Gittleman- Rosenblum model, the flux-flow resistivity ρ_{ff} field dependencies at different angles (sample I) were extracted. It is important to note that the angular scaling of ρ_{ff} is possible: $\rho_{ff}(H)$ can be represented as a single curve and reported as a function of the applied field scaled by an experimentally determined scaling function $f(\theta)$.

When the magnetic field is applied with an angle θ to the sample surface, the scaling property [14] predicts a dependence of the flux-flow resistivity on the magnitude of the external magnetic field and orientation as $\rho_{ff}(H,\theta) = \rho_{ff}(H/f(\theta))$, where $f(\theta)$ is the scaling function. The 3D Ginzburg-Landau theory in the case of straight current, perpendicular to the magnetic field, gives $f(\theta) = 1/\varepsilon(\theta)$, where $\varepsilon(\theta) = (\cos^2\theta\gamma^{-2} + \sin^2\theta)^{0.5}$ and $\gamma = H_{C2}(0^o)/H_{C2}(90^o)$ is the anisotropy ratio for YBCO. Indeed, $\rho_{ff}(H,\theta)$ can be scaled to a single curve (Fig. 4.9). This is a remarkable result by itself. Clearly, one has to investigate the details of the resulting function in order to check the consistency
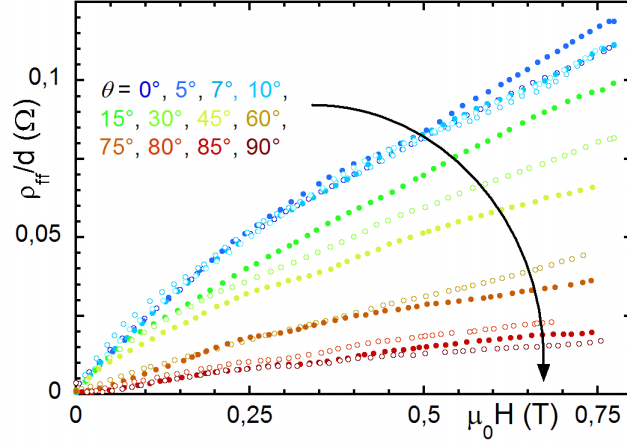
Figure 4.8: Magnetic field dependencies of the flux-flow resistivity of the I-type sample YBCO/BZO
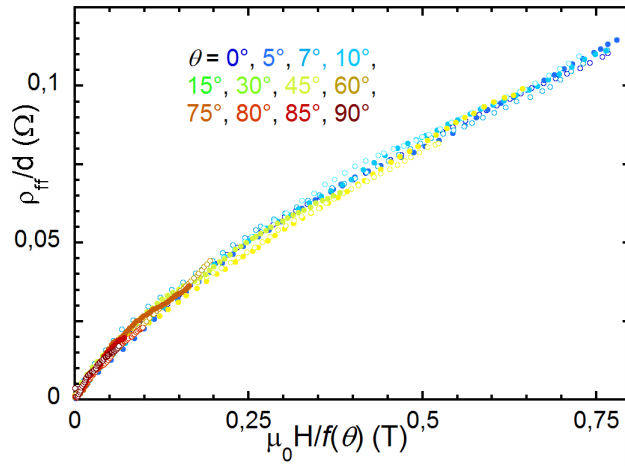
Figure 4.9: Scaling of the flux-flow resistivity over the curve $\rho_{ff}(H,\theta)$ with the rescaled field H/f(θ) (sample I)

of the results with the model. One should note that a direct application of the model for the straight current give an anisotropy ratio $\gamma = f(90^o)/f(0^o) = 12$, twice the commonly accepted value for the YBCO samples ($\gamma = 6$). It is not, however, surprising that the scaling function $f(\theta) \neq 1/\varepsilon(\theta)$. Here an additional contribution has to be taken into account: a non uniform angle between the magnetic field and local microwave current direction causes non-uniform orientation of the driving force. Using electrodynamic models for the mixed state in anisotropic superconductor, it can be shown that angle dependence ρ_{ff} can be rewritten as a function of in-plane (ρ_{ab}) and out-plane (ρ_c) resistivities. Taking also into account the observed experimental field dependence for ρ_{ff}, $\rho_{ff}(H) \sim H^\beta$ with $\beta = 0.8$, one can obtain the following scaling expression [136]:

$$f(\theta) = \epsilon^{-1}(\theta) \left[\frac{\gamma^{-2}sin^2\theta + cos^2\theta}{0.5\gamma^{-2}sin^2\theta + cos^2\theta} \right]^\beta \qquad (4.6.1)$$

where the term in square brackets is the correction due to the non-constant Lorentz force.

This equation has no fit parameters, therefore at $\theta = 0^o$ the anisotropy ratio can be determined directly using only β coefficient, which is a measured quantity.

The scaling approach can be applied also for the angular dependencies at fixed field (sample II). In Fig. 4.10a the angular dependencies of the ρ_{ff} at the fixed fields μ_0H_1=0.4 T and μ_0H_2=0.6 T is reported. In Fig. 4.10b the scaling of $\rho_{ff}(H,\theta)$ of the sample II is plotted over the curve obtained with the magnetic field parallel to the c axis, as a function of the applied field scaled by an experimentally-determined scaling function $f(\theta)$. Fig.4.10d reports the similarly scaled field-sweeps of ρ_{ff} in sample I, performed at several θ. The experimentally determined angular scaling functions for two different types of the measurements (sample I and sample II) are shown in Fig. 4.10c. They are clearly described by a unique curve that thus does not depend on the sample and on the applied field, consistently with an intrinsic phenomenon. The scaling function $f(\theta)$ agrees with the analytical equation 4.6.1. One finds as a result $\gamma = 5$, which is in the accepted interval for YBCO. It has to be noted, that the effects of the mass anisotropy and of the Lorentz force on the anisotropic response have been obtained from the analysis of ρ_{ff} alone, and they are not subjected to further adjustments.
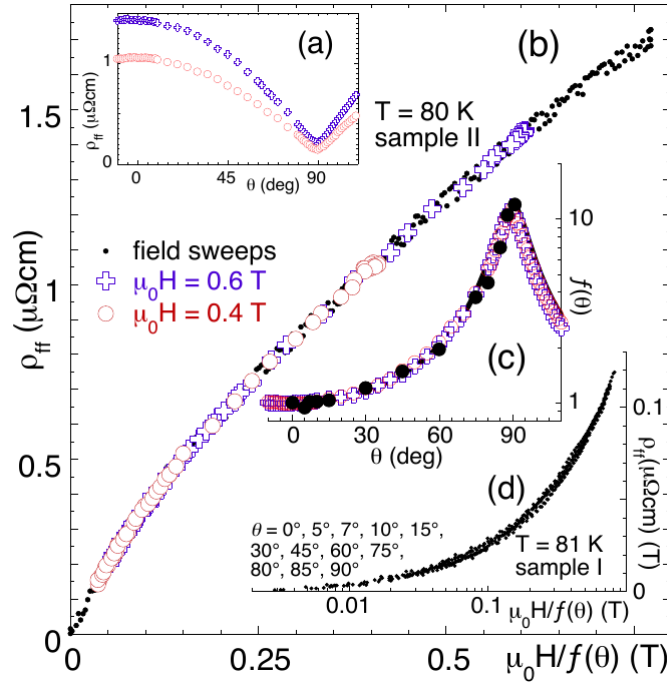
Figure 4.10: Flux-flow resistivity derived from ρ_{vm} (a): angular dependence at fixed field (sample II); (b) scaling of the data over the curve $\rho_{ff}(H, \theta = 0)$ with the rescaled field $H/f(\theta = 0)$; (c): experimental $f(\theta)$ (symbols) and comparison with the theoretical 3D expression, eq. 4.6.1 (continuous line); (d) scaling for the field-sweeps at various angles in sample I. The log scale emphasizes low-fields scaling

4.7   Directionality of the pinning coefficient

Now I comment on the results concerning the pinning constant. The directionality of the pinning was studied based on the angular dependence of the pinning coefficient in sample II with increased accuracy around the angles $\theta = 0^o$ and 90°. To obtain the angular dependence of $k_p(H, \theta)$ from the data, one has to remove the Lorentz force angular contribution, which enters in the measured quantity analogously to what happens for ρ_{ff}. From eq. 4.6.1 such correction can be easily extracted and $k_p(H, \theta)$ derived.

In Fig. 4.11 $k_p(H_i, \theta)$ $(i = 1, 2)$ is plotted. A large peak at the angle $\theta = 90°$ is seen. The increase of pinning (decrease of the dissipation) is determined both by the the mass anisotropy and the YBCO $a - b$ plane pinning. With the magnetic field applied parallel to the c axis there was no visible peak, which could indicate the effect of BZO on the pinning. But it does not imply that the angular dependence $k_p(\theta)$ is dictated only by the mass anisotropy. In this situation the scaling approach can be applied. Thus, the field dependencies of the pinning coefficient was examined.

In Fig. 4.12 the field dependence $k_p(H)$ at fixed angles and T=81 K is reported for sample I. It was determined, that up to $\theta = 60^0$, k_p is independent from the field and approximately angle independent. This behaviour can be influenced by BZO pinning centers, that oppose to the decrease of k_p with the field in pure YBCO samples.

In the intermediate region from 60° up to 80°, the field dependencies of k_p are similar to those at lower angles, although the absolute values slowly increases with the angle. Increasing θ above 80°, $k_p(H)$ changes from a constant value to a decreasing field dependence. Comparing with the field dependence of pure YBCO one can conclude that the decreasing field dependence is determined by the intrinsic anisotropy of YBCO. Summarizing, the overall results come from the interplay of the YBCO anisotropy and from BZO inclusions, but the effect of the BZO is much smaller in this angular range.

In Fig. 4.13b the angular dependence of the pinning parameter $k_p(H_{1,2}, \theta)$ is plotted. It can be seen that there is large peak at $\theta = 90°$, which is due to the effect of both intrinsic a-b plane pinning and mass anisotropy. No directional effect acting around $\theta = 0°$ seems evident, but it does not imply that the anisotropy of $k_p(\theta)$ is dictated by the mass anisotropy: for this to be true, the scaling rule should apply.

To check the scaling property [15] the $\epsilon(\theta)k_p(H, \theta)$ dependence versus $H\epsilon(\theta)$ was drawn in Fig. 4.13a, together with $k_p(H, \theta = 0°)$ as derived from the field sweep with $H \parallel c$. One can observe that in building up this dependence it is possible to remove the effective mass anisotropy: should the latter be the only source of anisotropy, Fig. 4.12 would present the collapse of the data over a
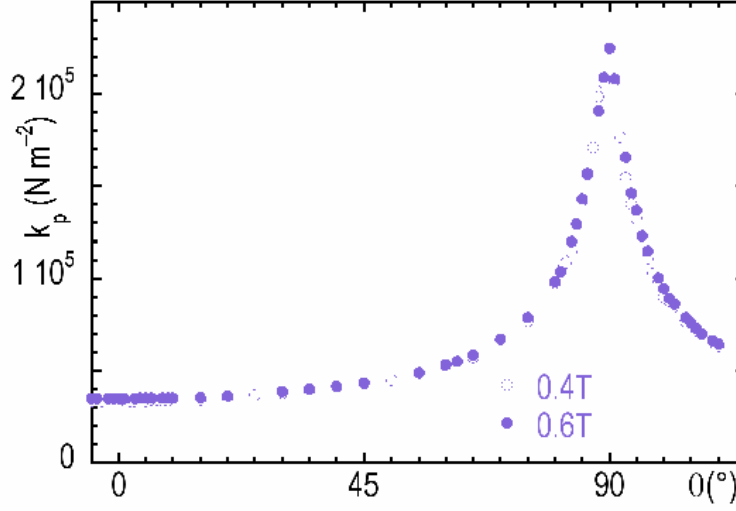
Figure 4.11:   Angular dependence of the pinning constant k_p

single curve. But it is impossible to describe all these curves as a single one, so the scaling approach can not be applied. Failing of the scaling indicates that the anisotropy of k_p originates not only from the mass anisotropy, but also from the other effects. Such directional pinning is stronger when the field is aligned with the nanocolumns (large $H\epsilon(\theta)$ in Fig.4.12a) or with the a-b planes ($\theta \rightarrow 90°$ and small $\epsilon(\theta)$ in Fig. 4.12a).

To understand better the physics of the vortex matter in YBCO with nanocolumns the comparison of the pinning constant, obtained from microwave measurements, and the dc critical current density J_c was done to compare different properties: an equivalent of J_c for short vortex displacement was derived as follows from the microwave data. The maximum pinning force (per unit length) is $k_p r_p = J_c \Phi_0$ where r_p is the radius of the random potential, which is of order ξ [148] for core pinning. In inclined fields one has [14, 10] $r_p(\theta) \sim \xi_{ab}\epsilon(\theta)$, where ξ_{ab} is the a-b plane coherence length. Thus, from microwave data an equivalent critical current density can be defined as:

$$J_{c,short}(H,\theta) = c\frac{k_p(H,\theta)\xi_{ab}\epsilon(\theta)}{\Phi_0} \qquad (4.7.1)$$

where $c \sim 1$, and the subscript "short" indicates that the d.c. and microwave vortex dynamics are different: J_c is measured in the regime where flux lines are depinned by a sufficiently strong direct current, and steady motion arises. $J_{c,short}$ is defined in the subcritical microwave currents regime, where the microwave field induces only very short (~ 1 Å) oscillations of the vortices around their equilibrium position.
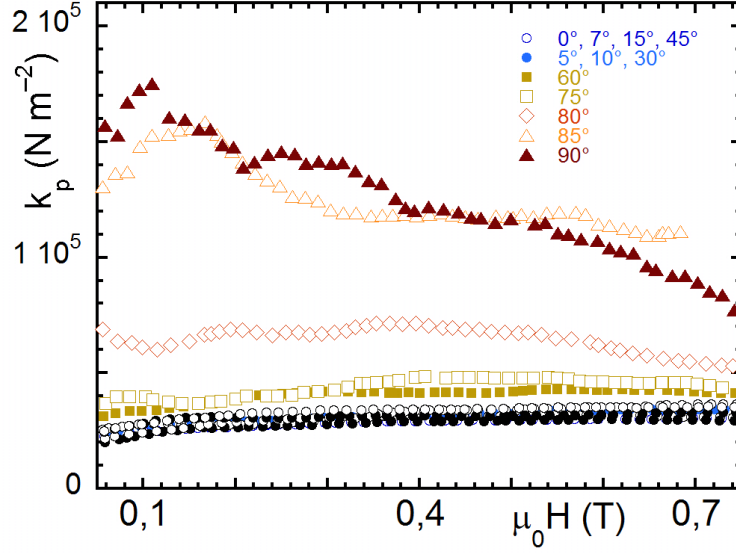
Figure 4.12: Magnetic field dependencies of the pinning constant at different angles

Comparison of $J_{c,short}$ to the actually measured dc J_c is shown in Fig.4.13c. Common features are a maximum centered at $\theta = 0°$, a local minimum around $\theta = 85°$ and a steep peak at $\theta = 90°$. The latter clearly originates from a-b plane pinning whereas the former is ascribed to the correlated pinning due to BZO inclusions [145]. It should be noted that the maximum at $0°$ is extremely wide, thus suggesting that BZO nanorods are strong pinning centers even in tilted magnetic field. Moreover, with reasonable $\xi_{ab}(T) = \xi_0/\sqrt{1 - (T/T_c)^2}$, where $\xi_0 = 12$ Å, and $c \sim 0.16$, the short-range-dynamic ($J_{c,short}$) and long-range dynamic (J_c) curves exactly coincide in the intermediate angular range $35° < \theta < 80°$. Thus, in the angular range where flux lines are most likely segmented between nanorods, the angular dependences of J_c and $J_{c,short}$ are identical, despite the very different dynamics.

However, $J_{c,short}(\theta)$ and $J_c(\theta)$ strongly depart from each other as the field aligns with the nanorods: for $\theta \lesssim 35°$ $J_{c,short}$ shows only a broad hump, over which a second, steeper hump appears in J_c. The further enhancement of $J_c(\theta)$ is then a dynamic effect: the largest peak at $\theta = 0°$ appears only when large vortex displacements are involved (dc). Thus, the important result that nanocolumns enhance J_c by means of two distinct mechanisms: strong core pinning, which gives rise to the broad hump in $J_c(\theta)$, and the reduced vortex mobility effect, which gives rise to the additional peak in $J_c(\theta)$ for $\theta < 35°$. The latter effect is a manifestation of the Mott-insulator phase for fluxons
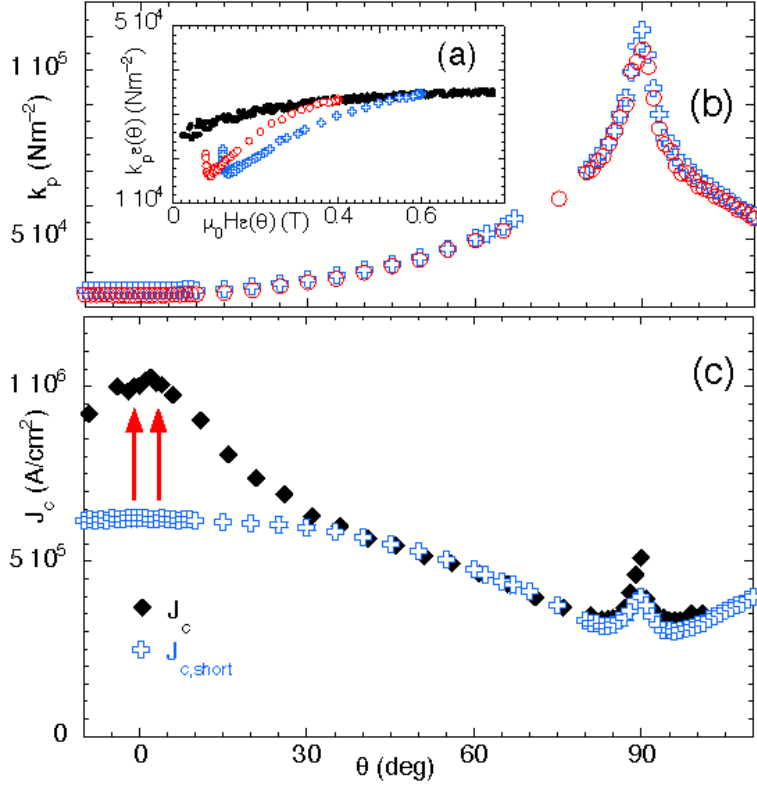
Figure 4.13: a) Failure of the scaling of $k_p(H,\theta)$ (open symbols) over the curve $k_p(H,\theta = 0°)$ (full circles). b) Angular dependence of the pinning constant k_p at fixed magnetic fields: μ_0H_1=0.4 T (open circles) and μ_0H_1=0.6 T (open crosses). c) Comparison between $J_{c,short}(0.6\,T,\theta)$ at T=80 K and $J_{c,short}(1\,T,\theta)$ at 77 K. Red arrows highlight the Mott-insulator effect.

[143]. Essentially, each vortex is pinned by an extended defect and when it is forced to move away from it by the external current, its mobility is drastically reduced by the lack of free sites where to move. When the field is tilted away from the nanocolumns, fluxons are no longer strongly pinned by the extended linear defects for the whole length, so that the Mott-insulator effect disappears at a certain angle ($\sim 35°$ in our case). Deformation of the flux lines (steplike) may yield stronger pinning than with point pins only, hence the same wide hump in $J_{c,short}(\theta)$ and $J_c(\theta)$.

This scenario is entirely consistent with the field dependence of J_c with $H \parallel c$-axis [141]: here a change of regime in the pinning force $F_p = J_c B$ with increasing field was observed. In fact, above the pseudo-matching field (the field where each linear defect accommodates one flux line) the Mott-insulator effect vanishes and the pinned vortex matter behaves more similarly to a lattice (more or less disordered) in presence of strong point pins. This is consistent with the strong extended pinning below the pseudo-matching field observed by careful analysis of the magnetization relaxation [149].

The dynamic effect on pinning due to the displacement of the vortices can be estimated by the introduction of the angular dependent parameter:

$$\alpha_\mu(\theta) = \frac{J_c(\theta) - J_{c,short}(\theta)}{J_{c,short}(\theta)} \tag{4.7.2}$$

When no dynamic effect is present, that is the critical current density does not depend on the vortex displacement, $\alpha_\mu = 0$. From the argument that led to eq. (4.7.1) one readily see that α_μ can be interpreted as the percentage increase of r_p due to the dynamic effect. In Fig. 4.14 we plot $\alpha_\mu(\theta)$. As it can be seen, $\alpha_\mu \neq 0$ when the field aligns with the directional pinning sources. In particular, α_μ drops with increasing θ, and vanishes at intermediate angles, before a further increase close to the a-b planes. The inset of Fig. 4.14 shows that α_μ drops exponentially with $\cos\theta$, the projection of the field along the nanocolumns. We found that the following empirical expression describes very well the angular behaviour of α_μ:

$$\alpha_\mu(\theta) = \alpha_\mu(0)\frac{e^{\zeta\cos\theta} - 1}{e^\zeta - 1} \tag{4.7.3}$$

where $\zeta \simeq 14.5$ is obtained from the exponential behaviour for $\cos\theta > 0.9$. The physical significance of the empirical fit is that the dynamic Mott-insulator pinning effect is a fast vanishing function of the fraction of the flux line that can be pinned and "caged" by the extended defect.
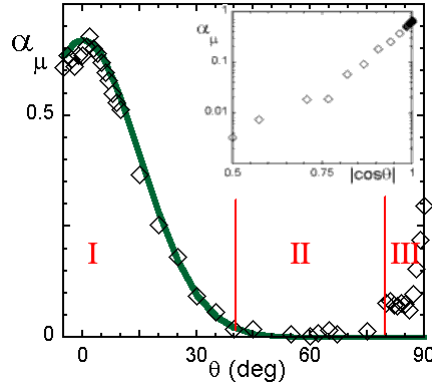
Figure 4.14: Main panel: the dynamic parameter $\alpha_\mu(\theta)$ (crossed diamonds) shows three regions: I, where dynamic effects (Mott-insulator vortex phase) increase α_μ; II, where core pinning (segmented flux lines) dominates; III, where a-b plane pinning is important. The green line is the empirical fit with eq. 4.7.3. Inset: in region I the increase in α_μ depends exponentially on the component of the field along the nanocolumns.

4.8 YBCO/BZO prepared by CSD-MOD

Study of the samples prepared by the new technique allows to improve the process of the deposition. The metal-organic decomposition method (MOD) has many potential advantages with respect to the PLD technique: this method is cheaper and more easily scalable than PLD, thus resulting in a promising approach for a future possible industrial production process. Here the quality of the YBCO/BZO film samples with thickness 400-600 nm, which were prepared using chemical solution deposition (CSD) by metal-organic decomposition method (CSD-MOD), was checked. YBCO/BZO samples with 10 mol.% concentration of the BZO inclusions were characterized and compared with pure YBCO samples grown with the same technique.

The structure of the defects induced by BZO is strongly defined by the growing technique. BZO inclusions in the YBCO samples deposited by PLD technique usually forms the columnar-like defects with diameter around 5 nm and height between 30 and 150 nm, aligned along the c-axis (or perpendicular to the sample surface). Since it was previously shown that increasing of the BZO concentration on YBCO samples deposited by PLD proportionally increases the pinning, the maximum possible concentration of the BZO was chosen for CSD deposited sample.

The signature of columnar pinning is the reduction of the vortex mobility at magnetic fields applied along the columnar defects. In Fig. 4.15 the real

and imaginary parts of the vortex motion resistivity $\Delta\rho(H)=\rho(H)-\rho(\mathring{H})$ with field applied perpendicular to the sample surface measured in pure YBCO and YBCO/BZO samples deposited by CSD technique are shown. It can be seen that the reactive component ρ_2 is ten times lower than ρ_1 for both measured samples, indicating weak pinning. At low temperatures the field dependence ρ_1(H) for pure YBCO CSD samples grows linearly, at high temperatures this dependence is characterized by the downward curvature (Fig. 4.15a), it is different with respect to the YBCO/BZO(CSD) sample, which is characterized by linear ρ_1(H) dependence in the temperature interval up to T_c. Both samples studied here are characterized by the linear dependence of $\rho_2(H)$ at low temperatures and by dependence with maximum at temperatures higher than T=70 K.

To highlight the effect of BZO inclusions, a comparison of the pinning coefficient (which is the relation between reactive and dissipative component of ρ_{vm}) $r = \rho_{vm,2}/\rho_{vm,1}$ is performed (see Fig. 4.16). The comparison of the parameter r of pure YBCO(CSD) and YBCO/BZO(CSD) indicates, that the presence of BZO inclusions does not affect much the pinning at microwave frequencies. It means that, in samples grown by CSD, BZO inclusions create pinning centres with potential wells with steepness comparable with conventional defects of pure YBCO, whence the results of microwave measurements, which probe short-range displacement of fluxons. These results are opposite to the characteristics of the CSD samples in dc [150], where it was shown that the introduction of BZO inclusions increased pinning by increasing its isotropic contribution, indicating bigger potential well depth. Therefore BZO inclusions does not effected on the correlated pining because it forms the point defects. In CSD samples BZO inclusions can be useful to increase the pinning properties of the pure YBCO (CSD) samples, which have a poor pinning characteristics with respect to the PLD grown samples, but the process is limited to dc properties.

4.9 Conclusions

In this chapter I performed the comprehensive study of the BZO inclusions on the pinning of YBCO films. Modified samples were compared with pure ones. Samples, which were grown with different techniques (PLD and CSD) were used. Study of the samples were performed at frequency 48 GHz in the pinning state. The effectiveness of the columnar pinning centers in PLD samples was observed in wide range of the angles between the c-axis and applied magnetic field. The generalized model of the vortex motion resistivity was applied for correct extraction of the DR experimental data. It was shown, that for the
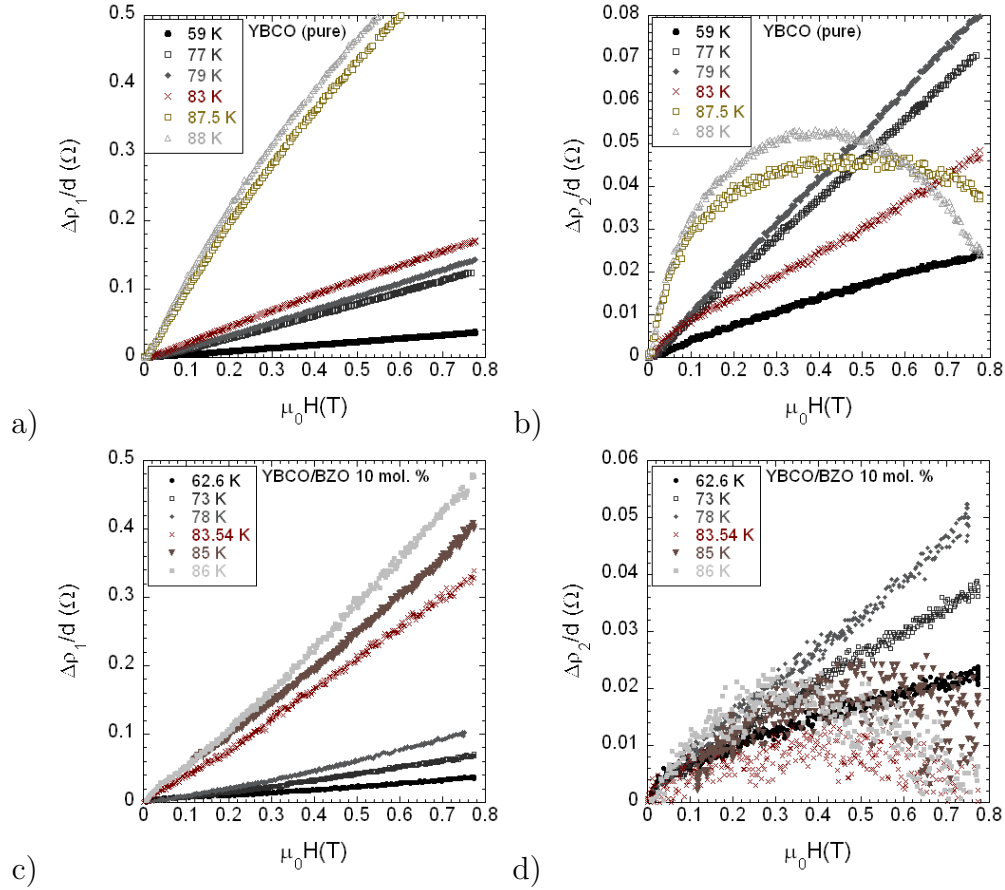
Figure 4.15: Magnetic field dependence of $\Delta\rho_1$ and $\Delta\rho_2$ of the a,b) pure YBCO and c,d) YBCO with 10% of BZO samples at T=60-90 K. It has to be noted that the different vertical scales for $\Delta\rho_1$ and $\Delta\rho_2$ indicate very weak pinning (small reactive signal)
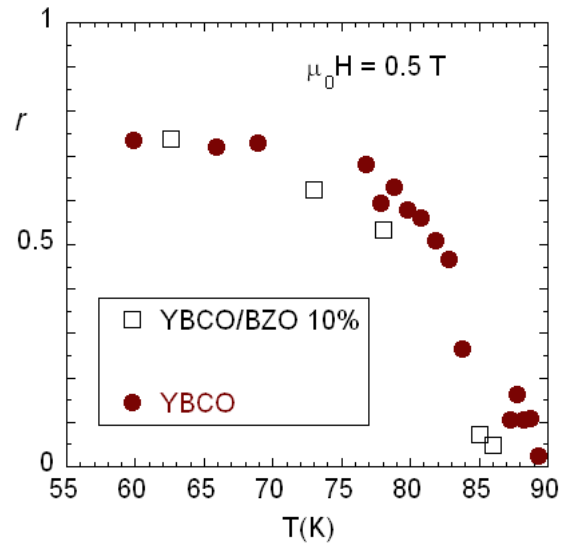
Figure 4.16: Temperature dependence of the pinning parameter of CSD YBCO and YBCO/BZO 10% samples at 0.5T

samples prepared with CSD technique the pinning caused by YBCO layered structure, which is indication of the point-like pinning centers. All obtained data are well agree with dc measurements.

Chapter 5

Conclusions

The goal of this thesis is the experimental study of the complex resistivity of nonconventional superconducting structures at microwave frequencies. Two kinds of structures were studied: first, a series of superconductor/ ferromagnetic/ superconductor (S/F/S) multilayers; second, high temperature superconductors with nanosize artificial pinning centres.

The experimental part included the development, setup and testing of new experimental systems or improvements of the performances of existing ones. Several resonance techniques for effective surface impedance measurements in thin superconducting films in presence of the external magnetic field were developed. A measuring cell based on a dielectric resonator, which operates at 8.3 GHz, was realized and tested at low temperature. The possibility of the superconductor parameter extraction from the raw data was shown. A 48-GHz dielectric resonator already operating for the reflection type measurements, was upgraded to operate in transmission. This gave a significant improvement to the measurement procedure. Finally, a new dielectric resonator in form of parallelepiped was designed and put into operation. Additional, a swept frequency Corbino disk setup was used to access the frequency dependence of the real part of the resistivity of the materials under study.

A series of S/F/S samples was measured, driven by the interest to the phenomena that occur due to the effect of the ferromagnet on superconductivity. $Nb/Pd_{0.81}Ni_{0.19}/Nb$ samples with different d_{PdNi} thickness (from 0 to 9 nm) with fixed thickness of S layer, d_S=15 nm, were prepared. The study of the crystal structure, performed by TEM and EXAFS (within a project at the ELETTRA Synchrotron Facility), showed the interdiffusion of the Pd atoms in the Nb layer. By EXAFS it was determined that the disorder in Nb layer is independent from the the thickness of ferromagnetic layer. The process of Pd-Nb interdiffusion depends on time, and it leads to the ageing effect, and to magnetic properties different from nominal.

In S/F/S, at zero magnetic field the losses and the effective penetration depth temperature dependencies (λ_{eff}(T)) were determined based on the complex resistivity measured by the 8.3-GHz dielectric resonator. The temperature dependencies of both losses and penetration depth exhibited a characteristic peak. This peak could not be interpreted as result of disordering, instead it could be an indication of so-called $0 - \pi$ thermally induced transition. In fact, the increase of the ferromagnetic layer thickness drives $\lambda_{eff}(T)$ away from the dependence described by BCS theory. However, for the sample with d_{PdNi}=2 nm above the reduced temperature $T/T_c \sim 0.78$ the Nb layers becomes coupled and $\lambda_{eff}(T)$ can be again described by BCS. This crossover is an additional indication of different coupling between superconducting layers for samples with different ferromagnetic layer thickness (0 and π states) and it is presently under active investigation. The ageing effect was also studied.

The main part of microwave measurements was performed in a dc magnetic field (up to H_{c2}), which was applied perpendicular to the sample surface. Measurements was taken with the 8.3-GHz dielectric resonator and by Corbino disk in the frequency interval 1-20 GHz. Experimental data, obtained by this two methods show good agreement and supplement each other. This gives the possibility of the precise measurements far from superconductor-normal transition and the possibility to obtain measurements also near it.

It was shown that microwave measurements allow to access the flux-flow resistivity ρ_{ff} at subcritical currents as well as other flux motion parameters. Then the study of ρ_{ff} field dependence of the sample with increasing ferromagnetic thickness d_F showed the progressive change from conventional behaviour (which can be described by time-dependent Ginzburg-Landau theory), to a new high-dissipative state. In this state ρ_{ff} exceeds the Bardeen-Stephen value $\rho_n H/H_{c2}$ in almost the entire field range. A quantitative explanation of the phenomenon is not given at present. Moreover, vortex pinning and vortex creep are heavily affected by thickness of F layer: pinning decreases and creep increases with increasing F thickness. The interesting result that structural disorder alone cannot explain the observed weakening of pinning and strengthening of creep (it is independent from d_F) points to a reduction of the superfluid as the origin of both effects

The last part of this work is connected to the study of the anisotropy in high temperature superconductors, namely, $YBa_2Cu_3O_{7-x}$ film samples with $BaZrO_3$ nano-inclusions were studied. $BaZrO_3$ inclusions form strongly oriented columnar defects in the $YBa_2Cu_3O_{7-x}$ film volume, which was confirmed by TEM study. Such nanorods are very efficient pinning centers, even if field is tilted from alignment with the nanorods. The samples, which were grown with pulsed laser deposition (PLD) and chemical solution decomposition (CSD)

techniques, contained 5 mol.% of BaZrO$_3$ and 10 mol.% of BaZrO$_3$ inclusions, respectively. To show the effect of BaZrO$_3$ the data were compared with pure YBa$_2$Cu$_3$O$_{7-x}$ samples.

Measurements of the field and angular dependence of the complex resistivity at 48 GHz were taken with μ_0H$\leq$0.8 T and T>65 K. The angular measurements of the genuine flux flow resistivity ρ_{ff} and pinning constant k$_p$ in YBa$_2$Cu$_3$O$_{7-x}$/BaZrO$_3$ (PLD) samples (obtained within a collaboration with ENEA-Frascati involving a FIRB project and EURATOM activity) was presented. To extract the measured quantity from the experimental data the universal expression was applied. By taking into account the variable Lorentz force in our experimental setup (due to the circular currents, induced by cylindrical DR mode), the correction based on the vortex motion model in anisotropic material was applied. It was shown that angular scaling takes place in flux-flow resistivity as intrinsic quantity related to the effective mass anisotropy. Opposite situation was observed in pinning coefficient and critical current, which are related to the pinning of fluxlines.

From the simultaneous study of the angular dependence of k$_p$ and J$_{c,dc}$ it was deduced that pinning is effective up to θ=65° of the magnetic field tilting. The pinning effect of BaZrO$_3$ dominates in the angular region θ=0°$-$65° which is characterized by the superposition of two regimes: strong core pinning and Mott insulator-like pinning, observed in dc. When magnetic field is parallel to the sample surface, the pinning due to the layered structure becomes dominant. At intermediate angles the interplay between the two sources of pinning exists and columnar BaZrO$_3$ structures operate as point-like pinning centers.

The study of the BaZrO$_3$ effect in CSD YBa$_2$Cu$_3$O$_{7-x}$/BaZrO$_3$ is relevant to the technological use of this superconductor. While dc measurements, which probes the height of the pinning well, showed an increase of the critical current with respect to the pure sample, with the microwave technique the steepness of the pinning well produced by BaZrO$_3$ was probed and no difference was found between the pure sample and YBa$_2$Cu$_3$O$_{7-x}$/BaZrO$_3$ (CSD). Thus, the combination of dc and microwave measurements unveil the different pinning nature in differently grown samples.

As a summary, I presented the comprehensive study of superconducting structures in microwaves both for the fundamental physics, in the case of S/F/S samples, and for technological applications, in case of the study of the pinning in YBa$_2$Cu$_3$O$_{7-x}$/BaZrO$_3$. I show, that microwave technique is a powerful tool for the investigation of the microscopical characteristics of the superconductors. The results, obtained for the study of the S/F/S samples stimulate of the interest of leading theorists as the base of the future theoretical models of the superconducting state . The investigation of the pinning in

$YBa_2Cu_3O_{7-x}$ with $BaZrO_3$ nanocolumns in microwaves determined the way to grow the coated conductors for the future realization in high magnetic field systems and fusion reactors.

Appendix A

12-term calibration approach

In order to determinate error coefficients, the 12-term model was applied. Initially S parameters of the Open, Short, Load and Thru standards must be determined from literature. Standards S parameters can be defined as:

$$\begin{cases} S_{11}^{open} = S_{22}^{open} = e^{-2i\beta l} e^{-2i\arctan(\omega C_{open}(\omega) Z_0)} \\ S_{11}^{short} = S_{22}^{short} = -e^{-2i\beta l} \\ S_{11}^{load} = S_{22}^{load} = 0 \end{cases} \qquad (A.0.1)$$

where $\beta = \omega\sqrt{\mu_0\varepsilon_0}$; l- length of the transmission line in the standard; $Z_0 = 50\Omega$; $C_{open}(\omega) = \sum_0^3 C_i\omega^i$ is the "open" standard capacitance (C_i - coefficients).

Then S parameters measurements of the standards connected to the line were performed. From such measurements one can extract 6 error coefficients: "Directivity" (E_D, $E_{D'}$), "Ports Match" (E_S,$E_{S'}$) and "Reflection Tracking" (E_{ST},$E_{ST'}$) coefficients in reverse and forward directions. This can be done by solving two following systems of linear equations:

$$\begin{pmatrix} 1 & S_{11}^{open} & -S_{11}^{open} \\ 1 & S_{11}^{short} & -S_{11}^{short} \\ 1 & S_{11}^{load} & -S_{11}^{load} \end{pmatrix} \cdot \begin{pmatrix} E_D \\ E_S \\ E_D E_S - E_{RT} \end{pmatrix} = \begin{pmatrix} S_{11,M}^{open} \\ S_{11,M}^{short} \\ S_{11,M}^{load} \end{pmatrix}$$

$$\begin{pmatrix} 1 & S_{22}^{open} & -S_{22}^{open} \\ 1 & S_{22}^{short} & -S_{22}^{short} \\ 1 & S_{22}^{load} & -S_{22}^{load} \end{pmatrix} \cdot \begin{pmatrix} E_{D'} \\ E_{S'} \\ E_{D'} E_{S'} - E_{RT'} \end{pmatrix} = \begin{pmatrix} S_{22,M}^{open} \\ S_{22,M}^{short} \\ S_{22,M}^{load} \end{pmatrix}$$

where $S_M^{<standard>}$ - measured S parameters of the connected standard.

From measurements with Load standard, connected to the each port the Leakage error coefficients can be determined as:

$$E_X = S_{21,M}; E_{X'} = S_{12,M} \qquad (A.0.2)$$

From measurements with Thru standard the Transmission Tracking (E_L,$E_{L'}$),

and Port-2 match $(E_{TT}, E_{TT'})$ error coefficients were obtained from equations:

$$\begin{cases} E_L = \frac{S_{11,M}-E_D}{S_{11,M}E_S-E_DE_S-E_{RT}} \\ E_{TT} = (S_{21,M}-E_X)(1-E_SE_L) \end{cases} and \begin{cases} E_{L'} = \frac{S_{22,M}-E_{D'}}{S_{11,M}E_S-E_DE_S-E_{RT}} \\ E_{TT'} = (S_{12,M}-E_{X'})(1-E_{S'}E_{L'}) \end{cases}$$

$$(A.0.3)$$

On the bases of the calibrated error coefficients, S parameters can be determined from equations:

$$S_{11} = \frac{a_1(1+a_2E_{S'})-E_La_3a_4}{(1+a_1E_S)(1+a_2E_{S'})-E_LE_{L'}a_3a_4} \tag{A.0.4}$$

$$S_{21} = \frac{a_3(1+a_2(E_{S'}-E_L))}{(1+a_1E_S)(1+a_2E_{S'})-E_LE_{L'}a_3a_4} \tag{A.0.5}$$

$$S_{12} = \frac{a_4(1+a_1(E_S-E_{L'}))}{(1+a_1E_S)(1+a_2E_{S'})-E_LE_{L'}a_3a_4} \tag{A.0.6}$$

$$S_{22} = \frac{a_2(1+a_1E_S)-E_{L'}a_3a_4}{(1+a_1E_S)(1+a_2E_{S'})-E_LE_{L'}a_3a_4} \tag{A.0.7}$$

where $a_1 = \frac{S_{11,M}-E_D}{E_{RT}}; a_2 = \frac{S_{22,M}-E_{D'}}{E_{RT'}}; a_3 = \frac{S_{21,M}-E_X}{E_{TT}}; a_4 = \frac{S_{12,M}-E_{X'}}{E_{TT'}}$

Appendix B

Modal fields of the dielectric resonator

In this appendix the electromagnetic structure represented in figure B.1 (along with its cylindrical coordinate system) is studied [70, 151]. It consists of an uniaxially anisotropic cylindrical dielectric rod ($r \leq a$, region 1) surrounded by air or vacuum ($a < r \leq b$, region 2) coaxially enclosed in a metallic case.
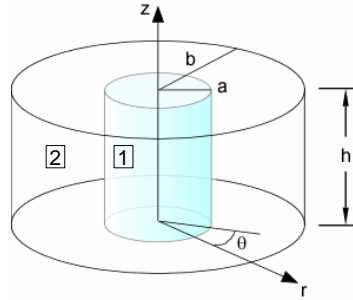
Figure B.1: Shielded dielectric resonator in cylindrical coordinate system.

The uni-axially anisotropic relative permittivity tensor is given by:

$$\bar{\bar{\varepsilon}}_r = \begin{bmatrix} \varepsilon_t & 0 & 0 \\ 0 & \varepsilon_t & 0 \\ 0 & 0 & \varepsilon_z \end{bmatrix} \tag{B.0.1}$$

and the anisotropy coefficient is defined as $\alpha = \varepsilon_z/\varepsilon_t$. The relative magnetic permeability of all the materials is assumed $\mu_r = 1$ and the conductors are assumed to be lossless. In the frequency domain, using the time-harmonic factor $e^{i\omega t}$, the source-free Maxwell equations in the dielectric are:

137

$$\nabla \times \mathbf{E} = -i\omega\mu_0\mathbf{H} \qquad (B.0.2)$$

$$\nabla \times \mathbf{H} = i\omega\varepsilon_0\bar{\bar{\varepsilon}}_r\mathbf{E} \qquad (B.0.3)$$

$$\nabla \cdot (\bar{\bar{\varepsilon}}_r\mathbf{E}) = 0 \qquad (B.0.4)$$

$$\nabla \cdot \mathbf{H} = 0 \qquad (B.0.5)$$

Equation (B.0.4) can be rewritten as:

$$\nabla \cdot \mathbf{E} = \left(1 - \frac{\varepsilon_z}{\varepsilon_t}\right)\frac{\partial E_z}{\partial z} \qquad (B.0.6)$$

Combining the Maxwell equations and using expression (B.0.6), one derives the following Helmholtz equations for the electric $\mathbf{E}$ and magnetic fields $\mathbf{H}$ inside the dielectric:

$$(\nabla \cdot \nabla)\mathbf{E} - \left(1 - \frac{\varepsilon_z}{\varepsilon_t}\right)\nabla\frac{\partial E_z}{\partial z} + k_0^2\bar{\bar{\varepsilon}}_r\mathbf{E} = 0 \qquad (B.0.7)$$

$$(\nabla \cdot \nabla)\mathbf{H} + i\omega\varepsilon_0\nabla \times (\bar{\bar{\varepsilon}}_r\mathbf{E}) = 0 \qquad (B.0.8)$$

Since all the electromagnetic field components can be derived once the z-components E_z and H_z are known, one can focus on them looking for the scalar equations which they must satisfy. Projecting the above expressions along the z direction and using the following identity derived from the first Maxwell equation:

$$\{\nabla \times (\bar{\bar{\varepsilon}}_r\mathbf{E})\}_z = -i\omega\varepsilon_0\varepsilon_t H_z \qquad (B.0.9)$$

one can write down the desired scalar (and decoupled) wave equations for the z-components of $\mathbf{E}$ and $\mathbf{H}$:

$$\nabla^2 E_z - \left(1 - \frac{\varepsilon_z}{\varepsilon_t}\right)\frac{\partial_2 E_z}{\partial z^2} + \varepsilon_z k_0^2 E_z = 0 \qquad (B.0.10)$$

$$\nabla^2 H_z + \varepsilon_t k_0^2 H_z = 0 \qquad (B.0.11)$$

where $k_0 = \omega\sqrt{\varepsilon_0\mu_0}$ is the vacuum wave number. In the region 2 of the resonator these same equations can be used with $\bar{\bar{\varepsilon}}_r = \bar{\bar{1}}$, being $\bar{\bar{1}}$ the unity matrix. Equations (B.0.10) and (B.0.11) are solved together with the boundary conditions on the conducting walls (upper and lower plates and lateral wall),

giving the following quantities (subscripts 1 and 2 denote quantities in region 1, dielectric, and region 2, air, respectively):

$$E_{z1} = Ak_{e1}^2 J_m(k_{e1}r)\cos m\theta \cos \beta z \tag{B.0.12}$$

$$H_{z1} = Bk_{h1}^2 J_m(k_{h1}r)\sin m\theta \sin \beta z \tag{B.0.13}$$

in region 1 with $0 \le r \le a$, and

$$E_{z2} = k_2^2 C P_{E,m}(k_2 r)\cos m\theta \cos \beta z \tag{B.0.14}$$

$$H_{z2} = k_2^2 D P_{H,m}(k_2 r)\sin m\theta \sin \beta z \tag{B.0.15}$$

in region 2 with $a < r \le b$. In the above equations:

$$k_{e1}^2 = \varepsilon_z k_0^2 - \frac{\varepsilon_z}{\varepsilon_t}\beta^2 = \alpha k_{h1}^2 \tag{B.0.16}$$

$$k_{h1}^2 = \varepsilon_t k_0^2 - \beta^2 \tag{B.0.17}$$

$$k_2^2 = \beta^2 - k_0^2 \tag{B.0.18}$$

$$\beta = \frac{p\pi}{h} \tag{B.0.19}$$

$$k_0 = \omega_0\sqrt{\varepsilon_0 \mu_0} = \frac{2\pi\nu_0}{c} \tag{B.0.20}$$

$$P_{E,m} = K_m(k_2 r) - \frac{K_m(k_2 b)}{I_m(k_2 b)}I_m(k_2 r) \tag{B.0.21}$$

$$P_{H,m} = K_m(k_2 r) - \frac{K_m'(k_2 b)}{I_m'(k_2 b)}I_m(k_2 r) \tag{B.0.22}$$

where the vacuum wave number k_0 is now evaluated at the resonant frequency $\nu_0 = \omega_0/(2\pi)$, and $c = 1/\sqrt{\mu_0\varepsilon_0}$ is the speed of light. A, B, C and D are mode constants determined (apart an overall scale factor defining the absolute intensity of the electromagnetic fields) by the boundary conditions at the dielectric/vacuum interface; m, n, and p are the mode numbers in the azimuthal, radial and axial directions, respectively; $J_m(x)$, $I_m(x)$ and $K_m(x)$ are the Bessel function of the first kind, modified Bessel functions of the first and second kind, respectively; the primes on the Bessel functions and on the $P_{E|H,m}(x)$ functions denote a differentiation with respect their argument x. All the remaining field components are obtained through the following:

$$
\begin{aligned}
E_r &= -i\omega\mu_0 \frac{1}{k_h^2}\frac{1}{r}\frac{\partial H_z}{\partial\theta} + \frac{\varepsilon_z}{\varepsilon_t}\frac{1}{k_e^2}\frac{\partial^2 E_z}{\partial r\partial z} \\[2mm]
E_\theta &= i\omega\mu_0 \frac{1}{k_h^2}\frac{\partial H_z}{\partial r} + \frac{\varepsilon_z}{\varepsilon_t}\frac{1}{k_e^2}\frac{1}{r}\frac{\partial^2 E_z}{\partial\theta\partial z} \\[2mm]
H_r &= \frac{1}{k_h^2}\frac{\partial^2 H_z}{\partial r\partial z} + i\omega\varepsilon_0\varepsilon_z\frac{1}{k_e^2}\frac{1}{r}\frac{\partial E_z}{\partial\theta} \\[2mm]
H_\theta &= \frac{1}{k_h^2}\frac{1}{r}\frac{\partial^2 H_z}{\partial\theta\partial z} - i\omega\varepsilon_0\varepsilon_z\frac{1}{k_e^2}\frac{\partial E_z}{\partial r}
\end{aligned}
\tag{B.0.23}
$$

The continuity condition for the tangential components of the fields at the dielectric/vacuum interface requires that $E_{z1} = E_{z2}$, $H_{z1} = H_{z2}$, $E_{\theta 1} = E_{\theta 2}$, $H_{\theta 1} = H_{\theta 2}$, which give an homogeneous linear system which has non-trivial solutions for A, B, C, D if its coefficient matrix determinant is non zero. This condition is verified for the solutions, in terms of resonant frequency ν_0, of the following characteristic equation:

$$
F_1 F_2 - F_3^2 = 0 \tag{B.0.24}
$$

with

$$
\begin{aligned}
F_1 &= \varepsilon_z \frac{J_n'(x_e)}{x_e J_n(x_e)} + \frac{P_{E,n}'(y)}{y P_{E,n}(y)} \\[2mm]
F_2 &= \frac{J_n'(x_h)}{x_h J_n(x_h)} + \frac{P_{H,n}'(y)}{y P_{H,n}(y)} \\[2mm]
F_3 &= \frac{m\beta}{k_0}\left(\frac{1}{x_h^2} + \frac{1}{y^2}\right)
\end{aligned}
\tag{B.0.25}
$$

where $x_e = k_{e1}a$, $x_h = k_{h1}a$ and $y = k_2 a$. In particular, the characteristic equation for TE_{0np} is $F_2 = 0$; for TM_{0np} and TM_{mn0} it is $F_1 = 0$ and for the hybrid modes HEM_{mnp} with $n \geq 1$ it is the full expression $F_1 F_2 - F_3^2 = 0$.

I now particularize for the case of the TE_{011} mode, writing down the full field expressions and the the figures of merit of the dielectric resonator used in this work. The field expressions are derived from (B.0.12), (B.0.14) and (B.0.23) giving the following:

$$
\begin{aligned}
H_{z1} &= H_0 J_0(k_h r)\sin\beta z \\
H_{z2} &= H_0 \frac{J_0(k_h a)}{P_{H,0}(k_2 a)} P_{H,0}(k_2 r)\sin\beta z \\
E_{\theta 1} &= -H_0 \frac{i\omega\mu_0}{k_h} J_1(k_h r)\sin\beta z \\
E_{\theta 2} &= -H_0 \frac{i\omega\mu_0}{k_h} \frac{J_1(k_h a)}{P'_{H,0}(k_2 a)} P'_{H,0}(k_2 r)\sin\beta z \quad\quad \text{(B.0.26)} \\
H_{r1} &= -H_0 \frac{\beta}{k_h} J_0(k_h r)\cos\beta z \\
H_{r2} &= -H_0 \frac{\beta}{k_h} \frac{J_0(k_h a)}{P_{H,0}(k_2 a)} P_{H,0}(k_2 r)\cos\beta z \\
E_z &= E_r = 0, \ H_\theta = 0
\end{aligned}
$$

where H_0 is a re-defined overall scale factor.

The amounts of electric energy stored in regions 1 and 2, which are required to compute η and therefore Q_d, are:

$$
\begin{aligned}
W_{e1} &= \frac{\varepsilon_t \varepsilon_0 \pi}{8} h a^2 |H_0|^2 \text{IntJ} \\
W_{e2} &= \frac{\varepsilon_0 \pi}{8} h a^2 |H_0|^2 \text{IntP} \quad\quad\quad\quad\quad\quad\quad\quad \text{(B.0.27)} \\
\text{IntJ} &= J_0(x_h)^2 - \frac{2}{x_h} J_0(x_h) J_1(x_h) + J_1^2(x_h) \\
\text{IntP} &= \left[\frac{J_1(x_h)}{P'_{H,0}(y)}\right]^2 \left[P_{H,0}^2(y) - \frac{2}{y} P_{H,0}(y) P'_{H,0}(y) - P'^2_{H,0}(y) - \left(y\frac{b}{a}\right)^2 P_{H,0}^2\left(y\frac{b}{a}\right)\right]
\end{aligned}
$$

The geometric factors G_{base} and G_{lat}, respectively for one base and for the lateral walls, are:

$$
\begin{aligned}
G_{base} &= 4\pi Z_0 \left(\frac{\nu_0 h}{c}\right)^3 \frac{\varepsilon_t \text{IntJ} + \text{IntP}}{\text{IntJ} + \text{IntP}} \quad\quad\quad\quad \text{(B.0.28)} \\
G_{lat} &= 4\pi^3 Z_0 \left(\frac{\nu_0}{c}\right)^3 \frac{a^4}{b} \frac{1}{y^2} \frac{\varepsilon_t \text{IntJ} + \text{IntP}}{\left(\frac{J_1(x_h)}{P'_{H,0}(y)}\right)^2 P_{H,0}^2(yb/a)} \quad\quad \text{(B.0.29)}
\end{aligned}
$$

with $Z_0 = \sqrt{\mu_0/\varepsilon_0}$ being the vacuum characteristic impedance. Last, the overall geometric factor is computed as $G_0^{-1} = 2G_{base}^{-1} + G_{lat}^{-1}$.

Appendix C

Rectangular DR

Main part of the losses in the metal covered dielectric resonator this is losses in the covering conductors. In [85, 87] the electromagnetic model of RDR was created for the filter application. For the resonator which can be represented as section of the metal rectangular waveguide of the length d filled by dielectric the $TE_{01\delta}$ mode is characterized by the shifting of the perfect magnetic wall from the open boundary to the center of the resonator.
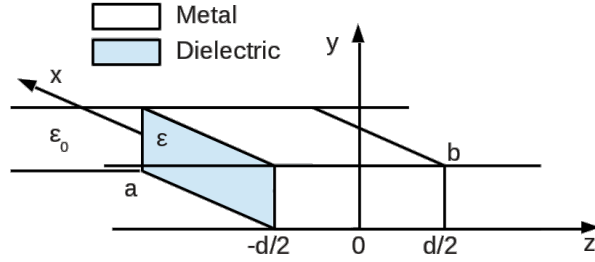
Figure C.1: Coordinate system for RDR.

Model of the field distribution can be obtained by assuming that this resonator is extended with empty (air-filled) infinite waveguide. The draft of this structure is shown in Fig. C.1. To define the field distribution in the partially filed waveguide, last can be represented as The field distributions in the section of RDR can be represented based on the solution of the wave equations. Fort the region inside the dielectric region $(-d/2 \leq z \leq d/2)$ the electric and magnetic field distribution is represented as [85, 81]

$$E_y = E_0 \sin \frac{\pi x}{a} \cos \beta z \qquad (C.0.1)$$

$$H_x = -j \frac{E_0 \beta}{\omega \mu} \sin \frac{\pi x}{a} \sin \beta z \qquad (C.0.2)$$

$$H_z = j\frac{E_0}{\omega\mu}\left(\frac{\pi}{a}\right)\cos\frac{\pi x}{a}\cos\beta z \tag{C.0.3}$$

for the region of the $z < -d/2$ and $z > d/2$

$$E'_y = E_0 \sin\frac{\pi x}{a}\cos\frac{\beta d}{2}e^{\gamma(z-d/2)} \tag{C.0.4}$$

$$E'_x = j\frac{E_0\gamma}{\omega\mu}\sin\frac{\pi x}{a}\cos\frac{\beta d}{2}e^{-\gamma(z-d/2)} \tag{C.0.5}$$

$$H'_z = j\frac{E_0}{\omega\mu}\left(\frac{\pi}{a}\right)\cos\frac{\pi x}{a}\cos\frac{\beta d}{2}e^{-\gamma(z-d/2)} \tag{C.0.6}$$

where
$\gamma^2 = K^2 - K_c^2,\ \beta^2 = K_c^2 - \omega_0^2\varepsilon_0\mu_0,$

$K_c^2 = (\pi m/a)^2 + (\pi m/a)^2,\ K^2 = \omega_0^2\varepsilon_0\varepsilon_r\mu_0,$

$\varepsilon = \varepsilon_0\varepsilon_r,\ \mu = \mu_0\mu_r$ are relative permittivity and permeability of the dielectric material.

The Q-factor of this resonator is represented as ratio between the total energy stored within the dielectric filled waveguide W with energy stored within the empty waveguide W' and losses in the elements of the structure

Amount of the stored energy within the dielectric is:

$$P_e = \frac{\varepsilon}{4}\int_v E_y \cdot E_y^* dv = \varepsilon\frac{ab}{16}E_0^2\left(d + \frac{\sin\beta d}{\beta}\right) \tag{C.0.7}$$

$$P_m = \frac{\mu}{4}\int_v (H_x \cdot H_x^* + H_z \cdot H_z^*)dv = \frac{\varepsilon E_0^2}{16}ab\left(d + \frac{K_c^2 - \beta^2}{K^2}\frac{\sin\beta d}{\beta}\right) \tag{C.0.8}$$

in the air filled waveguide:

$$P'_e = 2\cdot\frac{\varepsilon_0}{4}\int_{v'} E'_y E'^*_y dv' = \frac{\varepsilon_0}{\alpha}\frac{ab}{8}E_0^2\cos^2\frac{\beta d}{2} \tag{C.0.9}$$

$$P'_m = 2\cdot\frac{\mu}{4}\int_{v'}\left(H'_x \cdot H'^*_x + H'_z \cdot H'^*_z\right)dv' =$$
$$= \frac{\mu}{\alpha}\frac{ab}{8}E_0^2\left[\left(\frac{\alpha}{\omega\mu}\right)^2\sin^2\frac{\beta d}{2} + \left(\frac{K_c}{\omega\mu}\right)^2\cos^2\frac{\beta d}{2}\right] \tag{C.0.10}$$

Resulting total stored energy is the sum of all this terms:

$$P_{EM} = P_e + P'_e + P_m + P'_m = \frac{R_s}{2} \int_s J_s J_s^* ds =$$

$$= \varepsilon \frac{ab}{8} E_0^2 \left[d + \frac{\alpha}{K^2} + \frac{1 + \cos\beta d}{\varepsilon_r \alpha} + \left(\frac{K_c}{K}\right)^2 \frac{\sin\beta d}{\beta} \right] \qquad \text{(C.0.11)}$$

The losses in the conductive parts can be rewritten as:

$$P_c = \frac{\omega R_s}{4\sqrt{\mu/\varepsilon}} \left[\left(\frac{K_c}{K}\right)^2 \left(b + \frac{a}{2}\right)\left(d + \frac{\sin\beta z}{\beta}\right) + \left(\frac{\beta}{K}\right)^2 \frac{a}{2}\left(d - \frac{\sin\beta z}{\beta}\right) \right]$$
$$\text{(C.0.12)}$$

In result conductive parts Q-factor is:

$$Q_C = \frac{\omega_0 P_{EM}}{P_c} \qquad \text{(C.0.13)}$$

where $R_s = \sqrt{\omega\mu/2\sigma}$ is the surface impedance of the waveguide walls.

Dielectric losses can be determined with simple relation: $Q_d = 1/\tan\delta$, where $\tan\delta = \varepsilon/\varepsilon'$ is the loss tangent of the dielectric material.

The characteristic equations have to be solved to determine TE_{mnp} and TH_{mnp} modes resonant frequency. In this representation the waveguide is characterized by finite length $L \gg l$. For TE_{mnp} modes in the waveguide section filled by dielectric, where the rectangular dielectric placed in the center and fills the whole cross-section, one can define the characteristic equation in the following form [86]:

$$\sqrt{\frac{\varepsilon_r - \frac{\lambda}{\lambda_{cr}(m,n)}}{1 - \frac{\lambda}{\lambda_{cr}(m,n)}}} \tan\left[\left(1 - \frac{\lambda}{\lambda_{cr}(m,n)}\right)L\right] = \begin{cases} \cot\left[\left(\varepsilon_r - \frac{\lambda}{\lambda_{cr}(m,n)}\right)l/2\right] \\ -\tan\left[\left(\varepsilon_r - \frac{\lambda}{\lambda_{cr}(m,n)}\right)l/2\right] \end{cases}$$
$$\text{(C.0.14)}$$

For TH_{mnp} it is represented as:

$$\varepsilon_r \sqrt{\frac{1 - \frac{\lambda}{\lambda_{cr}(m,n)}}{\varepsilon_r - \frac{\lambda}{\lambda_{cr}(m,n)}}} \cot\left[\left(1 - \frac{\lambda}{\lambda_{cr}(m,n)}\right)L\right] = \begin{cases} \tan\left[\left(\varepsilon_r - \frac{\lambda}{\lambda_{cr}(m,n)}\right)l/2\right] \\ \cot\left[\left(\varepsilon_r - \frac{\lambda}{\lambda_{cr}(m,n)}\right)l/2\right] \end{cases}$$
$$\text{(C.0.15)}$$

where a, b and $l \ll L$ are sides of the dielectric parallelepiped; $\lambda_{cr}(m, n)$ is the cutoff wavelength of the waveguide without dielectric. Upper and lower right-side relations in the brackets correspond to the non-even modes (p=2N+1, where N=0,1,2...) and even modes (p=2N, where N=0,1,2...).

Bibliography

[1] H. Onnes. The superconductivity of mercury. *Comm. Phys. Lab. Univ. Leiden*, 122, 1911.

[2] W. Meissner and R Ochsenfeld. Ein neuer effekt bei eintritt der supraleitfhigkeit. *Naturwissenschaften*, 21:787, 1933.

[3] Ruslan Prozorov and Russell W Giannetta. Magnetic penetration depth in unconventional superconductors. *Superconductor Science and Technology*, 19(8):R41, 2006.

[4] C.J Gorter and H Casimir. On supraconductivity i. *Physica*, 1(1-6):306 – 320, 1934.

[5] V.V. Schmidt. *The Physics of Superconductors: Introduction to Fundamentals and Applications*. Springer, 2002.

[6] Charles P. Poole Jr., Horacio A. Farach, Richard J. Creswick, and Ruslan Prozorov. *Superconductivity, Second Edition*. Academic Press, 2007.

[7] J. Bardeen, L. N. Cooper, and J. R. Schrieffer. Theory of superconductivity. *Phys. Rev.*, 108:1175–1204, Dec 1957.

[8] Leon N. Cooper. Bound electron pairs in a degenerate fermi gas. *Phys. Rev.*, 104:1189–1190, Nov 1956.

[9] A.A. Abrikosov. *Fundamentals of the Theory of Metals*. North Holland, 1988.

[10] Michael Tinkham. *Introduction to Superconductivity: Second Edition*. Dover Publications, 2004.

[11] Matthias Hein. *High-Temperature-Superconductor Thin Films at Microwave Frequencies (Springer Tracts in Modern Physics)*. Springer, 1999.

[12] L. Pitaevskii. Phenomenology and microscopic theory: Theoretical foundations. In K.H. Bennemann and JohnB. Ketterson, editors, *Superconductivity*, pages 27–71. Springer Berlin Heidelberg, 2008.

[13] G. Blatter and V.B. Geshkenbein. Vortex matter. In K.H. Bennemann and JohnB. Ketterson, editors, *Superconductivity*, pages 495–637. Springer Berlin Heidelberg, 2008.

[14] G. Blatter, M. V. Feigel'man, V. B. Geshkenbein, A. I. Larkin, and V. M. Vinokur. Vortices in high-temperature superconductors. *Rev. Mod. Phys.*, 66:1125–1388, Oct 1994.

[15] G. Blatter, V. B. Geshkenbein, and A. I. Larkin. From isotropic to anisotropic superconductors: A scaling approach. *Phys. Rev. Lett.*, 68:875–878, Feb 1992.

[16] N B Kopnin. Vortex dynamics and mutual friction in superconductors and Fermi superfluids. *Reports on Progress in Physics*, 65(11):1633, 2002.

[17] John Bardeen and M. J. Stephen. Theory of the Motion of Vortices in Superconductors. *Phys. Rev.*, 140:A1197–A1207, Nov 1965.

[18] John Bardeen and M. J. Stephen. Theory of the Motion of Vortices in Superconductors. *Phys. Rev.*, 140:A1197–A1207, Nov 1965.

[19] M Golosovsky, M Tsindlekht, and D Davidov. High-frequency vortex dynamics in $YBa_2Cu_3O_{7-\delta}$. *Superconductor Science and Technology*, 9(1):1, 1996.

[20] C. Caroli, P.G. De Gennes, and J. Matricon. Bound Fermion states on a vortex line in a type-II superconductor. *Physics Letters*, 9(4):307 – 309, 1964.

[21] P. W. Anderson. Theory of Flux Creep in Hard Superconductors. *Phys. Rev. Lett.*, 9:309–311, Oct 1962.

[22] Jonathan I. Gittleman and Bruce Rosenblum. Radio-Frequency Resistance in the Mixed State for Subcritical Currents. *Phys. Rev. Lett.*, 16:734–736, Apr 1966.

[23] Mark W. Coffey and John R. Clem. Theory of rf magnetic permeability of isotropic type-II superconductors in a parallel field. *Phys. Rev. B*, 45:9872–9881, May 1992.

[24] Mark W. Coffey and John R. Clem. Unified theory of effects of vortex pinning and flux creep upon the rf surface impedance of type-II superconductors. *Phys. Rev. Lett.*, 67:386–389, Jul 1991.

[25] E H Brandt. Linear a.c. response of high- T c superconductors and the irreversibility line. *Physica Scripta*, 1992(T45):63, 1992.

[26] Ernst Helmut Brandt. Penetration of magnetic ac fields into type-II superconductors. *Phys. Rev. Lett.*, 67:2219–2222, Oct 1991.

[27] N. Pompeo and E. Silva. Reliable determination of vortex parameters from measurements of the microwave complex resistivity. *Phys. Rev. B*, 78:094503, Sep 2008.

[28] J. Halbritter. rf residual losses, surface impedance, and granularity in superconducting cuprates. *Journal of Applied Physics*, 68(12):6315–6326, 1990.

[29] Yoshishige Tsuchiya, Katsuya Iwaya, Kentarou Kinoshita, Tetsuo Hanaguri, Haruhisa Kitano, Atsutaka Maeda, Kenji Shibata, Terukazu Nishizaki, and Norio Kobayashi. Electronic state of vortices in $YBa_2Cu_3O_y$ investigated by complex surface impedance measurements. *Phys. Rev. B*, 63:184517, Apr 2001.

[30] A.M. Campbell and J.E. Evetts. Flux vortices and transport currents in type II superconductors. *Advances in Physics*, 21(90):199–428, 1972.

[31] N. Pompeo, R. Marcon, and E. Silva. Dielectric Resonators for the Measurement of Superconductor Thin Films Surface Impedance in Magnetic Fields at High Microwave Frequencies. *Journal of Superconductivity and Novel Magnetism*, 20:71–82, 2007.

[32] Robert E. Collin. *Foundations for Microwave Engineering - 2nd edition.* Wiley-IEEE Press, 2000.

[33] N. Klein, H. Chaloupka, G. Muller, S. Orbach, H. Piel, B. Roas, L. Schultz, U. Klein, and M. Peiniger. The effective microwave surface impedance of high T_c thin films. *Journal of Applied Physics*, 67(11):6940–6945, 1990.

[34] N Pompeo, L Muzzi, V Galluzzi, R Marcon, and E Silva. Measurements and removal of substrate effects on the microwave surface impedance of YBCO films on $SrTiO_3$. *Superconductor Science and Technology*, 20(10):1002, 2007.

[35] T.M.P. Percival, J.S. Thorn, and R. Driver. Measurements of high-Tc superconductivity in a microwave cavity. *Electronics Letters*, 23(23):1225 –1226, 5 1987.

[36] R. Marcon, E. Silva, R. Fastampa, M. Giura, and S. Sarti. Angular scaling of the microwave magnetodissipation in $Bi_2Sr_2CaCu_2O_{8+x}$. *Phys. Rev. B*, 50:13684–13687, Nov 1994.

[37] D.N. Peligrad, M. Mehring, and A. Dulćić. Critical fluctuations and pseudogap observed in the microwave conductivity of $Bi_2Sr_2CaCu_2O_{8+\delta}$, $Bi_2Sr_2Ca_2Cu_3O_{10+\delta}$, and $YBa_2Cu_3O_{7-\delta}$ thin films. *Phys. Rev. B*, 69:144516, Apr 2004.

[38] B. Mayer, A. Reccius, and R. Knochel. Conical cavity for surface resistance measurements of high temperature superconductors. *Microwave Theory and Techniques, IEEE Transactions on*, 40(2):228 –236, feb 1992.

[39] S. Sridhar. Microwave response of thin-film superconductors. *Journal of Applied Physics*, 63(1):159–166, 1988.

[40] N. Klein, U. Poppe, N. Tellmann, H. Schulz, W. Evers, U. Dahne, and K. Urban. Microwave surface resistance of epitaxial YBa$_2$Cu$_3$O$_{7-x}$films: studies on oxygen deficiency and disordering. *Applied Superconductivity, IEEE Transactions on*, 3(1):1102 –1109, mar 1993.

[41] M. A. Hein, M. Strupp, H. Piel, A. M. Portis, and R. Gross. Surface impedance of YBa$_2$Cu$_3$O$_{7-x}$ thin film grain boundary Josephson junctions: Evaluation of the I$_{cRn}$ product. *Journal of Applied Physics*, 75(9):4581–4587, 1994.

[42] E Silva, A Lezzerini, M Lanucara, S Sarti, and R Marcon. A cavity system for the measurement of the surface resistance at 48 GHz in high-T$_c$ superconductors. *Measurement Science and Technology*, 9(2):275, 1998.

[43] A.M. Portis, D.W. Cooke, and E.R. Gray. RF properties of high-temperature superconductors: Cavity methods. *Journal of Superconductivity*, 3:297–304, 1990.

[44] M. R. Trunin. Conductivity anisotropy and pseudogap in the microwave response of high-Tc superconductors. *Physics-Uspekhi*, 48(10):979, 2005.

[45] A.F. Shevchun and M.R. Trunin. A method for measuring the surface impedance of superconductors in the temperature range 0.4-120 K. *Instruments and Experimental Techniques*, 49:669–675, 2006.

[46] C. Wilker, Z.-Y. Shen, P. Pang, D.W. Face, W.L. Holstein, A.L. Matthews, and D.B. Laubacher. 5 GHz high-temperature-superconductor resonators with high Q and low power dependence up to 90 K. *Microwave Theory and Techniques, IEEE Transactions on*, 39(9):1462 –1467, sep 1991.

[47] Y. Kobayashi and S. Tanaka. Resonant Modes of a Dielectric Rod Resonator Short-Circuited at Both Ends by Parallel Conducting Plates. *Microwave Theory and Techniques, IEEE Transactions on*, 28(10):1077 – 1085, oct 1980.

[48] B.W. Hakki and P.D. Coleman. A Dielectric Resonator Method of Measuring Inductive Capacities in the Millimeter Range. *Microwave Theory and Techniques, IRE Transactions on*, 8(4):402 –410, july 1960.

[49] S.J. Fiedziuszko and P.D. Heidmann. Dielectric resonator used as a probe for high-Tc superconductor measurements. In *Microwave Symposium Digest, 1989., IEEE MTT-S International*, pages 555 –558 vol.2, jun 1989.

[50] C. Wilker, Z.-Y. Shen, V.X. Nguyen, and M.S. Brenner. A sapphire resonator for microwave characterization of superconducting thin films. *Applied Superconductivity, IEEE Transactions on*, 3(1):1457 –1460, mar 1993.

[51] J. Krupka, M. Klinger, M. Kuhn, A. Baryanyak, M. Stiller, J. Hinken, and J. Modelski. Surface resistance measurements of HTS films by means of sapphire dielectric resonators. *Applied Superconductivity, IEEE Transactions on*, 3(3):3043 –3048, sep 1993.

[52] S.Y. Lee and B. Oh. Recent Progress in Microwave HTS Technologies in Korea and Japan. *Journal of Superconductivity*, 16:823–831, 2003.

[53] Y. Kobayashi and T. Hashimoto. Design of an image-type dielectric resonator to measure surface resistance of a high-Tc superconductor film. In *Microwave Symposium Digest, 2001 IEEE MTT-S International*, volume 1, pages 495 –498 vol.1, 2001.

[54] A. Andreone, A. Cassinese, L. Gianni, M. Iavarone, F. Palomba, and R. Vaglio. Superconducting gap anisotropy of $LuNi_2B_2C$ thin films from microwave surface impedance measurements. *Phys. Rev. B*, 64:100505, Aug 2001.

[55] S.B. Cohn. Microwave Bandpass Filters Containing High-Q Dielectric Resonators. *Microwave Theory and Techniques, IEEE Transactions on*, 16(4):218 – 227, apr 1968.

[56] Y. Kobayashi, T. Aoki, and Y. Kabe. Influence of Conductor Shields on the Q-Factors of a TE 0 Dielectric Resonator. *Microwave Theory and Techniques, IEEE Transactions on*, 33(12):1361 – 1366, dec 1985.

[57] D.P. Choudhury, B.A. Willemsen, J.S. Derov, and S. Sridhar. Nonlinear response of HTSC thin film microwave resonators in an applied DC magnetic field. *Applied Superconductivity, IEEE Transactions on*, 7(2):1260 –1263, jun 1997.

[58] A. Porch, M.J. Lancaster, and R.G. Humphreys. The coplanar resonator technique for determining the surface impedance of $YBa_2Cu_3O_{7-\delta}$; thin films. *Microwave Theory and Techniques, IEEE Transactions on*, 43(2):306 –314, feb 1995.

[59] G Ghigo, D Botta, A Chiodoni, R Gerbaldo, L Gozzelino, F Laviano, B Minetti, E Mezzetti, and D Andreone. Microwave dissipation in YBCO coplanar resonators with uniform and non-uniform columnar defect distribution. *Superconductor Science and Technology*, 17(8):977, 2004.

[60] A. Vakaliuk, A. Kalenyuk, O. Prokopenko, and V. Pan. Impedance determination of high-temperature superconductor film by combined microstrip resonator. In *Physics and Engineering of Microwaves, Millimeter and Submillimeter Waves (MSMW), 2010 International Kharkov Symposium on*, page 1, june 2010.

[61] C. Bilzer, T. Devolder, P. Crozat, C. Chappert, S. Cardoso, and P. P. Freitas. Vector network analyzer ferromagnetic resonance of thin films on coplanar waveguides: Comparison of different evaluation methods. *Journal of Applied Physics*, 101(7):074505, 2007.

[62] E. Kawate, R. Mossavati, M. Okaji, T. Ito, Y. Ohashi, A.M. Moe, and K. Oka. Surface impedance measurements on high-Tc superconductors using a far-infrared laser. *Applied Superconductivity, IEEE Transactions on*, 7(2):1853 –1856, jun 1997.

[63] R. E. Glover and M. Tinkham. Conductivity of Superconducting Films for Photon Energies between 0.3 and $40kT_c$. *Phys. Rev.*, 108:243–256, Oct 1957.

[64] J Ceremuga-Mazierska. Transmission of microwave signals through superconducting thin films in waveguides. *Superconductor Science and Technology*, 5(6):391, 1992.

[65] A.I. Gubin, N.T. Cherpak, and A.A. Lavrinovich. MM Wave Conductivity Measurement Technique by Grazing Incidence Reflectivity. In *Microwave Conference, 2008. EuMC 2008. 38th European*, pages 1074 –1077, oct. 2008.

[66] A. I. Gubin, A. A. Lavrinovich, and N. T. Cherpak. Microwave-Band Reflection Coefficient of High-Temperature Superconductor Specimens in E-Plane Waveguide Structures. *Technical Physics Letters*, 27:336–337, apr 2001.

[67] O.M. Corbino. Azioni Elettromagnetiche Doyute Agli Ioni dei Metalli Deviati Dalla Traiettoria Normale per Effetto di un Campo. *Il Nuovo Cimento*, 1:397–420, 1911.

[68] N. Tosoratti, R. Fastampa, M. Giura, V. Lenzi, S. Sarti, and E. Silva. Two techniques for broadband measurement of the surface impedance of high critical temperature superconducting thin films. *International Journal of Modern Physics B*, 14(25-27):2926–2931, 2000.

[69] Carl T. A. Johnk. *Engineering Electromagnetic Fields and Waves*. John Wiley & Sons, 1988.

[70] Darko Kajfez and Pierre Guillon. *Dielectric Resonators*. SciTech Publishing, 1998.

[71] K. Leong and J. Mazierska. Precise measurements of the Q factor of dielectric resonators in the transmission mode-accounting for noise, crosstalk, delay of uncalibrated lines, coupling loss, and coupling reactance. *Microwave Theory and Techniques, IEEE Transactions on*, 50(9):2115 – 2127, sep 2002.

[72] D. Kajfez and E.J. Hwan. Q-Factor Measurement with Network Analyzer. *Microwave Theory and Techniques, IEEE Transactions on*, 32(7):666 – 670, jul 1984.

[73] D. Kajfez. Deembedding of lossy foster networks. *Microwave Theory and Techniques, IEEE Transactions on*, 53(10):3199 – 3205, oct. 2005.

[74] N.T. Cherpak, A.A. Barannik, S.A. Bunyaev, Y.V. Prokopenko, and S.A. Vitusevich. Measurements of millimeter-wave surface resistance and temperature dependence of reactance of thin HTS films using quasi-optical dielectric resonator. *Applied Superconductivity, IEEE Transactions on*, 15(2):2919 – 2922, june 2005.

[75] N. Klein, C. Zuccaro, U. Dahne, H. Schulz, N. Tellmann, R. Kutzner, A. G. Zaitsev, and R. Wordenweber. Dielectric properties of rutile and its use in high temperature superconducting resonators. *Journal of Applied Physics*, 78(11):6683–6686, 1995.

[76] N. Pompeo. *Microwave complex response in superconducting thin films in magnetic fields*. Phd thesis, Università degli Studi Roma Tre, 2005.

[77] Doug Rytting. Overview of high power and large signal measurements and calibration. In *ARFTG Conference Digest-Spring, 47th*, volume 29, pages 76 –84, june 1996.

[78] D. Kajfez, W.P. Wheless, and R.T. Ward. Influence of an airgap on the measurement of dielectric constant by a parallel-plate dielectric resonator. *Microwaves, Antennas and Propagation, IEE Proceedings H*, 133(4):253 –258, august 1986.

[79] L. J. Broutman, S. M. Krishnakumar, and P. K. Mallick. Effects of combined stresses on fracture of alumina and graphite. *Journal of the American Ceramic Society*, 53(12):649–654, 1970.

[80] N. Pompeo, R. Marcon, and E. Silva. Dielectric Resonators for the Measurement of Superconductor Thin Films Surface Impedance in Magnetic Fields at High Microwave Frequencies. *Journal of Superconductivity and Novel Magnetism*, 20:71–82, 2007.

[81] R.K. Mongia. Theoretical and experimental resonant frequencies of rectangular dielectric resonators. *Microwaves, Antennas and Propagation, IEE Proceedings H*, 139(1):98 –104, feb 1992.

[82] Hee Yong Hwang, Sang-Won Yun, and Ik-Soo Chang. A design of planar elliptic bandpass filter using SMD type partially metallized rectangular dielectric resonators. In *Microwave Symposium Digest, 2001 IEEE MTT-S International*, volume 3, pages 1483 –1486 vol.3, 2001.

[83] Y.M.M. Antar and Z. Fan. Theoretical investigation of aperture-coupled rectangular dielectric resonator antenna. *Microwaves, Antennas and Propagation, IEE Proceedings*, 143(2):113 –118, apr 1996.

[84] Achraf Jaoujal, Noura Aknin, and Ahmed El Moussaoui. Wide-Band Rectangular Dielectric Resonator Antenna for Wireless Applications. In *PIERS Proceedings*, pages 20–23, 2011.

[85] Hee Yong Hwang and Sang-Won Yun. Novel $TE_{10\delta}$; rectangular-waveguide-type resonators and their bandpass filter applications. *Microwave Theory and Techniques, IEEE Transactions on*, 50(7):1821 – 1831, jul 2002.

[86] B.Yu. Kapilevich and Ye.R. Trubekhin. *Waveguide Dielectric Filtering Structures*. Radio and Svjaz, in Russian, 1990.

[87] A. Chandra Kundu and I. Awai. Resonant frequency and quality factors of a silver-coated $\lambda/4$ dielectric waveguide resonator. *Microwave Theory and Techniques, IEEE Transactions on*, 46(8):1124 –1131, aug 1998.

[88] J. Sheen. Losses of the parallel-plate dielectric resonator. *Microwaves, Antennas Propagation, IET*, 2(3):221 –228, april 2008.

[89] S.J. Penn, N.McN. Alford, and T.W. Button. High Q dielectric resonators using $YBa_2Cu_3O_7$ thick films and polycrystalline dielectrics. *Applied Superconductivity, IEEE Transactions on*, 7(2):3500 –3503, jun 1997.

[90] D.H.Staelin, A.W. Morgenthaler, and J.A.Kong. *Electromagnetic waves*. Prentice-Hall Int., 1994.

[91] A. Angrisani Armenio, C. Bell, J. Aarts, and C. Attanasio. High-velocity instabilities in the vortex lattice of Nb/permalloy bilayers. *Phys. Rev. B*, 76:054502, Aug 2007.

[92] A. I. Buzdin. Proximity effects in superconductor-ferromagnet heterostructures. *Rev. Mod. Phys.*, 77:935–976, Sep 2005.

[93] V. A. Oboznov, V. V. Bol'ginov, A. K. Feofanov, V. V. Ryazanov, and A. I. Buzdin. Thickness Dependence of the Josephson Ground States of Superconductor-Ferromagnet-Superconductor Junctions. *Phys. Rev. Lett.*, 96:197003, May 2006.

[94] Manlai Liang, Milind N. Kunchur, Jiong Hua, and Zhili Xiao. Evaluating free flux flow in low-pinning molybdenum-germanium superconducting films. *Phys. Rev. B*, 82:064502, Aug 2010.

[95] Pierre Gilles de Gennes. *Superconductivity of Metals and Alloys (Advanced book classics)*. Addison Wesley, 1989.

[96] B. Pannetier and H. Courtois. Andreev Reflection and Proximity effect. *Journal of Low Temperature Physics*, 118:599–615, 2000.

[97] A. I. Buzdin. The thermal conductivity of the intermediate state in superconductor. *Sov.Phys.-JETP*, 19:1228–1231, 1964.

[98] A. I. Buzdin. Proximity effects in superconductor-ferromagnet heterostructures. *Rev Mod Phys*, 77(3):935–942, jul 2005.

[99] N. Moussy, H. Courtois, and B. Pannetier. Local spectroscopy of a proximity superconductor at very low temperature. *EPL (Europhysics Letters)*, 55(6):861, 2001.

[100] T. Kontos, M. Aprili, J. Lesueur, and X. Grison. Inhomogeneous Superconductivity Induced in a Ferromagnet by Proximity Effect. *Phys. Rev. Lett.*, 86:304–307, Jan 2001.

[101] Guoya Sun, D. Y. Xing, Jinming Dong, and Mei Liu. Gapless superconductivity in ferromagnet/superconductor junctions. *Phys. Rev. B*, 65:174508, Apr 2002.

[102] Gert Eilenberger. Transformation of Gorkov's equation for type II superconductors into transport-like equations. *Zeitschrift far Physik*, 214:195–213, 1968.

[103] 1B.P. Vodopyanov and L.R. Tagirov. Andreev Conductance of a ferromagnet-superconductor point contact. *Journal of Experimental and Theoretical Physics Letters*, 77:126–131, 2003.

[104] Klaus D. Usadel. Generalized Diffusion Equation for Superconducting Alloys. *Phys. Rev. Lett.*, 25:507–509, Aug 1970.

[105] Yu. A. Izyumov, Yu. N. Proshin, and M. G. Khusainov. Competition between superconductivity and magnetism in ferromagnet/superconductor heterostructures. *Physics-Uspekhi*, 45(2):109–148, 2002.

[106] A. Buzdin. π-junction realization due to the tunneling through thin ferromagnetic layer. *EPL (Europhysics Letters)*, 78:1073, 2003.

[107] J. S. Jiang, D. Davidovié, Daniel H. Reich, and C. L. Chien. Oscillatory Superconducting Transition Temperature in Nb/Gd Multilayers. *Phys. Rev. Lett.*, 74:314–317, Jan 1995.

[108] A.S. Sidorenko, V.I. Zdravkov, A.A. Prepelitsa, C. Helbig, Y. Luo, S. Gsell, M. Schreck, S. Klimm, S. Horn, L.R. Tagirov, and R. Tidecks. Oscillations of the critical temperature in superconducting Nb/Ni bilayers. *Annalen der Physik*, 12(1-2):37–50, 2003.

[109] Ya. V. Fominov, N. M. Chtchelkatchev, and A. A. Golubov. Nonmonotonic critical temperature in superconductor/ferromagnet bilayers. *Phys. Rev. B*, 66:014507, Jun 2002.

[110] C Cirillo, E A Ilyina, and C Attanasio. Static and dynamic properties of the vortex lattice in superconductor/weak ferromagnet bilayers. *Superconductor Science and Technology*, 24(2):024017, 2011.

[111] C. Cirillo, C. Bell, G. Iannone, S. L. Prischepa, J. Aarts, and C. Attanasio. Nonmonotonic behavior of the anisotropy coefficient in superconductor-ferromagnet-superconductor trilayers. *Phys. Rev. B*, 80:094510, Sep 2009.

[112] Thomas R. Lemberger, Iulian Hetel, Adam J. Hauser, and F. Y. Yang. Superfluid density of superconductor-ferromagnet bilayers. *Journal of Applied Physics*, 103(7):07C701, 2008.

[113] C. Cirillo, S.L. Prischepa, A. Romano, M. Salvato, and C. Attanasio. Proximity effect in superconductor/highly paramagnetic Nb/Pd systems. *Physica C: Superconductivity*, 404:95 – 98, 2004. Proceedings of the Third European Conference on Vortex Matter in Superconductors at Extreme Scales and Conditions.

[114] C. Cirillo, A. Rusanov, C. Bell, and J. Aarts. Depairing current behavior in superconducting $Nb/Pd_{81}Ni_{19}$ bilayers. *Phys. Rev. B*, 75:174510, May 2007.

[115] C. Cirillo, S.L. Prischepa, M. Salvato, and C. Attanasio. Transport properties of Nb/PdNi bilayers. *Journal of Physics and Chemistry of Solids*, 67(1-3):412 – 415, 2006. Spectroscopies in Novel Superconductors 2004.

[116] C. Meneghini, F. Bardelli, and S. Mobilio. ESTRA-FitEXA: A software package for EXAFS data analysis. *Nuclear Instruments and Methods in Physics Research Section B: Beam Interactions with Materials and Atoms*, 285(0):153 – 157, 2012.

[117] Srimanta Middey, Sugata Ray, K. Mukherjee, P. L. Paulose, E. V. Sampathkumaran , C. Meneghini, S. D. Kaushik, V. Siruguri , Kirill Kovnir,

and D. D. Sarma. Glasslike ordering and spatial inhomogeneity of magnetic structure in $Ba_3FeRu_2O_9$: Role of Fe/Ru site disorder. *Phys. Rev. B*, 83:144419, Apr 2011.

[118] F. Liscio, M. Maret, C. Meneghini, S. Mobilio, O. Proux, D. Makarov, and M. Albrecht. Structural origin of perpendicular magnetic anisotropy in epitaxial $CoPt_3$ nanostructures grown on $WSe_2(0001)$. *Phys. Rev. B*, 81:125417, Mar 2010.

[119] A. I. Gubin, K. S. Il'in, S. A. Vitusevich, M. Siegel, and N. Klein. Dependence of magnetic penetration depth on the thickness of superconducting Nb thin films. *Phys. Rev. B*, 72:064503, Aug 2005.

[120] V. V. Ryazanov, V. A. Oboznov, A. Yu. Rusanov, A. V. Veretennikov, A. A. Golubov, and J. Aarts. Coupling of Two Superconductors through a Ferromagnet: Evidence for a π Junction. *Phys. Rev. Lett.*, 86:2427–2430, Mar 2001.

[121] C. Cirillo, S. L. Prischepa, M. Salvato, C. Attanasio, M. Hesselberth, and J. Aarts. Superconducting proximity effect and interface transparency in $Nb/PdNi$ bilayers. *Phys. Rev. B*, 72:144511, Oct 2005.

[122] A. I. Buzdin. private communication, 2012.

[123] N. Pompeo, E. Silva, S. Sarti, C. Attanasio, and C. Cirillo. New aspects of microwave properties of Nb in the mixed state. *Physica C: Superconductivity*, 470(19):901 – 903, 2010.

[124] E Silva, N Pompeo, and S Sarti. Wideband microwave measurements in $Nb/Pd_{84}Ni_{16}/Nb$ structures and comparison with thin Nb films. *Superconductor Science and Technology*, 24(2):024018, 2011.

[125] Y. B. Kim, C. F. Hempstead, and A. R. Strnad. Flux-Flow Resistance in Type-II Superconductors. *Phys. Rev.*, 139:A1163–A1172, Aug 1965.

[126] A. L. Larkin D. N. Langenberg. Nonequilibrium superconductivity. *Crystal Research and Technology*, 21(12):1540–1540, 1986.

[127] P. Berghuis, A. L. F. van der Slot, and P. H. Kes. Dislocation-mediated vortex-lattice melting in thin films of Nb_3Ge. *Phys. Rev. Lett.*, 65:2583–2586, Nov 1990.

[128] Robert J. Troy and Alan T. Dorsey. Transport properties and fluctuations in type-II superconductors near H_{c2}. *Phys. Rev. B*, 47:2715–2724, Feb 1993.

[129] Nikolai B. Kopnin. *Theory of Nonequilibrium Superconductivity (International Series of Monographs on Physics)*. Oxford University Press, USA, 2001.

[130] A. Angrisani Armenio, C. Cirillo, G. Iannone, S. L. Prischepa, and C. Attanasio. Upper critical fields and interface transparency in superconductor/ferromagnet bilayers. *Phys. Rev. B*, 76:024515, Jul 2007.

[131] D. Janjušević, M. S. Grbić, M. Požek, A. Dulčić, D. Paar, B. Nebendahl, and T. Wagner. Microwave response of thin niobium films under perpendicular static magnetic fields. *Phys. Rev. B*, 74:104501, Sep 2006.

[132] J. A. Fendrich, W. K. Kwok, J. Giapintzakis, C. J. van der Beek, V. M. Vinokur, S. Fleshler, U. Welp, H. K. Viswanathan, and G. W. Crabtree. Vortex Liquid State in an Electron Irradiated Untwinned $YBa_2Cu_3O_{7-\delta}$ Crystal. *Phys. Rev. Lett.*, 74:1210–1213, Feb 1995.

[133] L. Civale, A. D. Marwick, T. K. Worthington, M. A. Kirk, J. R. Thompson, L. Krusin-Elbaum, Y. Sun, J. R. Clem, and F. Holtzberg. Vortex confinement by columnar defects in $YBa_2Cu_3O_{7-\delta}$ crystals: Enhanced pinning at high fields and temperatures. *Phys. Rev. Lett.*, 67:648–651, Jul 1991.

[134] J. L. MacManus-Driscoll, S. R. Foltyn, Q. X. Jia, H. Wang, A. Serquis, L. Civale, B. Maiorov, M. E. Hawley, M. P. Maley, and D. E. Peterson. Strongly enhanced current densities in superconducting coated conductors of $YBa_2Cu_3O_{7-\delta} + BaZrO_3$. *Nature Materials*, 3(7):439–443, 2004.

[135] Zhidong Hao and John R. Clem. Angular dependences of the thermodynamic and electromagnetic properties of the high-T_c superconductors in the mixed state. *Phys. Rev. B*, 46:5853–5856, Sep 1992.

[136] Zhidong Hao, Chia-Ren Hu, and C. S. Ting. Out-of-plane transverse resistivity in high-T_c superconductors as a signature of flow of rigid vortex lines. *Phys. Rev. B*, 52:R13138–R13140, Nov 1995.

[137] Zhidong Hao, Chia-Ren Hu, and C. S. Ting. Consistency between the Lorentz-force independence of the resistive transition in the high-T_c superconductors and the standard theory of flux flow. *Phys. Rev. B*, 51:9387–9390, Apr 1995.

[138] N. Pompeo. Theory of measurements of electrodynamic properties in anisotropic superconductors in tilted magnetic fields. Part I: flux flow and Campbell regimes. *arXiv:1211.3355 [cond-mat.supr-con]*, 2012.

[139] N. Pompeo. Theory of measurements of electrodynamic properties in anisotropic superconductors in tilted magnetic fields. Part II: high frequency regimes. *arXiv:1211.3731 [cond-mat.supr-con]*, 2012.

[140] A. Augieri, V. Galluzzi, G. Celentano, A.A. Angrisani, A. Mancini, A. Rufoloni, A. Vannozzi, E. Silva, N. Pompeo, T. Petrisor, L. Ciontea, U. Gambardella, and S. Rubanov. Transport Property Improvement by Means of BZO Inclusions in PLD Grown YBCO Thin Films. *Applied Superconductivity, IEEE Transactions on*, 19(3):3399 –3402, june 2009.

[141] A. Augieri, G. Celentano, V. Galluzzi, A. Mancini, A. Rufoloni, A. Vannozzi, A. Angrisani Armenio, T. Petrisor, L. Ciontea, S. Rubanov, E. Silva, and N. Pompeo. Pinning analyses on epitaxial $YBa_2Cu_3O_{7-\delta}$ films with $BaZrO_3$ inclusions. *Journal of Applied Physics*, 108(6):063906, 2010.

[142] N. Pompeo, R. Rogai, A. Augieri, V. Galluzzi, G. Celentano, and E. Silva. Reduction in the field-dependent microwave surface resistance in $YBa_2Cu_3O_{7-\delta}$ with submicrometric $BaZrO_3$ inclusions as a function of $BaZrO_3$ concentration. *Journal of Applied Physics*, 105(1):013927, 2009.

[143] David R. Nelson and V. M. Vinokur. Boson localization and correlated pinning of superconducting vortex arrays. *Phys. Rev. B*, 48:13060–13097, Nov 1993.

[144] A Rufoloni, A Augieri, G Celentano, V Galluzzi, A Mancini, A Vannozzi, T Petrisor, L Ciontea, V Boffa, and U Gambardella. $YBa_2Cu_3O_{7-\delta}$ films prepared by TFA-MOD method for coated conductor application. *Journal of Physics: Conference Series*, 43(1):199, 2006.

[145] A.A. Armenio, G. Celentano, A. Rufoloni, A. Vannozzi, A. Augieri, V. Galluzzi, A. Mancini, L. Ciontea, T. Petrisor, G. Contini, and I. Davoli. Deposition and Characterization of Metal Propionate Derived Epitaxial Films for Coated Conductor Fabrication. *Applied Superconductivity, IEEE Transactions on*, 19(3):3204 –3207, june 2009.

[146] A Maeda, Y Tsuchiya, K Iwaya, K Kinoshita, H Kitano, T Hanaguri, T Nishizaki, K Shibata, N Kobayashi, J Takeya, K Nakamura, and Y Ando. Dynamics vs electronic states of vortex core of high-Tc superconductors investigated by high-frequency impedance measurement. *Physica C: Superconductivity*, 362(1-4):127 – 133, 2001.

[147] Jonathan I. Gittleman and Bruce Rosenblum. Radio-Frequency Resistance in the Mixed State for Subcritical Currents. *Phys. Rev. Lett.*, 16:734–736, Apr 1966.

[148] A.E. Koshelev and V.M. Vinokur. Frequency response of pinned vortex lattice. *Physica C: Superconductivity*, 173(5-6):465 – 475, 1991.

[149] L. Miu. Vortex depinning temperature in $YBa_2Cu_3O_{7-\delta}$ films with $BaZrO_3$ nanorods. *Phys. Rev. B*, 85:104519, Mar 2012.

[150] A Rufoloni, A Augieri, G Celentano, V Galluzzi, A Mancini, A Vannozzi, T Petrisor, L Ciontea, V Boffa, and U Gambardella. $YBa_2Cu_3O_{7-\delta}$ films prepared by TFA-MOD method for coated conductor application. *Journal of Physics: Conference Series*, 43(1):199, 2006.

[151] Y. Kobayashi and S. Tanaka. Resonant Modes of a Dielectric Rod Resonator Short-Circuited at Both Ends by Parallel Conducting Plates. *Microwave Theory and Techniques, IEEE Transactions on*, 28(10):1077 – 1085, oct 1980.

List of Publications

1. A. Angrisani Armenio, A. Augieri, F. Fabbri, R. Freda, V. Galluzzi, A. Mancini, F. Rizzo, A. Rufoloni, A. Vannozzi, G. Sotgiu, N. Pompeo, K. Torokhtii, E. Silva, E. Bemporad, G. Contini, and G. Celentano. Growth and Characterization of $La_2Zr_2O_7$ Buffer Layers Deposited by Chemical Solution Deposition. Physics Procedia, 36(0):1552 1557, 2012.
   doi: 10.1016/j.phpro.2012.06.209. Superconductivity Centennial Conference 2011.

2. K. Torokhtii, C. Attanasio, C. Cirillo, E.A. Ilyina, N. Pompeo, S. Sarti, and E. Silva. Vortex motion in Nb/PdNi/Nb trilayers: New aspects in the flux flow state. Physica C: Superconductivity, 479(0):140 142, 2012. doi:10.1016/j.physc.2011.12.011. Proceedings of VORTEX VII Conference.

3. N. Pompeo, R. Rogai, K. Torokhtii, A. Augieri, G. Celentano, V. Galluzzi, and E. Silva. Angular dependence of the high-frequency vortex response in $YBa_2Cu_3O_{7-x}$ thin film with self-assembled $BaZrO_3$ nanorods. Physica C:Superconductivity, 479(0):160 163, 2012.
   doi: 10.1016/j.physc.2011.12.008. Proceedings of VORTEX VII Conference.

4. N. Pompeo, K. Torokhtii, A. Augieri, G. Celentano, V. Galluzzi, and E. Silva. Directional Vortex Pinning at Microwave Frequency in $YBa_2Cu_3O_{7-x}$. Journal of Superconductivity and Novel Magnetism, pages 15, 2012. doi: 10.1007/s10948-012-2060-9.

5. N. Pompeo, K. Torokhtii, C. Meneghini, S. Mobilio, R. Loria, C. Cirillo, E.A. Ilyina, C. Attanasio, S. Sarti, and E. Silva. Superconducting and Structural Properties of Nb/PdNi/Nb Trilayers. Journal of Superconductivity and Novel Magnetism, pages 15, 2012. doi: 10.1007/s10948-012-2057-4.

6. K. Torokhtii, N. Pompeo, C. Meneghini, C. Attanasio, C. Cirillo, E.A.

Ilyina, S. Sarti, and E. Silva. Microwave Properties of Nb/PdNi/Nb Tri-layers. Journal of Superconductivity and Novel Magnetism, 26:571574, 2013. doi:10.1007/s10948-012-1795-7.

7. N. Pompeo, A. Augieri, K. Torokhtii, V. Galluzzi, G. Celentano, E. Silva. Vortex matter dynamics in YBaCuO with $BaZrO_3$ nanocolumns as revealed by dc and high-frequency experiments: role of anisotropy and directional pinning. arXiv:1211.3311 [cond-mat.supr-con] (submitted to Applied Physics Letters).

Acknowledgements